INVESTIGATION OF HOMOGENEOUS-HETEROGENEOUS COUPLING EFFECTS IN THE HIGH TEMPERATURE CATALYTIC OXIDATION REACTIONS OF LIGHT ALKANES IN A NOVEL MICROCHEMICAL REACTOR SYSTEM

by

Sen Liu

Bachelor in Chemical Engineering, Tsinghua University, 2007

Submitted to the Graduate Faculty of

Swanson School of Engineering in partial fulfillment

of the requirements for the degree of

Doctor of Philosophy

University of Pittsburgh

2011

UNIVERSITY OF PITTSBURGH

SWANSON SCHOOL OF ENGINEERING

This dissertation was presented

by

Sen Liu

It was defended on

November 15, 2011

and approved by

Joseph J. McCarthy, Ph.D., Professor, Chemical and Petroleum Engineering Department

Sachin S. Velankar, Ph.D., Professor, Chemical and Petroleum Engineering Department

Peyman Givi, Ph.D., Professor, Mechanical Engineering and Materials Science Department

Dissertation Director: Götz Veser, Ph.D., Professor, Chemical and Petroleum Engineering Department

INVESTIGATION OF HOMOGENEOUS-HETEROGENEOUS COUPLING EFFECTS IN THE HIGH TEMPERATURE CATALYTIC OXIDATION REACTIONS OF LIGHT ALKANES IN A NOVEL MICROCHEMICAL REACTOR SYSTEM

Sen Liu, PhD

University of Pittsburgh, 2011

Understanding the coupling effects between homogeneous and heterogeneous (HH) chemistry is crucial in the field of high-temperature catalysis. An important example in this area is the catalytic oxidation of light hydrocarbons. Microreactor technology, with its precise control of fluid and temperature fields, improved reactant mixing, and large surface-to-volume ratio, is ideally suited for the study of such reaction systems. Most significantly, the pathways of homogeneous-heterogeneous coupling can be better understood as critical reactor dimensions are reduced into micrometer range, where diffusive flux starts to play an equally important role as convective transport.

Here, we are reporting a novel modular microreactor system based on the use of silicon-based thin-film catalysts, which allows stable operation during thermal cycling up to 800 ^{o}C. Precise control and adjustment of the critical dimension, i.e. the height of reaction chamber, offers the ability to steer the relative importance of gas- and catalytic-phase chemistries due to transport of reactants between the gas phase and the catalytic walls. Additionally, a moveable thermocouple and quartz-glass capillary (connected to a mass spectrometer) allow the in-situ measurement of temperature and composition profiles in the reaction chamber. By combining these two capabilities, the system thus provides an efficient and sensitive way to investigate the

interplay between gas phase and catalytic chemistries, and to evaluate the catalytic performance of thin-film catalysts. The reactor system was tested using oxidative coupling of methane (OCM) as model reaction. OCM has been studied intensively for many decades and offers a potentially highly efficient path for direct upgrading of methane to higher-value C_2 products. The reaction is also well known to include catalytic steps in the generation of methyl radicals (as well as in undesired methane combustion) and homogeneous reaction steps in which methyl radicals are coupled to form the desired C_2 products (C_2H_6 and C_2H_4). It thus forms an ideal test system for the above described microreactor system.

A La-based thin-film catalyst was deposited onto a silicon chip via dip-coating, characterized, and inserted into the microreactor. The effect of major reactor operating parameters, such as temperature, flow rate, C:O feed ratio, and, most importantly, the surface-to-volume ratio were tested in detailed experimental studies using both reactor outlet and spatially-resolved concentration profiles. The results show a strong decrease of C_2 production rates with decreasing microreactor channel height (680 µm to 460 and 330 µm), in agreement with the established OCM reaction mechanism. A 2D FEM-based numeric model was also carried out to provide supports and further insights into OCM system. While the Pt- and Rh-catalyzed oxidative dehydrogenation of ethane (ODH) is currently under investigation as the second model reaction, it is promising that this methodology can be transferred to study several other systems, e.g. hydrogen oxidation and catalytic partial oxidation of methane (CPOM) and propane (CPOP).

TABLE OF CONTENTS

LIST OF TABLES

LIST OF FIGURES

PREFACE

I would like to sincerely thank Professor Götz Veser for providing me the chance to work on this changeling yet very interesting research project. His knowledge and guidance during the past several years benefit me greatly, not only letting me realize my passion for chemical reaction engineering and the petrochemical industry, but also gradually nurturing my habit and ability to think and research independently.

I would also like to acknowledge Tom Gasmire from the machine shop in the department of chemistry. Tom provided a long-time support to help me design and build the microchemical reactor system, and for many times repaired the broken ones with suggestions for further improvement. Additionally, I would like to give credit to my lab mate Shuang Liang, who helped me synthesize and characterize the relevant thin-film catalysts for different reaction systems. It was with his help that I could build a bridge between reaction engineering and material science, and gained more knowledge from the material aspect.

Lastly, I would like to thank for my family for their continuous moral support. Thanks for my brother to advise and help me on the numerical simulation by providing me with deeper knowledge in the field of computer science.

1.0 INTRODUCTION

1.1 HIGH TEMPERATURE CATALYSIS AND CATALYTIC MICROREACTOR

Catalysts are generally applied to lower the activation barriers for specific reaction pathways, such that reactions can progress much faster than those that are not catalyzed. Conventional studies in the field of heterogeneous catalysis are focused on low temperature conditions, where homogeneous reaction pathways cannot be triggered and become trivial. However, under high-temperature conditions, the contribution of homogeneous chemistry becomes larger and is sometimes comparable to its heterogeneous counterpart [1]. Thus, in order to investigate the general behavior of the reactive flow, reliable mechanisms for both reaction pathways need to be developed. Moreover, the catalytic reaction system is always characterized by a complex interplay between transport processes for mass, energy and momentum and detailed gas-phase as well as catalytic chemistries [2].

A particularly important reaction system belongs to this kind is the high-temperature catalytic oxidation of hydrocarbons, which is of highly relevance to the combustion of fossil fuels and thus energy industry [3-5]. It has been studied intensively during past several decades because of their great industrial potential. In these systems, homogeneous reactions can occur in parallel to catalytic reactions, as long as the temperature is sufficiently high to overcome the activation barriers of homogeneous reaction pathways. Usually, the appearance of homogeneous reactions is an undesired feature, since it introduces extra complexity to the reaction system,

leads to selectivity losses to the desired products, and poses a safety hazard resulting from uncontrolled process temperatures, reactor runaway and even explosion behavior [2, 6, 7]. To guarantee the reaction is proceeding in a safe manner, the underlying reaction mechanism should be thoroughly understood. Also, main parameters which will have significant impact on the ignition behavior need to be identified and analyzed carefully. Tremendous effects have been devoted to the investigation in this field for both homogeneous and catalytic processes, which is far from trivial. As shown in Figure 1 [8], the complexity of chemistry and reactor system increases dramatically from hydrogen to methane and to even higher hydrocarbons.

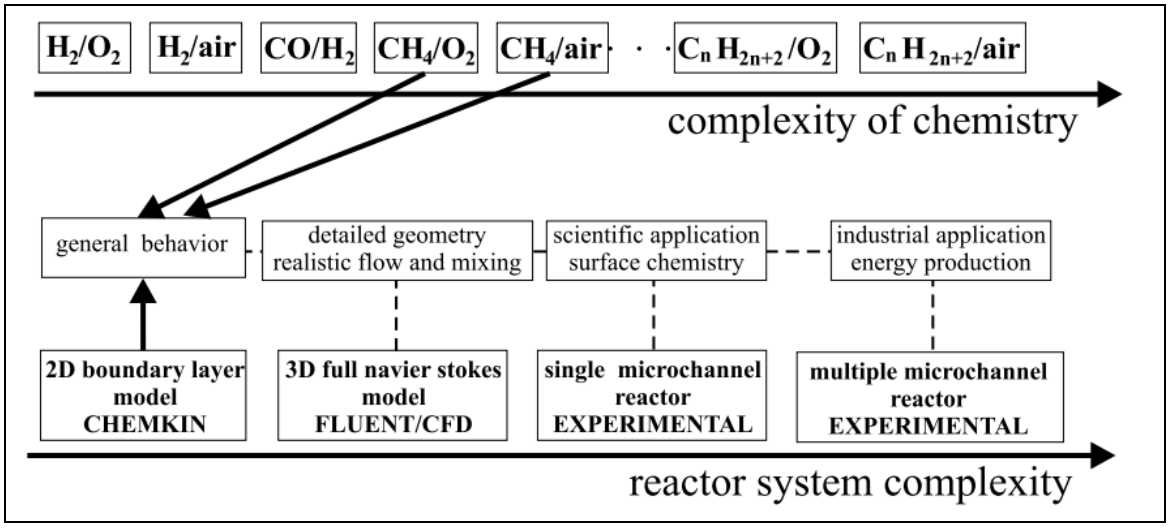

Figure 1. Schematic of research approach for investigating and analyzing high-temperature homogeneous and heterogeneous oxidation reactions for hydrocarbon fuels.

Microreactor is usually defined as a miniature reactor system that, to some extent, utilizing microtechnology and precision engineering. The characteristic dimension of the internal structure of a microreactor is typically within the range from submicrometer to submillimeter. Lots of efforts have been put into the investigation and development of microsystems during the past decade. Different type of reactors (gas and liquid phase [9, 10]) as well as unit operations

such as micromixer [11, 12] and microseparator [13, 14], have been brought forward. All these efforts have resulted in the success implementation of an integrated multistep synthesis system that directly leads to the desired product [15]. Small-length scale microsystems offer potential advantages such as reduced reaction volumes, enhanced heat and mass transfer, and precise control of temperature and flow pattern.

Interestingly, microreactor technology shows great potential in the field of high temperature catalysis. The application of microreactor can effectively solve the issue of mass transfer limitation for gas-phase processes which are kinetically fast at high temperature. Moreover, heterogeneously catalyzed gas-phase reactions will gain benefit from an increase of surface-to-volume ratio in a microreactor, where reactions usually occur at the gas-to-solid interfaces. Another important aspect is regarding to the safety issues for the catalytic burning and selective oxidation of hydrocarbons. The use of microreactor system is essential to control the inherent danger of explosion and flames, which is generally not possible by using conventional reactor equipment. The very first remarkable experiment was done by Veser et al. [16] to investigate the catalytic combustion of hydrogen in a silicon-based microreactor, with an embedded commercial platinum wire as the catalyst. Safe operation was demonstrated as no open flames and explosion were observed during the experiment. The effective suppression of gas-phase reactions was not only caused by enhanced thermal quenching, but rather by a distinct “radial quenching” mechanism. The finding shows great potential to investigate high temperature catalysis by using microreactor systems. More importantly, it paves the way for the further study into the homogeneous-heterogeneous coupling reaction systems.

1.2 HOMOGENEOUS-HETEROGENEOUS REACTION AND THE COUPLING BEHAVIOR

There are many important chemical processes belonging to the homogeneous-heterogeneous (HH) reaction mechanisms, such as combustion [17, 18], catalytic partial oxidation (CPO) (e.g. methane, propane to syngas) [19-21], oxidative dehydrogenation (e.g. ethane to ethylene) [22-24], oxidative coupling of methane (OCM) [25-27], and the catalytic fast pyrolysis of biomass which has been introduced recently [28, 29].

These reaction systems are of crucial importance because they are closely related to the energy industry. The proportion of homogeneous chemistry in these chemical systems varies with different applications and operating conditions. For instance, by modeling the high-temperature catalytic partial oxidation of methane over platinum gauze [30], Raul et al. have demonstrated that although some gas-phase reactions are predicted to be significant at elevated pressure and residence time, heterogeneous reaction kinetics is predominant for the overall process. On the contrary, oxidative dehydrogenation of ethane to ethylene (ODH) can be viewed as a sequential one, in which ethane is first oxidized to CO, CO_2 and water close to reactor inlet. The heat released due to surface reaction causes a substantial temperature rise that drives the dehydrogenation of ethane to ethylene in the gas phase [23, 31]. In other words, in ODH reaction, gas-phase kinetics dominates the process behavior.

More interestingly, recent work by Beretta et al. that investigated HH interaction in propane CPO [21] suggests a “synergy” effect, where gas-phase chemistry enriches the fuel by smaller hydrocarbon species, making catalytic reactions faster and more efficient. The author further generalized that the relative importance of gas-phase versus catalytic reactions in high-temperature CPO originated from the relative difficulty of gas-phase C-H bond activation and catalytic steam reforming (SR). So far, research efforts in this area are still intensive, aiming to

provide more insights into these unusual reaction systems, so that these chemical processes can be harnessed more efficiently.

In terms of methodology, all these previous works for HH coupling study are mainly focused on several aspects: 1) finding evidence for the participation of gas-phase or catalytic reaction pathways; 2) quantifying the relative contributions for gas-phase and catalytic chemistries; 3) verifying the proposed numerical modeling based on elementary reaction mechanism, by comparing with experiment results (spatially resolved profiles as well as reactor exit data). However, none of these suggest a feasible way to adjust and steer the relative contributions between gas-phase and catalytic chemistries. As mentioned in Chapter 1.1, in studying the Pt-catalyzed hydrogen oxidation reaction [16], it has been demonstrated for the first time in our group, that it is possible to influence the HH interplay in a micro-scaled reactor by radical quenching. Further simulation tests performed in our group confirmed the quenching effect. Chattopadhyay et al. [1] applied a 2D boundary layer model in CHEMIKIN with isothermal consumption to study the hydrogen oxidation reaction. The key results can be explained by reproducing two figures (Figure 2 and 3) from the paper.

It can be clearly seen in Figure 2 that concentration of H radical (indicator for gas-phase kinetics) decreases dramatically as the diameter of the microchannel decreases, with the smallest channel resulting in a trivial amount of H radicals (2×10^{-10} mol/m^3). This means that gas-phase chain propagation reaction pathways have been suppressed almost completely, due to radical quenching effect as the surface-to-volume ratio of the reaction chamber increased to a sufficient level.

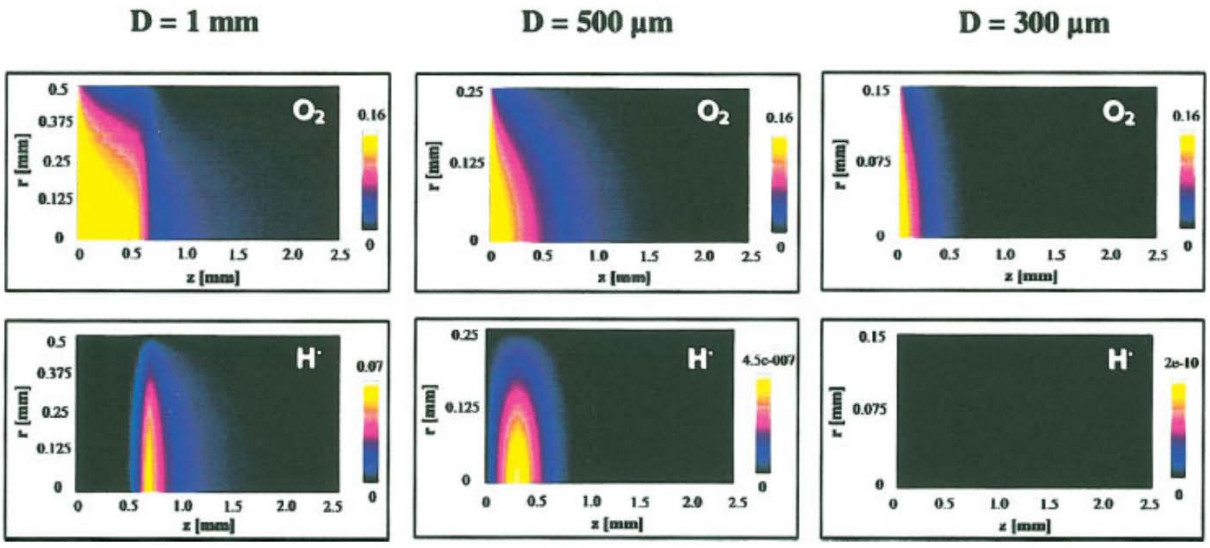

Figure 2. Contour plot of O_2 concentration (top row) and H radical concentration (bottom row) as a function of axial (z) and radial (r) direction for a Pt-coated microchannel with diameters of 1 mm (left), 500 µm (middle), and 300 µm (right) at T = 1113 K.

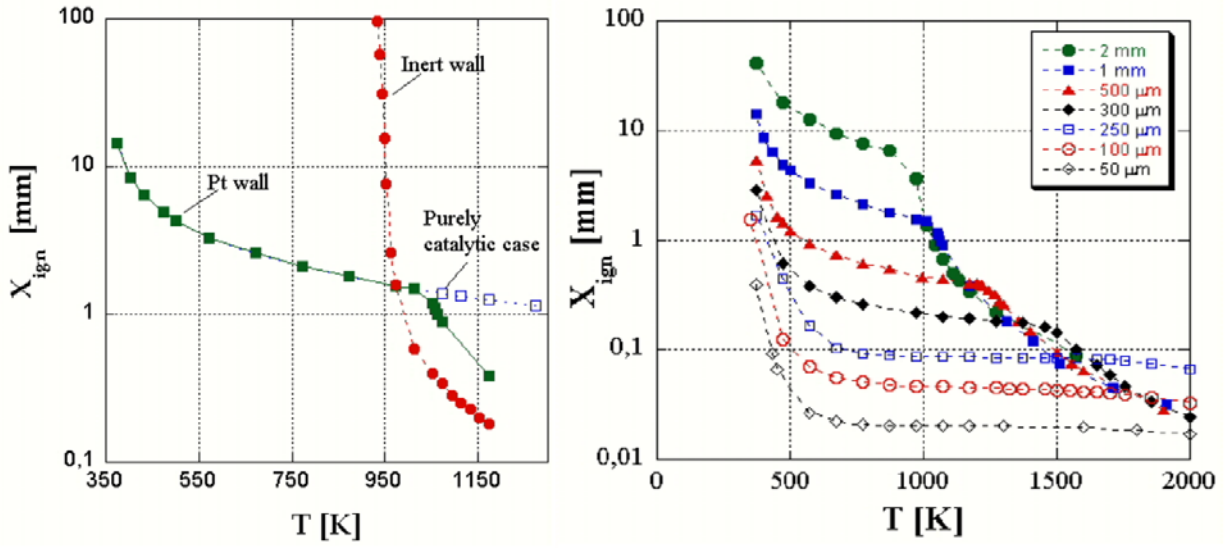

Figure 3. Ignition distance vs. reaction temperature for a reactor with 1mm diameter (left) for pure homogeneous, heterogeneous and HH coupled chemistry; Ignition distance versus reaction temperature for a reactor with catalytic Pt-wall varying channel diameters (right).

This trend can also be confirmed by looking at ignition curves at elevated temperature as presented in Figure 3. The left figure shows the presence of catalytic chemistry can retard gas-phase kinetics characterized by an increase of ignition distance, which is defined as the distance from reactor inlet to a point where 50% hydrogen is converted at reactor centerline. As the diameter of reactor decreases, the retard effect becomes less pronounced which indicates a shift from homogeneously dominated ignition to a heterogeneously dominated one. When the diameter of the reactor decreases to around 250 μm, homogenous reaction pathways have been completely suppressed and no "turning point" can be seen on the curves.

The successful simulation of hydrogen oxidation reaction demonstrates the possibility to alter HH coupling behavior by changing the critical dimension of reaction chamber. It forms the theoretical foundation for both experimental and numerical studies that will be described in later chapters.

1.3 NUMTERICAL MODELING FOR REACTIVE FLOW BEHAVIOR

The behavior of the reactive flow at high temperature is very complex, which is characterized by intricate interactions between gas-phase and catalytic chemistries, as well as molecular transport and heat transfer. By building appropriate numerical models, people can better understand the underlying physics of these complex systems.

From the methodology point of view, the most complex model should solve the full Navier-Stokes equation, with both axial and radial mass transport considered (both gas-phase and catalytic elementary steps included), as well as energy balance equation. Generally, solving the complete Navier-Stokes is computationally expensive and sometime may not be necessary.

Certain simplifications can be made to reduce the computation efforts. For example, the full Navier-Stokes model can turn into a simple plug flow model if diffusive terms are totally omitted. An alternative is the model based on boundary layer approximation, in which the axial diffusive terms are neglected but diffusion in radical direction is retained. The model provides accurate solutions when the mass transport is dominated by convection, i.e. at high Peclet number conditions. The computation efforts, for both plug-flow and boundary layer model, are expected to be dramatically reduced.

Additionally, the simplest way to calculate the diffusion term in mass transport is to directly apply the Fickian diffusion model, in which binary diffusion coefficients for species in gaseous phase can be calculated by setting one species as the reference. However, when the diluted condition does not hold, the multicomponent transport model may be required in order to accurately capture the system behavior, such as mixture-averaged diffusion model or Maxwell-Stefan diffusion model. These extra complexities can lead to a dramatic increase of computation demands.

Also, in studying the high-temperature chemical processes, the complexity of the reaction kinetics also matters. While the most complex mechanism needs to consider all important elementary reaction steps in both gas phase and on catalytic surface, simplifications can be made by constructing a global reaction network with major reactants, products and intermediates involved. The correctness of the proposed reaction kinetics was initially tested by reactor exit data acquired in experiments [32], and more recently can be verified by spatially resolved temperature and species compositional profiles [5].

Due to the fast advancement of computation capabilities, as well as the increasing demands for numerical models with better accuracy, models with all complexities described

previously can be developed, especially for some industrially important chemical processes, i.e. automotive exhaust gas after-treatment [33-35], catalytic combustion [36], solid-oxide fuel cells [37], and hydrogen production from reforming of diesel and gasoline [38, 39]. Computation geometries applied in model is developed from original 1D to 2D and even 3D [30]. More interestingly, the aim for numerical simulation is not just for understanding the reactive flow behavior, but more progressively, towards the optimization of the targeted parameters, e.g. the yield of the desired product [40].

One remarkable feature to study high temperature processes numerically is the possibility to open and shut down specific reaction pathways and look into the influence on the overall system behavior, which is usually unfeasible in experimental study. A remarkable example is the study of catalytic partial oxidation of propane (CPOP) to produce syngas, in which Beretta et al. [21] identified numerically that the steam reforming (SR) of C_2 and C_3 intermediate species has played an important role to the overall system behavior. The exclusion of corresponding SR reaction steps could lead to a severe underestimation of syngas production, accompanied by an unreasonable temperature rise. Another interesting example is the Pt-catalyzed hydrogen oxidation studied in our group. As can be seen in Figure 3, numerical simulation allows the study of pure homogeneous and heterogeneous chemistry separately, as well as the coupling between the two. However, in actual experiments, homogeneous kinetics cannot be avoided, as long as the system temperature is sufficiently high to trigger the gas-phase reaction pathways.

In this thesis, we move further to extend the numerical simulation to the oxidative coupling of methane (OCM), which belongs to the HH coupling reaction systems. The modeling was implemented by using commercially available software COMSOL Multiphysics, a powerful interactive environment for modeling scientific and engineering problems based on partial

differential equations (PDEs) [41, 42]. The COMSOL program is based on finite element method (FEM) which aims at solving coupled physics phenomena within complex geometries. Detailed modeling procedures, as well as result discussion for OCM are presented in Chapter 5.0. Also, governing equations, relevant OCM mechanisms and all mathematical equations are available in appendix.

2.0 RESEARCH OBJECTIVES

This project is targeting at understanding the complex interaction behavior in HH reaction systems, especially, the high-temperature catalytic oxidation of hydrocarbons. Previous works published in literature usually focus on identifying the relative importance of gas-phase chemistry versus its heterogeneous counterpart. By combining experiment and numerical modeling, the contribution of each part to the overall chemical process can be quantified. However, all these works do not indicate a possible way to alter the relative magnitude between two chemistries. This may be due to the fact that a major proportion of these works use a reactor setup applying ceramic monolith with catalyst washcoat, which lacks such ability for the systematical adjustment of the geometrical structure of the reaction chamber.

Here, the work in this thesis aims to move a step further to demonstrate the ability to control and steer the relative importance of gas-phase versus catalytic chemistry, by changing the critical dimension of the microchemical reactor system, i.e. the height of reaction chamber. We want to show that, such a change is resulted, not only from the relative change of gas-phase versus catalytic reactions, also due to the interaction between the two chemistries. More importantly, we hope to provide a novel and complete methodology based on which HH reaction systems can be systematically and accurately studied.

The key point behind this idea can be shown by the following equation

$$\frac{dN_i}{dt} = r_g V + r_s A = (r_g d + r_s) A \qquad \text{(Eqn. 2.1)}$$

where N_i (mol) represents the total amount of a certain species; r_g (mol/(m^3·s)) denotes the net formation rate of species i due to gas-phase reactions; r_s (mol/(m^2·s)) represents the net formation rate of species i due to catalytic reactions; V and A denotes the volume of the reaction chamber and the area of catalytic surface, respectively; d is the height of a rectangular-shaped reaction chamber. Basically, this equation states that the formation rate of a gas-phase species is resulted from both gas-phase and catalytic reactions. By changing the height of reaction chamber, we will be able to control the relative contributions from both chemistries. For example, if gas-phase chemistry favors the formation of a certain species, thus we know from Eqn. 1 that the selectivity to this species can be enhanced if d is increased.

Importantly, the precondition for this argument is that, formation rates for both chemistries should be comparable in order of magnitude. One possible way to achieve this is to apply a microreactor device, in which contribution from catalytic chemistry may be enhanced due to its large surface-to-volume ratio. In other words, HH coupling mechanism may be better studied and understood in a microchemical reactor system.

Specifically, to study the HH reaction, a novel microchemical reactor system needs to be designed and manufactured with the following characteristics: 1) able to adjust the critical dimension of the reaction chamber in a convenient manner; 2) allow stable and safe operation under high-temperature conditions; 3) chemically inert for the building materials; 4) able to load thin-film catalyst. As will be introduced in Chapter 3.0, a microchemical reactor system with all these capabilities was successfully developed.

Furthermore, another equally important question is how to select the model reaction for investigation. Such reaction system should involve gas-phase and catalytic chemistries, and both should have a nontrivial influence on the system behavior. As one can see in Chapter 4.0, OCM

was selected as the model reaction, which has been thoroughly investigated both by experiment and simulation. Several aspects contributes to this decision: 1) decent understanding has already been achieved in understanding this unusual HH system; 2) gas-phase and catalytic chemistries in OCM behave drastically different, the former of which favors C_2 formation by radical coupling, while the latter favors C_1 formation via catalytic deep oxidation; 3) gas-phase and catalytic chemistries in OCM are tightly coupled with each other: gas-phase needs radicals generated from the catalytic surface, and catalytic surface has various reaction channels to oxidize gas-phase molecules. Moreover, ODH was chosen as the second system for study for similarly reasons (see Chapter 6.0). A major difference for ODH lies in that, C_2H_6 is the reactant and mainly consumed by dehydrogenation reaction in the gaseous phase.

In summary, the work presents in this thesis aims to develop a detailed methodology to study HH reaction systems. In order to achieve this goal, a novel microchemical rector system is designed which allows the fitting of thin-film catalyst. In this system, the relative amount of gas-phase and catalytic chemistry can be varied by adjusting the surface-to-volume ratio via changing the gap height of reaction chamber. OCM and ODH have been selected as the model reactions for study, due to their unusual HH coupling characteristics. It is hoped that, extension to study other important chemical processes becomes possible after these two systems have been demonstrated.

3.0 THE DESIGN OF THE MICROCHEMICAL REACTOR SYSTEM

3.1 OVERVIEW OF THE MICROCHEMICAL REACTOR SYSTEM

A microchemical reactor system was designed for the purpose of investigating homogeneous-heterogeneous coupling behavior for high-temperature catalysis. As shown in Figure 4 (design) and 5 (actual), the left-side channels allow the feeding of fuel and oxidant separately. After passing through the reaction chamber, gas stream is guided out from the right-side channel. During the design process, important issues were considered carefully, such as thermal compatibility and durability, machining accuracy, gas-tight sealing at interfaces, fuel-oxidant mixing and thin-film catalyst incorporation.

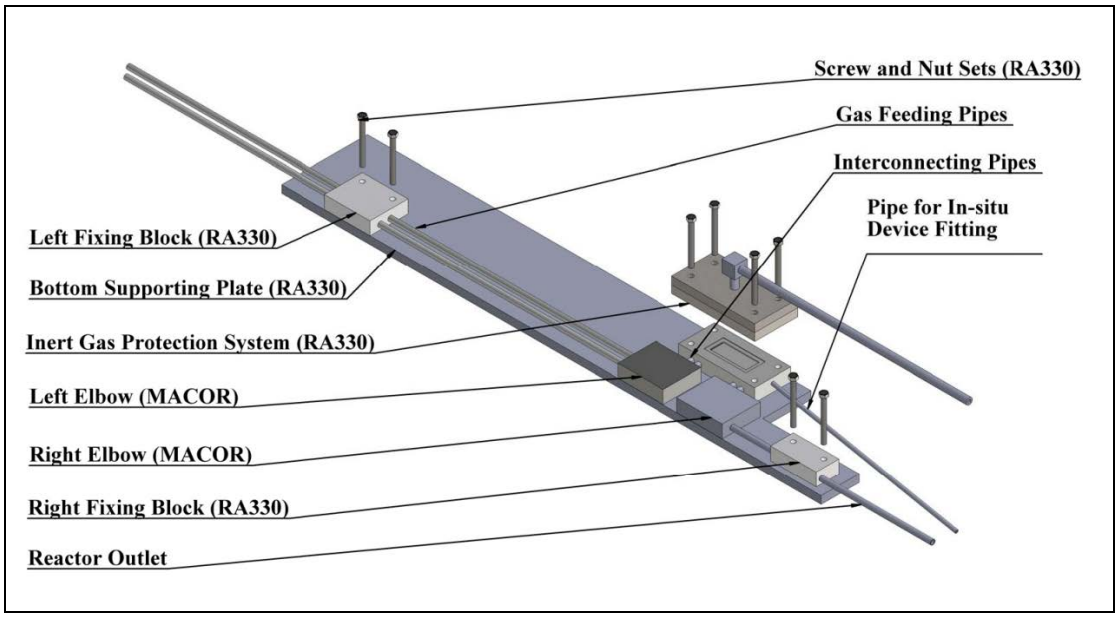

Figure 4. Three-dimensional view of the complete microchemical reactor system (drawn in AutoCAD 2009).

Figure 4 shows three dimensional view of the complete reactor system, which consists of several parts: 1) the main microreactor; 2) left and right ceramic elbows; 3) alumina pipes for gas transport; 4) inert gas protection system; 5) left and right fixing blocks; 6) the bottom supporting plate.

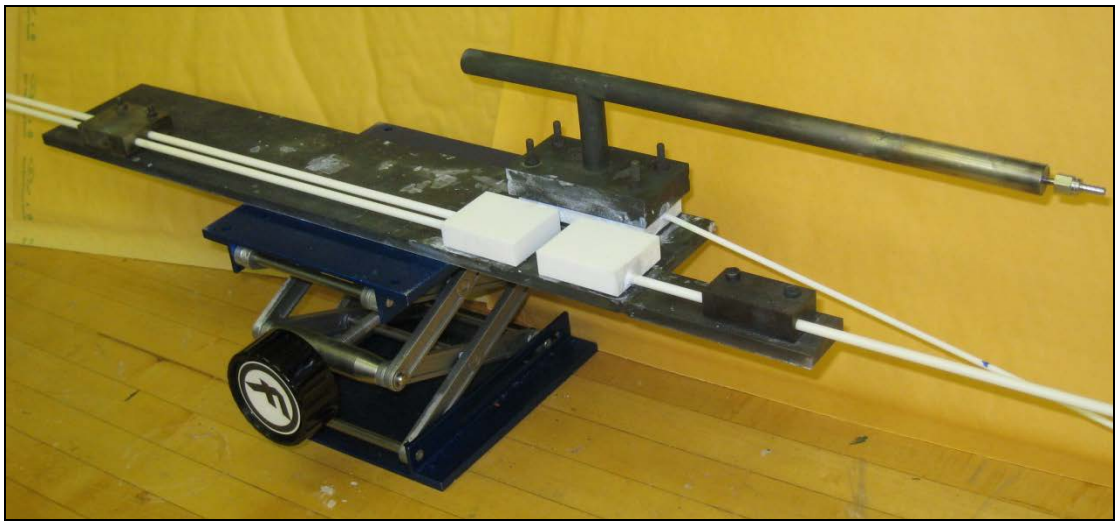

Figure 5. The actual microchemical reactor system after manufacturing and assembly.

In the system, the main microchemical reactor (part 1) and elbows (part 2) were made from MACOR (Corning Incorporated) (manufactured by Technical Product, Inc.), a type of glass ceramics that combines excellent thermal properties and machinability. High-purity nonporous alumina tubes (McMaster-Carr) were used to connect the main microreactor part and elbows together, transport gas entering and leaving the reactor, and provide mechanical robustness for the system.

Moreover, inert gas protection system was made from RA330 (Rolled Alloys), a special high-temperature alloy that has an exceptionally high thermal and oxidant resistance up to 1204 ^{o}C. This device was specially designed and placed on top of the main microreactor to prevent gas leaking from the top of reaction chamber. Also, since the entire system was very sensitive to

outer forces and slight displacements could cause the system to fail especially at high temperature conditions, fixing blocks (part 5) and the bottom supporting plate (part 6) were made from RA330 to guarantee all parts can be located at the correct position after assembly. All RA330-based were manufactured at a local machine shop.

Due to the importance and complex structure of the main microchemical reactor, a detailed description of its design is introduced in Chapter 3.2. A key feature in the main microchemical reactor is the feeding system for gas streams at reactor inlet, a proper design of which determines the mixing efficiency of fuel and oxidant. Therefore, in Chapter 3.3, a numerical model is introduced to understand the mixing behavior, as well as demonstrate the sufficient mixing efficiency of the interdigital micro-channel array configuration of the main microchemical reactor. Moreover, another two important aspects of this system are: 1) the design of the sealing interfaces, which is crucial to guarantee a stable operation of the system; 2) the design of a novel in-situ measurement device to allow the acquisition of spatially-resolved profiles of temperature and species composition. The contents of these two parts are not covered in the main text but can be found in Appendix A.

3.2 THE DESIGN OF THE MAIN MICROCHEMICAL REACTOR

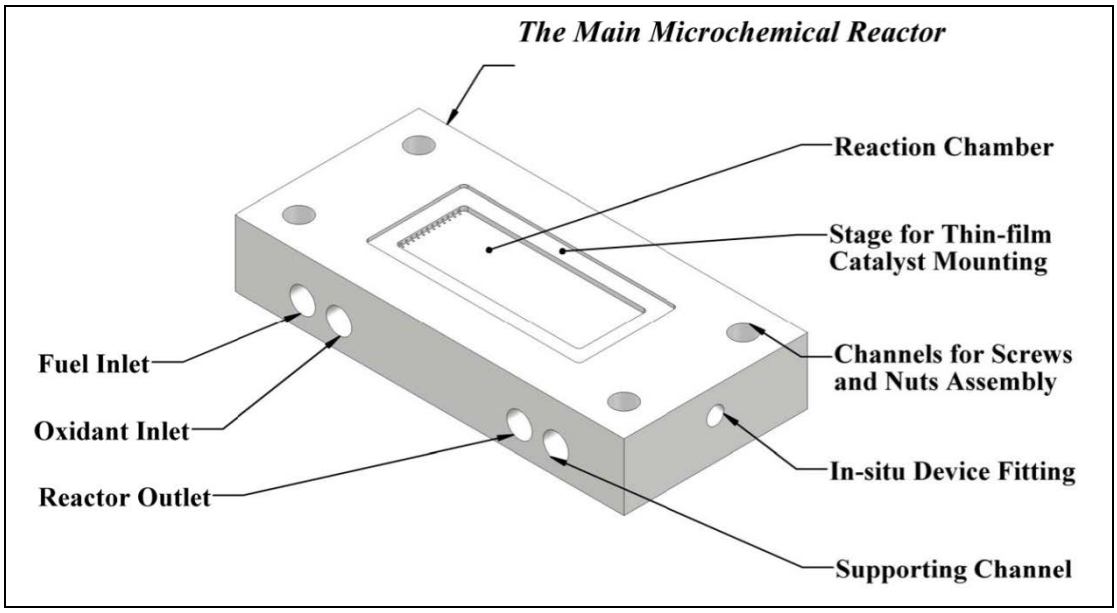

Figure 6. Three dimensional view of the main microchemical reactor (drawn in AutoCAD 2009)

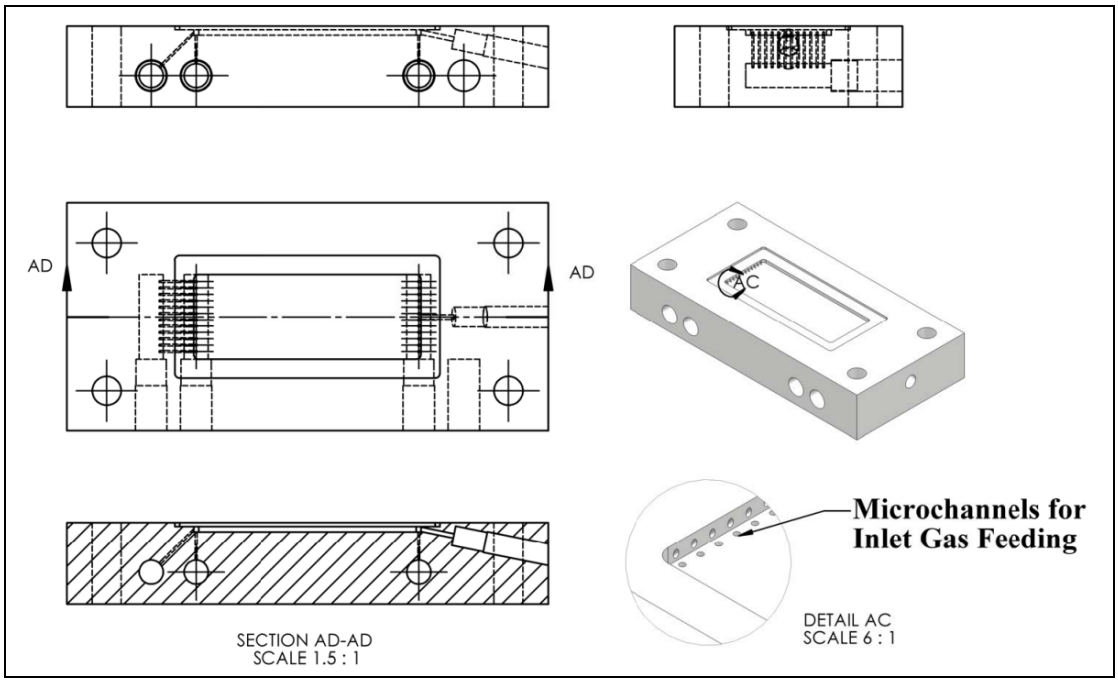

Figure 7. Multiple views of the main microchemical reactor: the standard three views with hidden lines, crop view and detail view for interdigital micro-channel series (drawn in AutoCAD 2009)

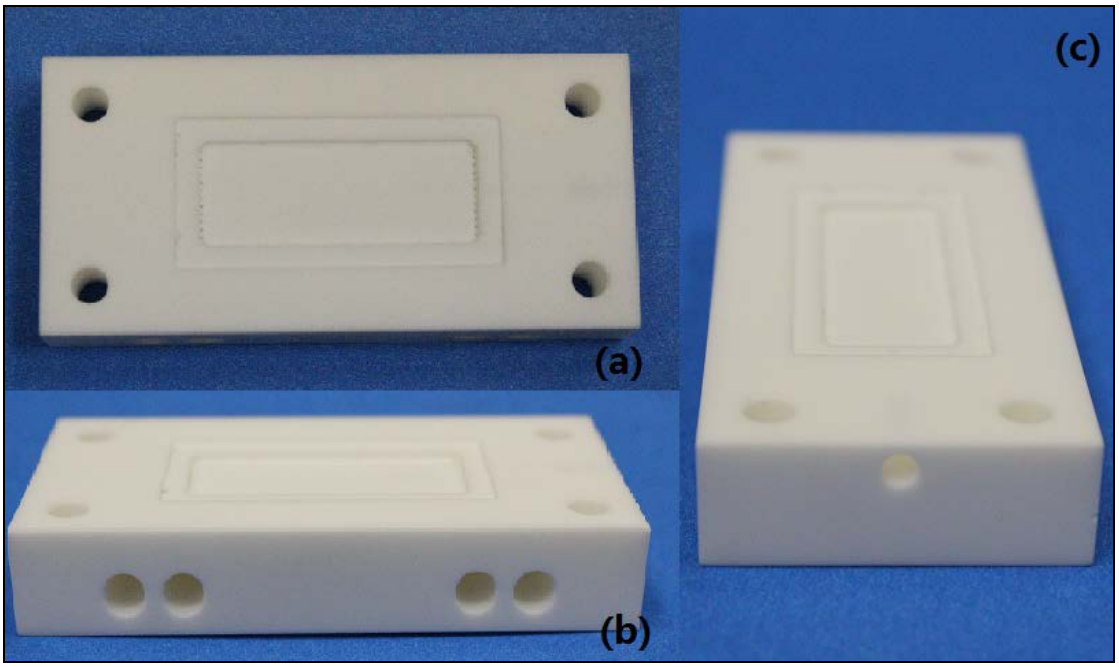

Figure 8. Photo of the actual main microchemical reactor with multiple views.

Figure 6, 7 and 8 shows the detailed design of main microchemical reactor part, which is the core of the microchemical reactor system. On the left side, two reactor inlets were created, allowing fuel and oxidant to feed into the reactor system separately, thus avoids the occurrence of potential homogeneous pre-reactions under high temperature environment. To guarantee the mechanical robustness, two channels were also designed on the right side. One channel is used to guide the gas stream out of the system and the other is used for supporting the reactor by inserting a high-purity alumina tube to connect to the right elbows. The reason for such a symmetrical design is that, applying a single-channel configuration on the right side always leads to reactor failure due to the mechanical fragility at the joint interface between reactor and MACOR elbows. However, it has been tested and proven that using two parallel alumina channels are sufficient to provide mechanical robustness.

Additionally, staged rectangular grooves were designed on the top of main reactor part. The larger groove was designed to support the thin-film catalyst with silicon chip as substrates, while the smaller one acts as the reaction chamber. Moreover, as shown in Figure 7 (right corner), micro-channel arrays (Φ 0.012" pattern of 12 holes, 0.04" spacing) were created to connect inlet and outlet channels with the reaction chamber. Such design at the inlet side will provide a uniform gas feeding as well as fast mixing between fuel and oxidant due to the interdigital direction of the two microchannel arrays.

Lastly, at the exit end, a small channel was designed (Φ 0.134", 5.00^{o} slope) to bond with a ceramic tube thorough which the fused quartz capillary (SIS, Inc. ID 0.110 mm, OD 0.170 mm) or thermocouple (Omega Engineering, Inc. type K, ID 0.254 mm) could be inserted for spatially resolved measurement. This part serves as the interface to connect the main reactor with the data acquisition device for spatially resolved profiles, which will be described in detail in Appendix A.

3.3 THE DESIGN OF THE FEEDING SYSTEM AND CFD SIMULATION

As mentioned in Chapter 3.2, a key feature of main microchemical reactor is the design of the feeding system, which enables fast mixing of two separate gas streams by the interdigital micro-channel array structure. In this chapter, the mixing effectiveness of the design is verified by basic CFD computations. Since a detailed description of modeling procedure for a similar but more advanced model will be covered in Chapter 5.0, this chapter only briefly introduces how this model has been developed, and more focuses on presenting and discussing simulation results for the mixing efficiency.

3.3.1 Model Physics and Governing Equations

A 3D model was developed and implemented in COMSOL Multiphysics, which considered fluid flow and mass transport in an isothermal environment. The mixing behavior was modeled at 25 ^{o}C and therefore reaction kinetics was not considered. Since mixing could proceed faster at higher temperature, the mixing efficiency derived from this model could be used as lower bounds.

In this model, the incompressible formulation of continuity equation and Navier-Stokes were coupled to capture the flow behavior. The formulations of both equations at steady-state condition are

Equation of continuity (steady state)

$$\nabla \cdot \mathbf{u} = 0 \qquad \text{(Eqn. 3.1)}$$

where $\mathbf{u}$ (m/s) is the velocity vector.

Incompressible formulation of Navier-Stokes equation (steady state)

$$\rho \mathbf{u} \cdot \nabla \mathbf{u} = -\nabla p + \nabla \cdot \left(\mu \left(\nabla \mathbf{u} + (\nabla \mathbf{u})^{T} \right) - \frac{2}{3} \mu (\nabla \cdot \mathbf{u}) \mathbf{I} \right) + \mathbf{F} \qquad \text{(Eqn. 3.2)}$$

where p (Pa) is pressure; μ (Pa·s) denotes mixture viscosity and $\mathbf{F}$ (N/m^3) is the volume force vector.

Moreover, chemical species are transported through diffusion and convection, and the following mass balance equation is applied

$$\frac{\partial c}{\partial t} + \mathbf{u} \cdot \nabla c = \nabla \cdot (D \cdot \nabla c) + R \qquad \text{(Eqn. 3.3)}$$

where c (mol/m^3) is the concentration of chemical species; D (m^2/s) denotes the diffusion coefficient; R (mol/(m^3·s)) is the net formation rate of the species; and **u** (m/s) denotes the velocity vector.

In equation 3.4, binary diffusion coefficients are used and can be calculated based on the kinetic gas theory

$$D_{AB} = 2.66 \times 10^{-2} \frac{\sqrt{T^3 (M_A + M_B) / (2 \times 10^3 M_A M_B)}}{p \sigma_A \sigma_B \Omega_D} \qquad \text{(Eqn. 3.4)}$$

where D_{AB} (m^2/s) is the binary diffusion coefficient; M_A and M_B (kg/mol) are molecular weight of species A and B, respectively; σ_A (Å) denotes the characteristic length of the Lennard-Jones/Stockmayer potential; Ω_D represents the collision integral.

3.3.2 Geometry Settings and Modeling Procedures

As Figure 9 shown below, three different kinds of geometrical structures of the feeding system have been studied numerically, i.e. (a) parallel mixing; (b) interdigital mixing (blank reactor) and (c) interdigital mixing with silicon substrate. The purpose of comparing (a) and (b) is to understand two different type of mixing mechanisms. Also, to mimic actual experiment conditions, in which silicon chips can stacked into the reactor to adjust the gap size, geometrical configuration shown in part (c) is also included.

The dimensions of the reaction chamber for modeling were careful chosen to match the actual microchemical reactor part. The height was set to 900 μm, which was exactly the value for the actual reactor. To reduce computation efforts, only three channels were modeled to represent a complete micro-channel array, with both left and right walls treated as symmetry planes. The

length of reaction chamber was also shortened to 5 mm (~1/7 of total length), which was verified to be sufficient to achieve a complete mixing for all configurations.

Hydrogen and oxygen were selected as the model gases for the mixing study. Flat velocity profiles were imposed for H_2 and O_2 at corresponding feeding inlets. For mass balance, constant concentrations of H_2 and O_2 were applied at inlets, which were derived based on ideal gas law. The H_2/O_2 ratio (vol. based) was adjusted by changing the linear velocity of each gas species at reactor feeding inlets. In this work, this value was set to 1 for simplicity. Moreover, the residence time (RT) was adjusted systematically from 0.3 sec to 0.1 and 0.03 sec, with the corresponding volumetric flow rate at inlet to be 25, 80 and 270 sccm, respectively. This range of volumetric flow rate was expected to be a reasonable one, under which condition the actual reactor will be run in experiment.

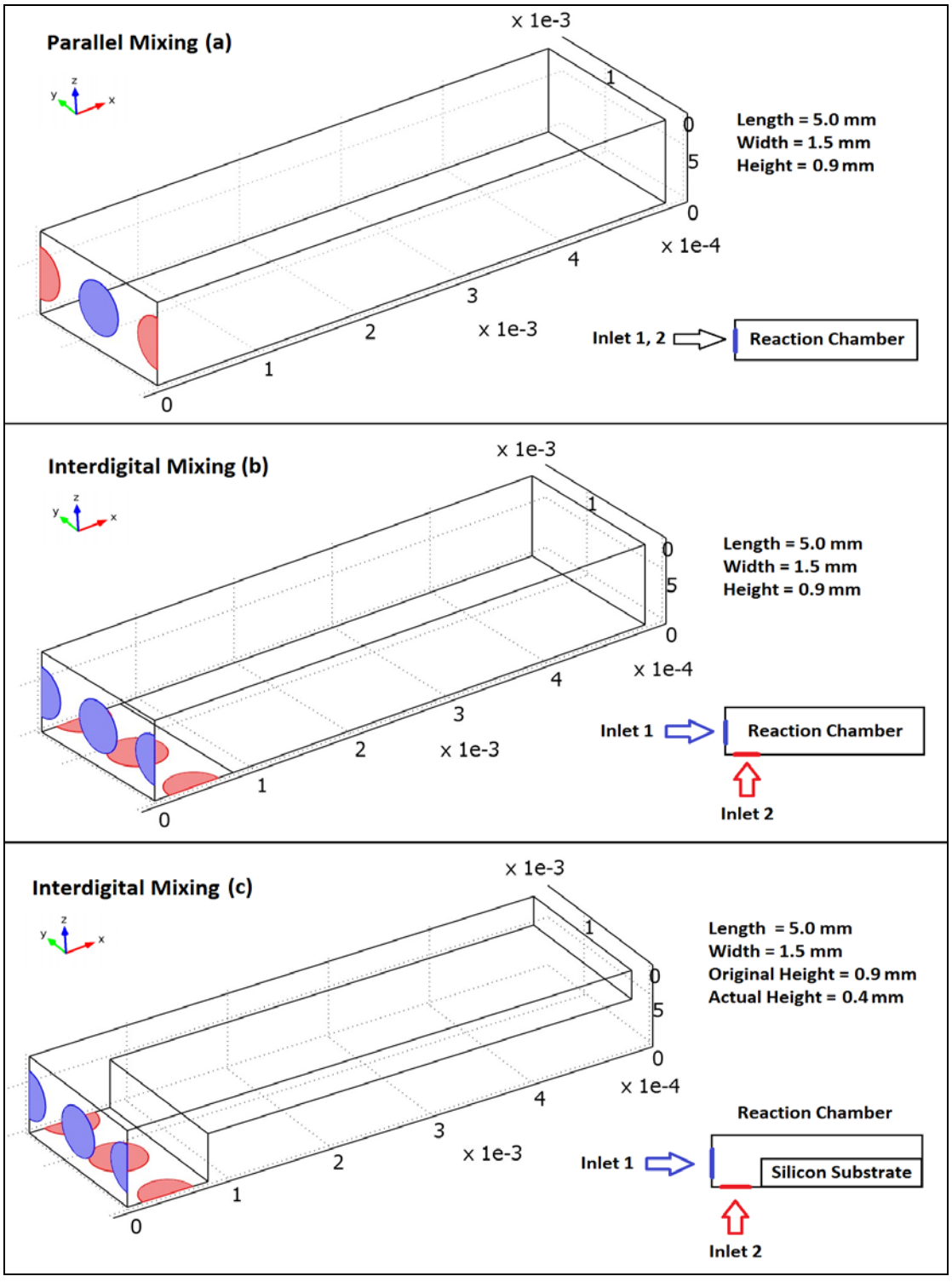

Figure 9. Three geometrical configurations of inlet micro-channel arrays (Φ = 0.019") for numerical study of mixing efficiency: a) parallel mixing; b) interdigital mixing without silicon substrate stacking; c) interdigital mixing with silicon substrate stacking.

3.3.3 Results and Discussion

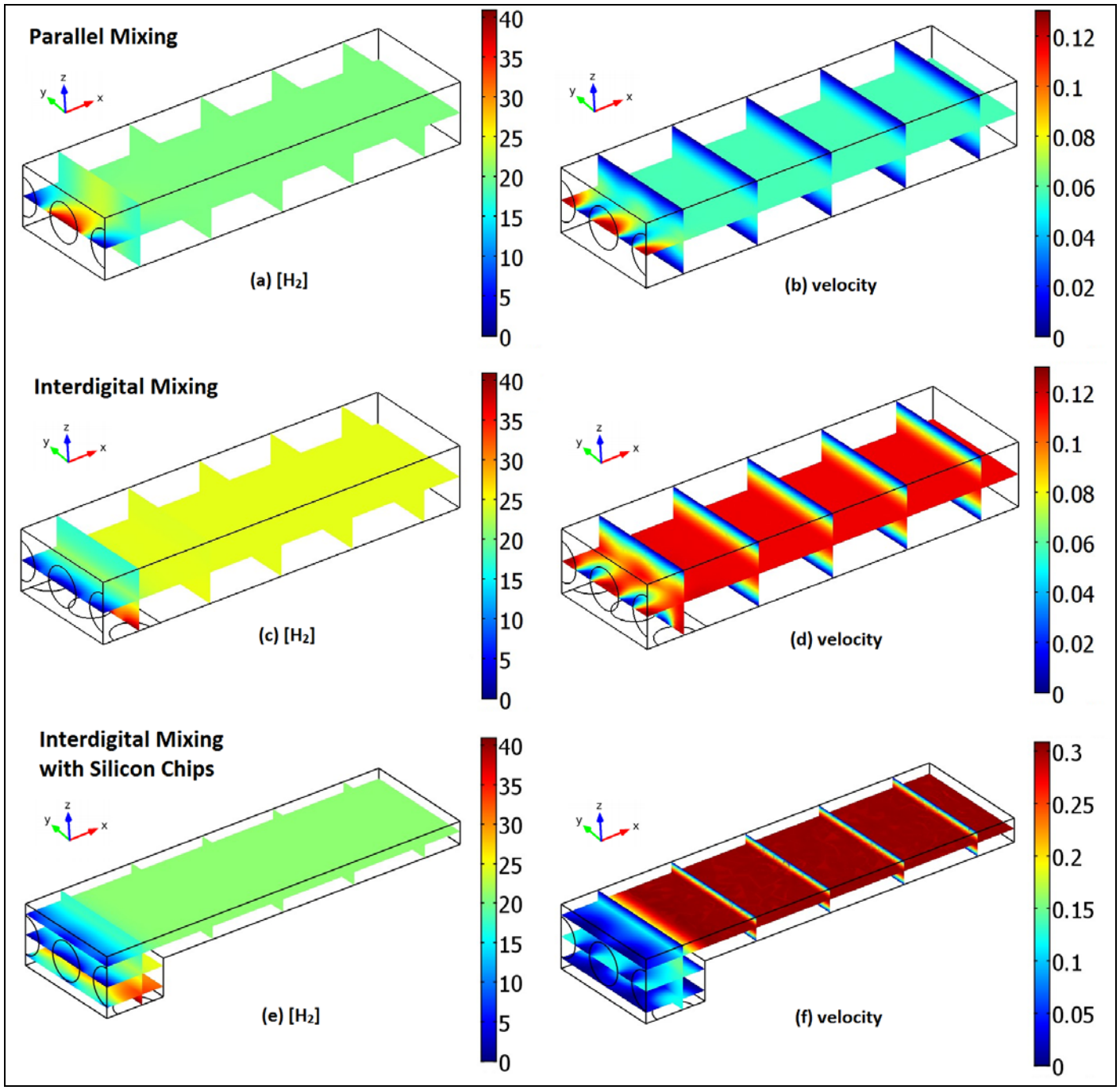

Figure 10. 3D profiles for H_2 concentration (mol/m^3) (left) and velocity field (m/s) (right) under three geometrical configurations of the feeding system: a) parallel mixing; b) interdigital mixing in blank reactor; c) interdigital mixing with silicon substrate stacking; T = 25 ^{o}C, v_0 = 0.12 m/s (RT = 0.3 sec), H_2/O_2 = 1 (vol. based).

Figure 10 shows the 3D profiles of H_2 concentration (a, c, e) and velocity field (b, d, f) to demonstrate the mixing behavior under three different geometrical configurations. Generally, it is clear that good mixing is achieved for all three cases and H_2 concentration is almost constant beyond the first millimeter at reactor inlet. It also takes shorter time for interdigital mixing to achieve a more flat concentration profile against the x-axis direction, compared to parallel mixing. The decent mixing effect might be due to the relatively long residence time for the gas streams.

In order to gain deeper insight into the mixing behavior, 1D profiles for H_2 concentration under three different mixing configurations were acquired. 1D data were sampled on the line which connected the center of the plane of inlet and outlet. The exception was for the third configuration, in which centers of inlet and outlet planes were not on the same height. Therefore, a line which was parallel to the x-axis and connected to the center of the exit plane was used. Due to the relative simple geometrical configurations, these profiles were believed to capture the overall mixing performance in good accuracy.

As Figure 11 shown, for all three geometrical configurations, curves for RT at 0.10 and 0.03 sec do not have much difference. It takes around 1.5 mm, 1.0 mm and 0.8 mm in distance (x-axis) to achieve a complete mixing, which can be seen by the flat H_2 concentration profiles afterwards. At the shortest RT investigated (0.03 sec), H_2 concentration profiles show drastically different yet interesting behavior. For the parallel mixing configuration, it takes longer distance (~2.5 mm) for a complete mixing, compared to two cases with shorter RT. For the second configuration, since H_2 is fed from the micro-channel array located on the bottom of reaction chamber (Figure 11: inlet 2 in part b), when inlet velocity is large, there is a overshoot for H_2

concentration signal which then decreases gradually to the value for well mixing at ~2 mm. However, this overshoot effect is lessened when silicon chips are stacked in the reaction chamber, as (c) presented, and shorter distance is needed to complete the mixing. This can be explained by that the presence of silicon substrates forces gas streams to travel upwards until they reach and enter the thin reaction chamber.

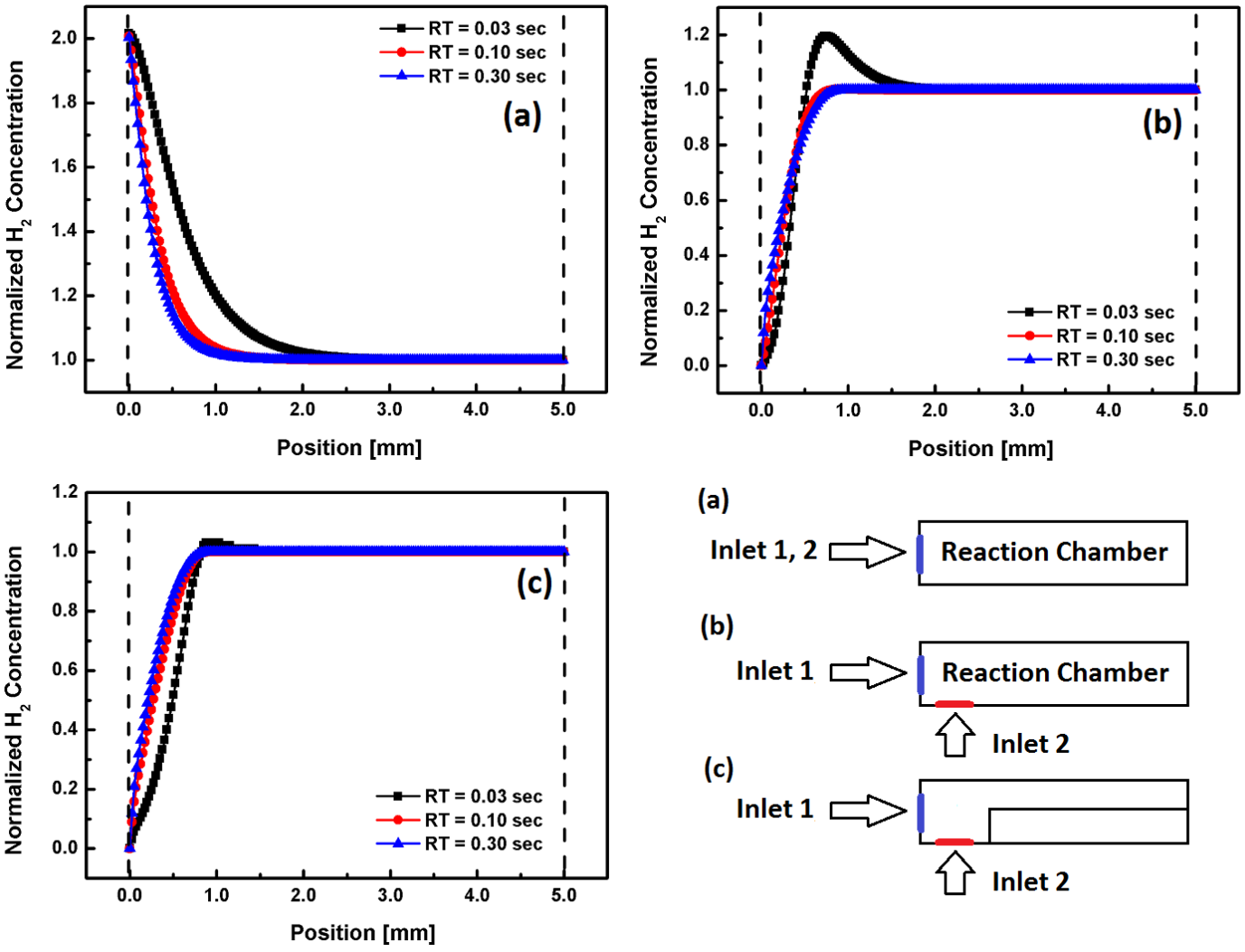

Figure 11. 1D profiles for the normalized H_2 concentration (mol/m^3) (left) under three geometrical configurations of the feeding system: a) parallel mixing; b) interdigital mixing for blank reaction chamber; c) interdigital mixing with silicon substrate stacking; inlet velocity was set to 0.12 m/s (RT = 0.30 sec), 0.36 m/s (RT = 0.10 sec) and 1.20 m/s (RT = 0.03 sec), respectively; T = 25 ^{o}C, H_2/O_2 = 1 (vol. based).

Overall, for the three configurations investigated, numerical simulation demonstrates that the complete mixing between two gas streams can be realized in the first 3 millimeters at reactor inlet, which is a major benefit from the using of a micro-scaled reactor. Even through the geometrical configuration for modeling was slightly different from the actual microchemical reactor system, it is believed a similar mixing behavior and efficiency is expected. Also, under high temperature conditions where experiments take place, the mixing efficiency can be enhanced due to the increase of diffusion coefficients (Eqn. 3.4).

3.4 CONCLUSION AND SUMMARY

In summary, a MACOR-based microchemical reactor system was designed and manufactured which serves as a general platform to study the coupling effects of homogeneous-heterogeneous reaction systems. By taking advantage of the micro-scaled system and the interdigital micro-channel array configuration, the sufficient mixing efficiency was achieved and confirmed by numerical modeling. Before proceeding to the next chapter, the overall performance of this microchemical reactor system is summarized as follows: 1) temperature range of stable operation: from 25 ^{o}C to 800 ^{o}C; 2) sealing performance: overall leakage less than 5% (maximum inlet volumetric flow rate = 150 sccm); 3) range of the height of reaction chamber to be adjusted: from 240 μm to 680 μm; 4) allow the fitting of thin-film catalyst in the main reactor; 5) able spatially resolved measurement of temperature and species concentration.

4.0 EXPERIMENT ON OXIDATIVE COUPLING OF METHANE (OCM)

4.1 INTRODUCTION TO OCM

Due to the enormous proven reserves of natural gas worldwide (1.9×10^{14} m^3) [43] with methane (CH_4) as the principle component, there is a strong economic incentive to convert methane into more valuable chemicals [44, 45]. During the past thirty years, most of the research on the direct conversion of methane has been focused on oxidative coupling of methane to produce ethylene, an important feed-stock of petrochemical industry, which can also be converted to liquid transportation fuels by oligomerization reaction.

OCM reaction usually takes place between 700 ^oC and 950 ^oC and the global reaction can be written as:

$$2CH_4 + O_2 \leftrightarrow C_2H_4 + 2H_2O, \qquad \Delta H^0_{rxn} = -281.4 \ \ kJ/mol$$

The possibility to achieve reasonable C_{2+} yields through OCM first becomes apparent after the publications by Bearns and coworkers in 1984 [46] and Ito et al. in 1985 [47]. In their papers, Bearns reported 58% C_{2+} selectivity at 5% CH_4 conversion by using PbO/Al_2O_3 as the catalyst, while in Ito's work 50% C_{2+} selectivity at 28% CH_4 conversion was achieved over Li/MgO catalyst. As a potential route for direct upgrading methane to more useful C_2 chemicals, tremendous efforts have been devoted with hundreds of materials been identified as potential OCM catalysts in terms of reactivity. Among these materials, oxides for alkali, alkaline earth and

rare earth metals show highest reactivity, with the highest C_{2+} yield in the range of 15% to 20% in a single pass through the reactor.

However, in today's petrochemical industry, ethylene is produced almost exclusively by steam cracking process, in which alkanes are heated up to around 800℃ and fed to alloy tubes in a furnace to cause homogeneous pyrolysis. Typically, the residence time for the process is ~ 1 second and ~85% C_{2+} selectivity is achieved at ~60% alkane conversion [48]. Clearly, OCM failed to be developed into a commercially available process due to an unsatisfactory C_{2+} yield.

However, extensive research efforts have resulted in an insightful understanding of OCM. It belongs to an unusual catalytic oxidation process that involves both catalytic and gas-phase free radical chemistries, i.e. the H-H coupling reaction. During the OCM process, CH_4 is firstly adsorbed and activated on the catalyst surface, reacted with absorbed oxygen species, to produce CH_3 radicals. Ethane is formed exclusively from gas-phase coupling of CH_3 radicals [47, 49], which is further decomposed into ethylene, the desired product. CO and CO_2 are produced via the oxidation of methyl radicals in the gas phase, as well as deep oxidation processes catalytically. OCM is a very complex chemical process and a detailed description of the reaction network is presented in Chapter 4.2.

Moreover, Chapter 4.3 gives a brief introduction to OCM catalysts, which is a key element to understand OCM process. Among a large variety of potential catalysts, lanthanum oxide (La_2O_3) has been selected for OCM study in this thesis. Thus, the synthesis and characterization method are then fully discussed in Chapter 4.4, on how to prepare and analyze the La-based thin-film catalyst. Then, in Chapter 4.5, a detailed discussion of the experiment methodology for running OCM in the microchemical reactor system is presented. Following this experimental procedure, La_2O_3-catalyzed OCM is fully studied with data gained from both

reactor exit and spatially resolved sampling technique. These results are examined and discussed in Chapter 4.6.

4.2 REACTION NETWORK ANALYSIS

Before moving to the analysis of integral reactor data and spatially resolved profiles, it is necessary to describe the detailed reaction steps in OCM based on reported literatures. Reaction mechanism developed by Marin and coworkers [27, 49-51] were taken as main references to assistant the understanding of OCM reaction kinetics, which consists of detailed elementary reaction steps for both gas-phase and catalytic reactions. The main reaction pathways for OCM reaction on La_2O_3 catalyst were identified and presented in the figure below, which can be divided into 5 groups:

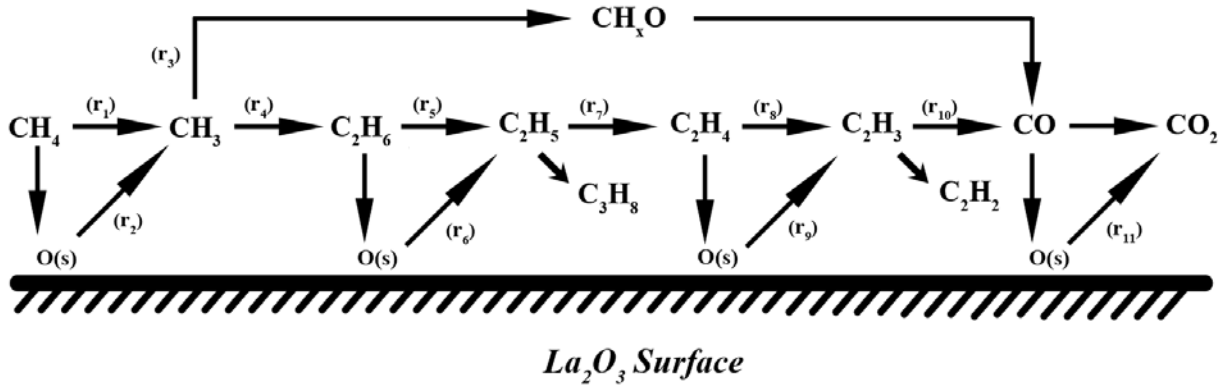

Figure 12. Schematic of main reaction pathways for OCM reaction on La_2O_3-based thin-film catalyst

1) **CH_4 activation (r_1 and r_2):** CH_4 can be activated by breaking C-H bond to form CH_3 radicals, which can occur both in the gas phase and on the catalytic surface. In gas phase, CH_4 reacts with H, O and OH radicals to generate CH_3 radials. However, the dominating

pathway is the activation of CH_4 on reactive La_2O_3 surface, by reacting with surface absorbed oxygen species, producing CH_3 and surface absorbed hydroxyl species.

2) **CH_3 consumption (r_3 and r_4):** One channel is the direct coupling of CH_3 radicals in the gas phase. The rate of this reaction is the second order with respect to CH_3 concentration, and it is a non-activated reaction step [52]. CH_3 radicals can also be easily oxidized in the gas phase via the following chain that ultimately leads to the formation of CO:

$$CH_3\bullet \rightarrow CH_3O\bullet \rightarrow CH_2O \rightarrow CHO\bullet \rightarrow CO$$

This reaction pathway is generally very fast.

3) **C_2H_6 consumption (r_5 and r_6):** In the gas phase, C_2H_6 can be consumed via $C_2H_6 \rightarrow C_2H_5\bullet \rightarrow C_2H_4$ reaction channel (r_5). Also, C_2H_6 can react with surface absorbed oxygen species to produce C_2H_5 radicals by Eley-Rideal type reaction (r_6) [52, 53]. Since C_2H_5 radical is a reactive immediate with trivial net formation rate, also experiment results suggest reaction pathways towards the formation of C_3 species (C_3H_6, C_3H_8) are insignificant. Thus, the consumption rate of C_2H_6 is the summation of r_5 and r_6, which approximately equals to the formation rate of C_2H_4 (r_7).

4) **C_2H_4 consumption (r_8 and r_9):** Similar to C_2H_6, C_2H_4 can be dehydrogenated in the gas phase (r_8) by reacting with radicals (such as H, O, CH_3), and on catalytic surface by Eley-Rideal type reaction (r_9), both lead to the formation of C_2H_3. C_2H_3 is highly reactive and can be oxidized to form CO in the gas phase via the following reaction pathways:

$$C_2H_3\bullet \rightarrow CH_2O,\ CHO\bullet \rightarrow CO$$

Also, the total consumption rate of C_2H_4 (r_{10}) is the summation of r_8 and r_9.

5) **C_1 formation and consumption (r_{10} and r_{11}):** CO can be formed through two reaction pathways: 1) direct oxidation of CH_3 radicals (r_3); 2) oxidation of C_2H_3 radicals (r_{10})

resulted from C_2 (C_2H_4, C_2H_6) re-adsorption and reaction on the catalytic surface. CO can be oxidized to CO_2 both in gas phase and on surface (r_{11}), while the latter one is the primary reaction step [54].

4.3 CATALYST FOR OCM REACTION

Among a large variety of oxides explored as catalysts for OCM, rare each oxides, mainly M/La_2O_3 and Sm_2O_3 (M = Ca, Ba, Sr, etc.) are most active to convert CH_4 into higher hydrocarbons. Pure La_2O_3 was initially been tested in OCM at oxygen-limited conditions and ~47% C_2 selectivity was achieved at 9.4% of CH_4 conversion at 725℃ [55]. Later on lanthanum-based catalyst was improved by the moderate addition of barium (Ba) content and a yield of ~18% for C_{2+} was achieved [56]. The high reactivity of lanthanide oxides in OCM is mainly due to their intrinsic ability to form active $O^-_{2(s)}$ species, which are highly movable in the hexagonal structures [57]. Another important species being reported is $O^-_{(s)}$, which has been identified as one of the most active oxygen sites based on periodic density functional theory (DFT) study [58]. These transient ion species are believed to serve as active centers on which CH_4 is reacted to form CH_3 radials, generating C_2 products by CH_3 dimerization afterwards. In fact, Kazansky and co-workers have proposed the following mechanism that may occur on lanthanide oxides with the presence of oxygen [59]:

$$O_2(gas) \longleftrightarrow O_{2(s)} \xleftrightarrow{+e^-} O^-_{2(s)} \xleftrightarrow{+e^-} O^{2-}_{2(s)} \longleftrightarrow 2O^-_{(s)} \xleftrightarrow{+2e^-} 2O^{2-}_{(s)}$$

In this thesis, since the target is not to search for a better catalyst for OCM reaction, but to investigate the HH coupling behavior under high temperature conditions, pure La_2O_3 has been

selected as the model catalyst. It is a catalyst which is sufficiently effective to generate CH_3 radicals and able to leads to a decent yield for C_2 products.

4.4 CATALYST SYNTHESIS AND CHARACTERIZATION

Silicon substrates (Cemat Silicon S.A.) were cut by using a dicing saw (DISCO, type DFD6240) to two different dimensions based on the geometry dimensions of the main microchemcial reactor part (see Chapter 3.2). The dimensions of silicon substrates after cutting are: 1) top substrate, 41.68 mm (length) × 13.00 mm (width); 2) bottom substrate, 34.00 mm (length) × 13.00 mm (width). When assembling the reactor system, the top substrate is used to place on top of the reaction chamber, while the bottom one fits inside the reaction chamber.

The La_2O_3 catalyst film was prepared by dip coating method. The lanthanum nitrate hexahydrate ($La(NO_3)_3 \cdot 6H_2O$, >99.0%, Sigma-Aldrich) was used as the precursor without further purification. Silicon substrates used for coating were ultrasonically cleaned for 10 minutes in acetone and rinsed for several times with ethanol. 1 gram of $La(NO_3)_3 \cdot 6H_2O$ was dissolved in 30ml ethanol (>99.8%, Pharmco-AAper) and stirred for 1 hour to prepare the coating solution. The substrate was dipped into the coating solution for 1 minute and removed. It was then quickly inserted into a tube furnace which was preheated to 600^{o}C for 30 minutes. The dip coating and heating were repeated for 5 times to ensure a uniform coating. The coated substrate was finally acquired after calcination at 750 ^{o}C for 4 hours with a flow of air (flow rate, 200 ml/min).The catalyst film was characterized by Philips XL-30 field emission scanning electron microscope (SEM). The elemental analysis was performed by energy-dispersive x-ray analysis (EDX) equipped on Philips XL-30 SEM.

4.5 EXPERIMENTAL PROCEDURE

All experiments were carried out in the microchemical reactor system described previously. CH_4 (99.5%), O_2 (99.99%) and He (99.999%) (Metheson) were controlled by mass flower controllers (MKS Instruments) and fed into the reactor connected by plastic tubes (Tygon). Since there were only two inlet pipes in the system, O_2 and He were premixed before feeding to the reactor, while CH_4 was fed through the other channel. Thus, CH_4 and O_2 could only be contacted after entering the reaction chamber, which was crucial because any pre-reaction could be completely avoided.

Each time before running the experiment, the microchemical reactor system needed to be assembled based on the following procedure: 1) locate the bottom supporting plate and place the main reactor in the correct position, fixed by left and right fixing blocks; 2) place the bottom silicon substrates in the reaction chamber; 3) insert the fused quartz capillary/thermocouple into the reaction chamber through the spatially resolved sampling channel; 4) fit the upper silicon substrate on top of reaction chamber; 5) insert a well-cut graphite gasket between the main reactor part and inert gas protection system (see Appendix A), pressing it against graphite gasket to achieve a closed sealing line; 6) use bolts and nuts to tighten the entire reactor system.

It should be emphasized that, due to the fragility of the ceramic-based reactor system, prior to assembly, the bottom supporting plate needs to be paced on a well-positioned lab jack with sufficiently large free space at surroundings. Then, the assembly process requires a very careful operation that strictly sticks to the aforementioned assembly protocols. The disassembly procedure is followed exactly the opposite sequence as for assembly.

Another important aspect that needs to be stressed is the way to change the height of reaction chamber, a key parameter to adjust in this experiment. Generally, we achieve this by

stacking silicon chips into the chamber. The initial height of reaction chamber before without silicon substrates is designed to be 900 μm. Since silicon substrates with two different thicknesses has been selected, i.e. 220 (thin) and 350 μm (thick), respectively, by selecting and putting one or two substrates into the chamber, we can systematically adjust its height from 680 μm (1 thin), to 460 (2 thins) and to 330 μm (1 thin, 1 thick).

After the reactor assembly, the entire reactor system was placed into a tube furnace (Lindberg Blue M, Thermal Scientific) for heating treatment. OCM experiment was then conducted at elevated temperatures from 25 ^{o}C to 800 ^{o}C. Several important parameters, i.e. helium dilution, C/O ratio as well as residence time were systematically adjusted at specified temperature when a decent methane conversion was achieved. Gas chromatography (MicroGC 3000A, Agilent) was used to analyze chemical compositions of gas stream at reactor outlet. GC was equipped with two channels and was able to quantify all the main species from OCM reaction: 1) He, H_2, CH_4, O_2, CO at channel 1 (carrier gas: Argon; column: molecular sieve; detector: TCD); 2) CO_2, C_2H_4 and C_2H_6 at channel 2 (carrier gas: Helium; column: plot U; detector: TCD). Each time ~20 minutes was necessary to complete the entire analysis after steady state was achieved.

Molar flow rates of all species were calculated by using helium as the internal standard. Conversion and selectivity were then calculated based on the following equations:

$$X_j = \frac{F_{j,in} - F_{j,out}}{F_{j,in}} \qquad \text{(Eqn. 4.1)}$$

where j denotes the name of the reactant, i.e. either CH_4 or O_2; $F_{j,in}$ and $F_{j,out}$ (mol/s) represents molar flow rate of species j at inlet and outlet, respectively; X_j denotes the conversion of species j.

$$S_j = \frac{x_j F_j}{\sum_i x_i F_i} \qquad \text{(Eqn. 4.2)}$$

where S_j is the selectivity to species j (on an atomic basis); i denotes the product species at reactor exit; x_i denotes the number of atoms (element carbon) in species i; F_i is the molar flow rate of species i at reactor outlet.

The reliability of experiment data were confirmed by closing atom balances (C, H and O) by calculating molar flow rates for all chemical species at inlet and outlet of reactor system. For all experiments investigated, atom balances were less than ±7%.

Spatially resolved profiles were acquired by manually moving the inserted quartz capillary/thermocouple in the direction of the flow. Measurement began from reactor inlet end, and 14 data points were taken sequentially with a uniform interval of 2.54 mm to cover the entire range of reaction chamber (~36 mm). At each point, a period of 2 minutes was waited to ensure the stability of MS signals. The movement of quartz capillary/thermocouple was accurately controlled by the adjustment of micrometer mounted on the lab jack.

Additionally, during the process of measuring spatially resolved composition profiles, the related mass spectrum (m/z) was set between from 2 and 46, covering the smallest molecule hydrogen (H_2) and the largest carbon dioxide (CO_2). Prior to analysis, MS was calibrated by using helium (He) as the internal standard (m/z = 4), while all other gases were calibrated by using a binary gas mixture with respect to He. Analog scan was performed for all relevant species with main mass peaks identified, which were defined as the one that was larger than 5% of the maximum mass peak signal. A table for fragmentation pattern was then established, which was directly used to convert m/z signals to composition data in the analysis of spatially resolved profiles. Water was determined by closing the O element balance. Also, when measuring the

spatially resolved profiles of chemical composition, Multiple Ion Detection (MID) mode was applied to acquire the intensity information at different m/z values. SEM detector was used and its voltage was set to 970 mV. This detector was thus able to capture weak ion intensity signals due to the presence of small amounts of chemicals in the system, such as signals due to formation of ethane (C_2H_6) and ethylene (C_2H_4).

4.6 RESULTS AND DISCUSSION

4.6.1 Catalyst Characterization and Stability Test

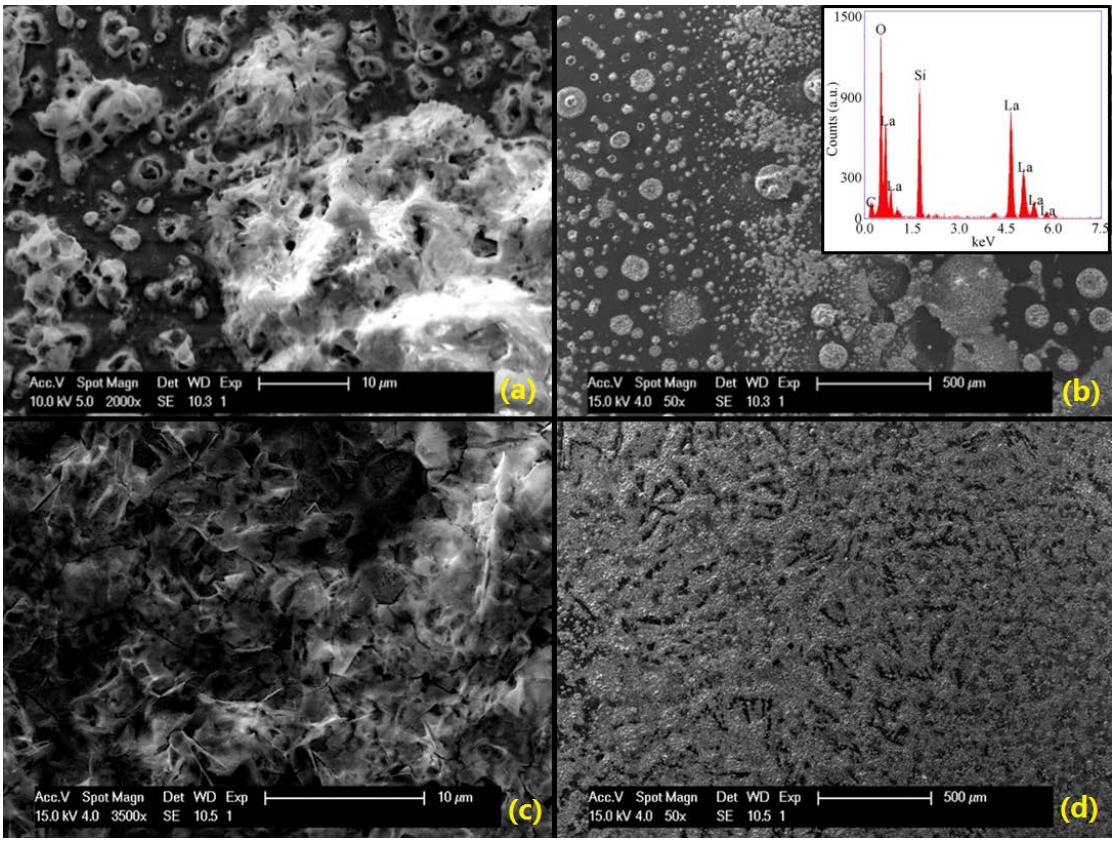

Figure 13. SEM images for La_2O_3 on silicon substrate before (a, b) and after (c, d) OCM reaction.

As shown in Figure 13, SEM images for La_2O_3 catalyst are presented. The La_2O_3 content of the catalyst on silicon substrate was identified by EDX as shown in part (b) (inserted). SEM images indicate by applying dip coating method, La_2O_3 shows decent coverage with porous structure on silicon substrate. During the synthesis, the formation of this structure is due to the immediate ignition of ethanol in the oven, which is preheated to a temperature (600 ^oC) higher than the autoignition point (362 ^oC). Although the La_2O_3 was calcined at 750 ^oC, which is above the crystalline temperature, the porous structure is still well maintained. After the reactions at 800 ^oC, the coverage of La_2O_3 on silicon dramatically increases due to the high temperature. However, the porous structure of the La_2O_3 can still be observed.

Additionally, the stability of La_2O_3-based thin-film catalyst was tested prior by running OCM reaction at 800 ^oC for 10 hours. Composition data for gas mixture at reactor outlet were taken from GC every half an hour. Results suggest the fresh catalyst shows the highest reactivity, which experiences an initial deactivation phase with a loss of 30% of its original reactivity (CH_4 conversion). After that, reactivity of the catalyst was kept as constant. Therefore, the condition of this catalyst was sufficient for further OCM study.

4.6.2 Temperature Profiles

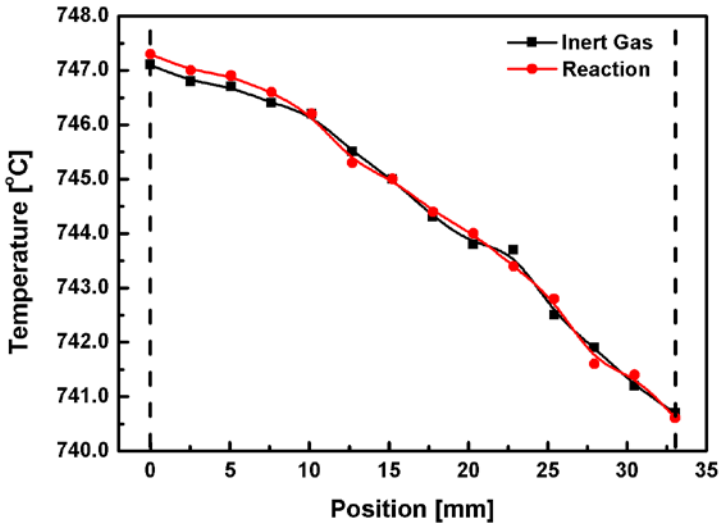

Figure 14. Comparison between two typical spatially-resolved temperature profiles within the reaction chamber with and without OCM reaction at 738.5°C (reactor outlet temperature): 1) pure He flowed through the reactor, flow rate = 20 sccm; 2) with OCM reaction occurring, inlet feed condition: He dilution = 50%, C/O ratio = 2.0, flow rate = 20 sccm

Before performing further experiments, spatially resolved temperature profiles were firstly acquired and compared at elevated temperatures while total volumetric flow rate was maintained as a constant (20 sccm): 1) only He was flowed in the reactor (no reaction); 2) reactive mixture was fed into the system (OCM reaction). Typical temperature profiles were presented in Figure 14 when the reactor outlet temperature was held at 738 °C. Results show that temperature slight decreased towards reactor outlet with maximum temperature difference less than 8 °C. Moreover, temperature profiles were found to be independent of the occurrence of OCM reaction, also was not influenced at all by major operating parameters such as C/O ratio,

helium composition and residence time. Thus it can be fairly argued that a quasi-isothermal environment can be created by the current microchemical reactor system.

Due to the strong exothermicity of OCM reaction, the achievement of the isothermal environment is seemingly surprising but it is what we have expected. The realization of isothermal condition within the reaction chamber was mainly due to the large surface-to-volume ratio, good thermal conductivity of reactor (made from MACOR, thermal conductivity at 25 ^{o}C is 1.46 W/m/K) and decent temperature control of the tube furnace.

Compared with millisecond CPO with extreme thermal gradients (up to 200 ^{o}C/mm) [60, 61], the creation of isothermal environment with accurate control of temperature is significantly meaningful: it dramatically decreases the complexity for reaction kinetics analysis by ruling out the influence of temperature on system behavior. This is a very important foundation for HH investigation in this study.

4.6.3 Conversion and Selectivity

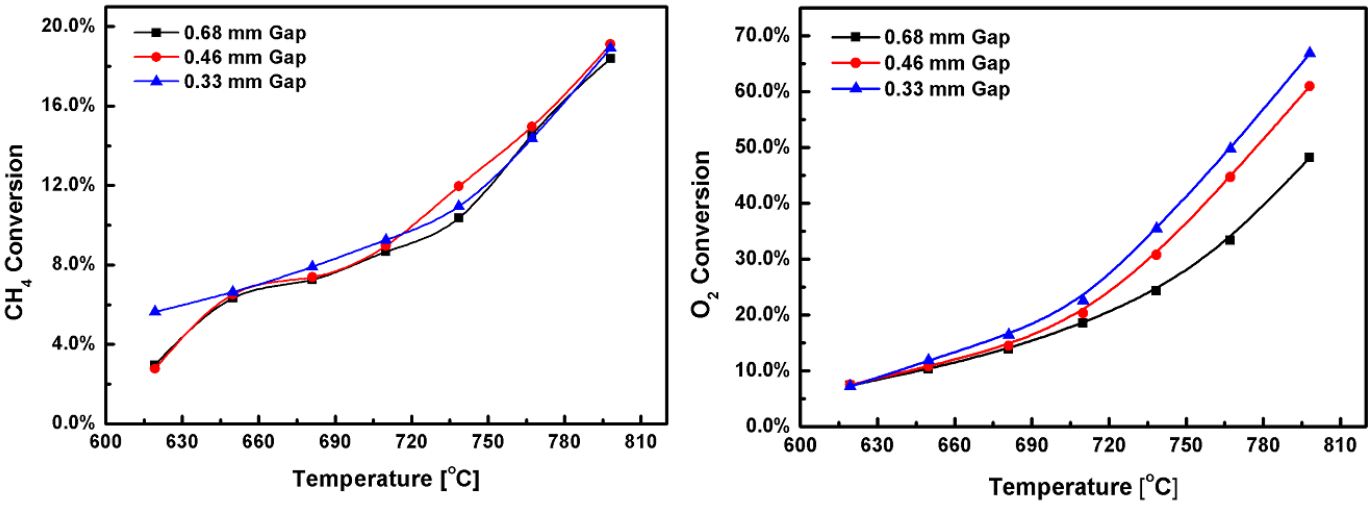

Figure 15. Conversion of CH_4 (left) and O_2 (right) at elevated temperature (measured at reactor outlet) for OCM. Three curves represent different cases by varying the critical dimension (i.e. gap distance) of the reaction chamber. Inlet feed condition: He dilution = 50%; C/O ratio = 2.0; residence time = 0.29 sec.

The influence of temperature on OCM reaction was tested by ramping up the temperature gradually from 620 to 800 ^{o}C, with 30 ^{o}C as the interval, while other important operating parameters (He dilution, C/O ratio, and residence time) are kept as constants. Results suggest that for each gap distance, conversions of CH_4 and O_2 increase at elevated temperatures. Also, CH_4 conversion is barely influenced by the change of gap size, while decreasing gap size enhances O_2 conversion. Beyond the catalytic consumption on reactive surface, O_2 can also be consumed by the oxidation chain in the gas phase which leads to C_1 (CO, CO_2) formation. As Figure 16 shown next, decreasing the gap size shifts the system towards C_1 formation by suppressing CH_3 coupling in the gas-phase. Thus it is not surprising that O_2 conversion increases with decreasing gap size.

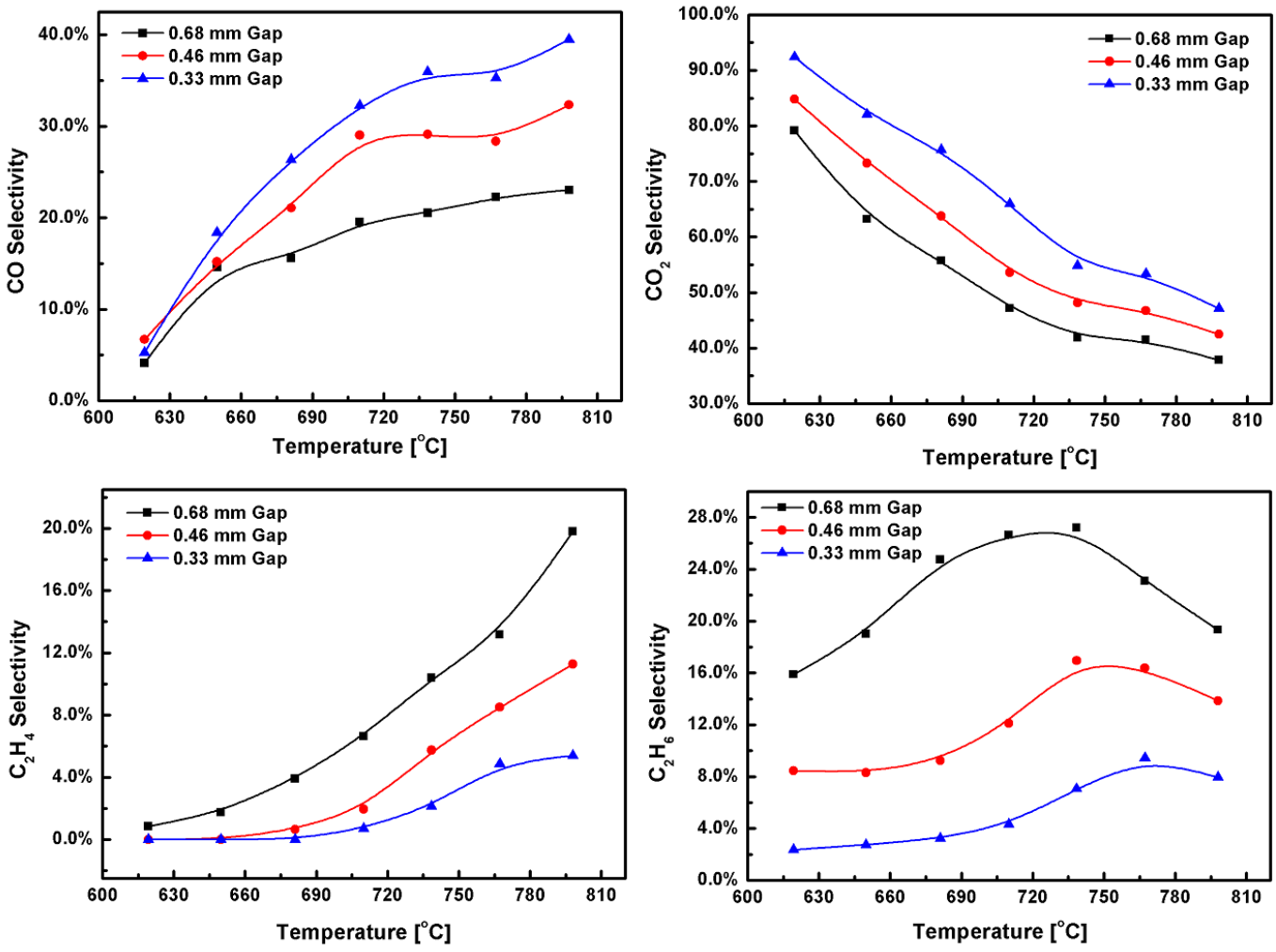

Figure 16. Selectivity to C_1 (CO, CO_2) and C_2 (C_2H_4, C_2H_6) products at elevated temperature in OCM reaction under different gap sizes. Inlet feed condition: He dilution = 50%; C/O ratio = 2.0; residence time = 0.29 sec.

Figure 16 consists four subplots, showing the selectivity to CO, CO_2 (undesired products) and C_2H_4, C_2H_6 (desired products) at elevated temperatures in OCM reaction. For all three cases investigated, as the temperature increases, selectivity for CO and C_2H_4 increases, CO_2 decrease, and more interestingly, C_2H_6 shows a maximum.

Selectivity to C_1 Product:

Generally, we see an increase of CO and decrease of CO_2 selectivity at elevated temperatures for all three cases. Additionally, selectivity to total C_1 (CO + CO_2) species decreases, specifically, from 83.2% to 60.8%, 91.5% to 74.8% and 97.5% to 86.6% for gap size 680, 460 and 330 μm respectively. As Figure 12 suggested, C_1 and C_2 species can be competitively generated from CH_3 radicals. Since C_2H_6 formation is the only step that is second order with respect to CH_3 concentration, increasing temperature results in an increasing supply of CH_3, and the system biases towards C_2 formation. Also, it can be seen that low temperature favors CO_2 formation, while high temperature favors CO formation. This can be explained by that gas phase is playing an increasingly important role as temperature increases. It is well known that CO_2 in OCM is mainly formed catalytically [62] and CO is formed by oxidation of CHO radical in the gas phase. Also, gas phase reaction is generally second order with respect to species concentrations while surface reaction has first order dependence. Thus, as temperature increases, gas phase reaction increases more than catalytic reactions, resulting in an increase of selectivity to CO, as well as a decrease of selectivity to CO_2.

Moreover, decreasing the gap distance leads to an increase of both CO and CO_2 selectivity, while suppresses the formation of C_2 products. As we know that decreasing the gap size leads to an increase of surface-to-volume ratio, thus catalytic reaction can be enhanced against gas-phase reactions. More specifically, as can be seen from Figure 16, decreasing the gap size enhances reaction steps r_6 and r_9, leading to more C_2H_5 and C_2H_3 radicals escaping to the gap phase. These radicals are highly reactive and can be quickly oxidized to CO by chain oxidation pathways in the gas phase. Catalytic oxidation of CO to CO_2 (r_{11}) is also enhanced due

to gap size effect. Therefore, decreasing the gap size can increase the selectivity to both CO and CO_2.

Selectivity to C_2 Products:

Under all gap size cases, selectivity curves for C_2H_4 show a monotonic increase at elevated temperature. Also, less C_2H_4 is formed as channel height decrease. The monotonic increase of C_2H_4 selectivity can be easily explained by the fact that C_2H_4 can only be generated via $C_2H_6 \rightarrow C_2H_5\bullet \rightarrow C_2H_4$ reaction pathway. As mentioned in Chapter 4.2 for reaction network analysis, the dehydrogenation steps for C_2H_4 (r_9) and C_2H_6 (r_6) are catalytically dominant. At a fixed gap size, for species C_2H_4, the major formation steps (r_6, r_7) is expected to increase faster than the consumption step r_9, as temperature increases. Therefore, the net formation rate of C_2H_4 increases. The relative importance of reaction rates can be verified by the smaller activation energy of C_2H_4 react on La_2O_3 surface (E_a = 131.4 kJ/mol), compared to the one for C_2H_6 (E_a = 166.2 kJ/mol) [50]. Additionally, decreasing the gap size can enhance catalytic dehydrogenation reaction pathways of C_2 species that ultimately lead to C_1 formation, resulting in a shift of C_2H_4 selectivity curve towards lower value.

Curves for C_2H_6 selectivity show three interesting trends: 1) a gradual increase is initiated at low temperature until a maximum value reached, then accompanied by a rapid decrease towards highest temperature investigated; 2) decreasing the gap size can suppress C_2H_6 formation; 3) decreasing the gap size shifts the peak selectivity towards higher temperature. As already mentioned in discussing the trend for C_1 selectivity, low temperature favors C_1 formation. In other words, the ratio between the rates of direct oxidation and coupling (r_3/r_4) is relatively high at low temperature, due to the second order dependence of CH_3 concentration for

the coupling step. This ratio gradually decreases as temperature goes high. Surface dehydrogenation steps for C_2 products (r_6, r_9) also increase, but they are expected to be the first order dependence on C_2 concentrations. Thus, the net result is the dominating role of CH_3 coupling step, leading to an increase of C_2H_6 selectivity. However, the non-activated nature of the coupling step eventually makes C_2H_6 consumption steps comparative at higher temperature. Then selectivity to C_2H_6 begins to decrease, resulting in a corresponding increase in C_2H_4 selectivity.

When fixing the temperature and decreasing the gap size, r_4 is expected to be unchanged due to two reasons: 1) the supply of CH_3 radicals keeps unchanged, indicated by the fact that CH_4 conversion is barely influenced by gap size (Figure 15); 2) r_3/r_4 ratio is kept unaffected since temperature is constant. However, decreasing the gap size can significantly enhance r_6 while suppress r_5 due to the increase of surface-to-volume ratio. Since r_6 is the dominating step [52], the net result is the increase of r_7. Therefore, C_2H_6 selectivity curve shifts towards lower values as gap size decreases.

At high temperature conditions, the increasing formation of C_2H_4 is mainly responsible for the decrease of C_2H_6 selectivity. At the peak point for C_2H_6 selectivity curve, the rate for C_2H_6 dehydrogenation (r_7) is reaching sufficiently large values to prevent further formation of C_2H_6, which can be achieved under a condition of high temperature or high C_2H_6 concentration, or the combination between the two. As the gap distance decreases, the system is biased towards C_1 formation, leading to a lower value of C_2H_6 concentration. While the formation rate of C_2H_6 (r_4) may be enhanced due to spatial confinement effect (the reduced gas-phase volume may increase CH_3 radical concentration), the only way to prevent further C_2H_6 formation is to let the system go to higher temperature to make r_3 competitive.

Dilution Effect:

The dilution effect was studied by varying the He composition from 50% to 90% and the results are presented in Figure 17. Results suggest that increasing concentration of He only slightly increases CH_4 conversion. Also, as He concentration continuously increases, selectivity to CO, C_2H_4 and C_2H_6 decreases, while selectivity to CO_2 increases. The trends can be explained by the change of relative importance of gas-phase versus catalytic reactions. Increasing inert gas dilution can lower the formation rates of C_2 species, which generally belongs to second order dependence on species concentration in the gaseous phase. Less CH_4, C_2H_4 and C_2H_6 due to increasing inert gas dilution can suppress dehydrogenation steps for C_1 and C_2 species on the catalytic surface, resulting in an increase of surface oxygen availability. This ultimately enhances the catalytic oxidation of CO step (r_{11}) and thus selectivity to CO_2.

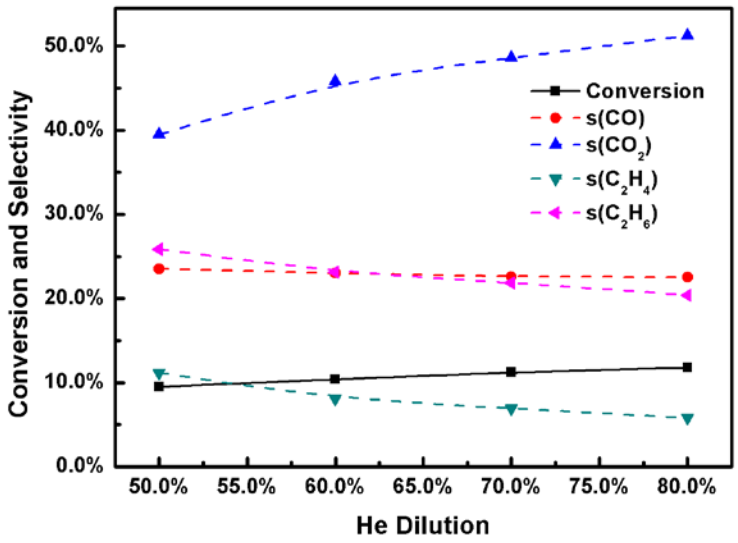

Figure 17. Conversion and selectivity to C_1 (CO, CO_2) and C_2 (C_2H_4, C_2H_6) at 738.5°C (reactor outlet temperature) while setting the inert gas (He) dilution to be 50.0%, 60.0%, 70.0% and 80.0%; Inlet feed condition: He dilution = 50%; C/O ratio = 2.0; residence time = 0.29 sec.

C/O Ratio Effect:

C/O ratio was adjusted from 1 to 4 to study the system behavior while kept inert gas dilution and residence time as constants. As shown in Figure 18, increasing C/O ratio leads to a strong decrease of CH_4 conversion from 17% to 10%. The best C/O ratio to achieve maximum C_2H_6 selectivity is at around 2.5, agrees with previous literature [47]. When C/O ratio equals to one, oxygen presents in large amount in the gas phase, leading to a large concentration of surface oxygen, which serves as the active center for CH_4 activation. As a result, r_2 is enhanced and CH_4 conversion increases. However, the large O_2 concentration in the gas phase also increases CH_3 oxidation reaction (r_3) against the coupling step (r_4), leading to a low C_2H_6 selectivity versus a high CO_2 selectivity. As C/O ratio increases, CH_4 activation step (r_2) is suppressed due to less available surface oxygen on the catalyst, and therefore CH_4 conversion decreases. Also, less available O_2 in the gas phase lowers the value of r_3/r_4 ratio, and thus slightly increases the coupling step (r_4) and C_2H_6 selectivity. As C/O ratio increase to higher values (3 and 4), no benefit was gained for C_2 yields due to much less available surface oxygen species.

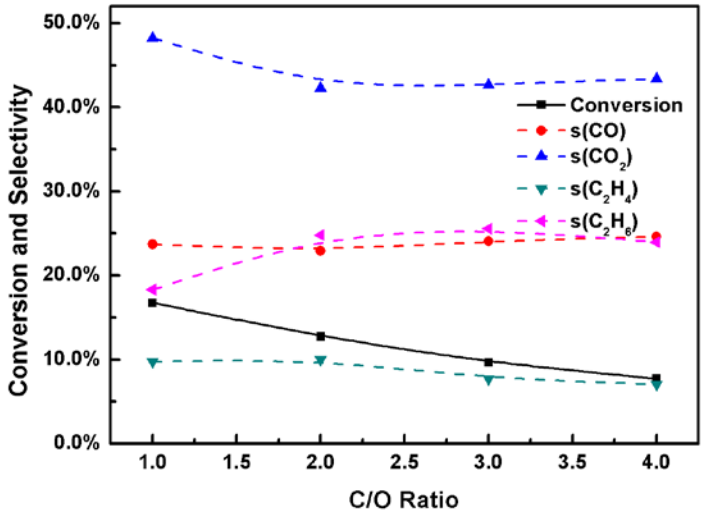

Figure 18. Conversion and selectivity to C_1 (CO, CO_2) and C_2 (C_2H_4, C_2H_6) at 738.5℃ (reactor outlet temperature) by varying C/O ratio. Inlet feed condition: He dilution = 50%; residence time = 0.29 sec.

Residence Time Effect:

Increasing the residence time will allow both gas-phase and catalytic reactions to proceed at longer time within the same reactor volume. As shown in Figure 19, such an increase leads to a dramatic increase of CH_4 conversion, a significant decrease of C_2H_6 selectivity, and enhancement of selectivity to other three products. This indicates at longer residence time, the consumption steps for the intermediate C_2H_6 become more pronounced both in gas phase (r_5), and on catalytic surface (r_6 and r_{11}). Also, the decrease of C_2H_6 also indicates the supply of CH_3 radicals is limited and thus CH_3 coupling reaction (r_4) cannot be enhanced proportionally to C_2H_6 consumption steps (r_5 and r_6).

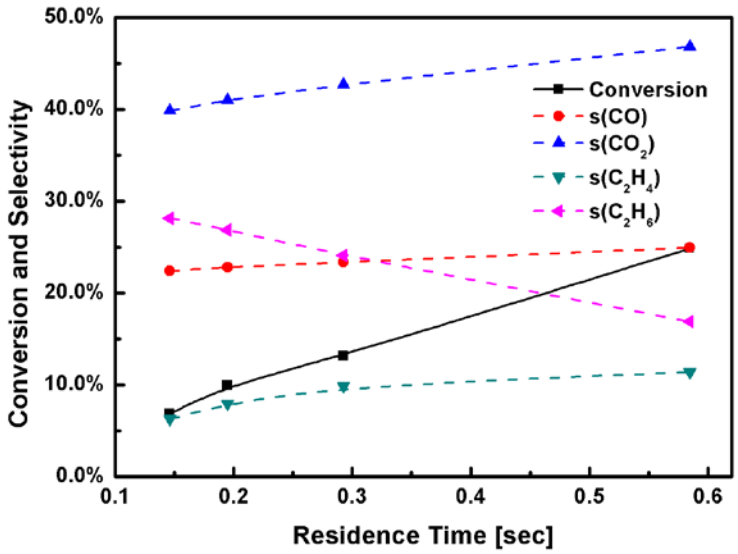

Figure 19. Conversion and selectivity to C_1 (CO, CO_2) and C_2 (C_2H_4, C_2H_6) at 738.5℃ (reactor outlet temperature) by varying the residence time). Inlet feed condition: He dilution = 50%; C/O ratio = 2.0.

4.6.4 Spatially Resolved Profiles

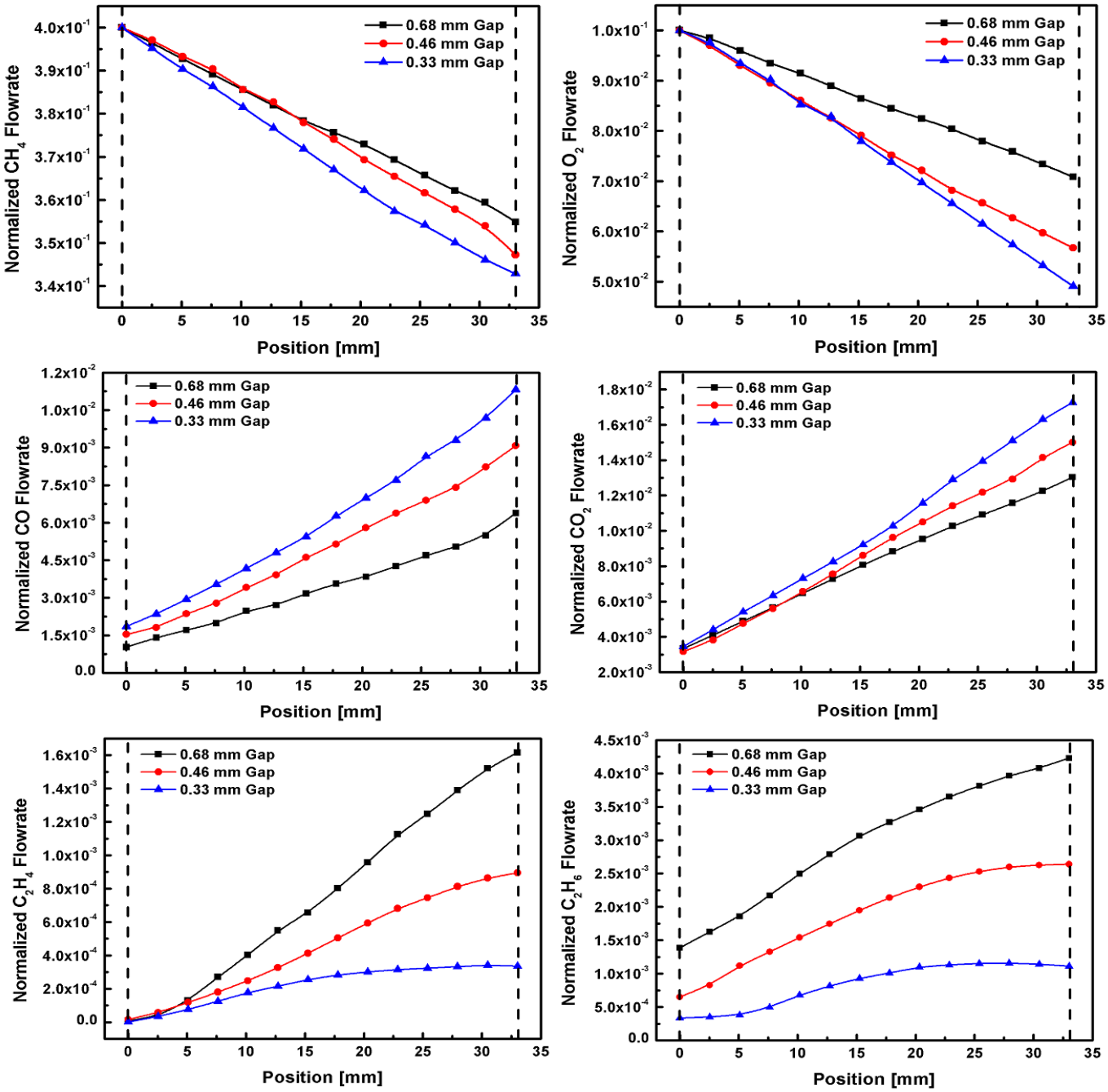

Figure 20. Spatially resolved profiles of normalized flow rates for CH_4, O_2, CO, CO_2, C_2H_4 and C_2H_6 at 738.5°C (reactor outlet temperature). Inlet feed condition: He dilution = 50%; C/O ratio = 2.0; residence time = 0.29 sec.

Figure 20 shows the spatially resolved profiles of the normalized flow rates for important species, i.e. CH_4, O_2, CO, CO_2, C_2H_4 and C_2H_6. Since the height of reaction chamber is an adjustable parameter, it is not convenient to get clear information by comparing absolute values of species flow rates. Since the residence time for all three cases was kept constant, therefore, all actual flow rates are normalized by dividing by the total inlet molar flow rate, which is proportional to the gap size. Two dash lines in spatially resolved profiles below represent the location of the inlet (left) and outlet (right) of the reaction chamber, respectively.

Normalized flow rates of reactants CH_4 and O_2, show almost a linear decrease towards the outlet. A decrease in gap size does not change CH_4 profiles much. However, it does shift O_2 flow rates to lower values towards reactor exit by increasing the magnitude of the slope. This is in accordance with previous findings that CH_4 is barely influenced by gap size, but O_2 conversion can increase at decreasing gap size because the system shifts towards C_1 formation. The almost linear decrease of CH_4 may be explained by the CH_4 activation step on catalytic surface and O_2 adsorption and desorption step:

$$CH_4 + O_{(s)} \overset{La_2O_3}{\rightleftharpoons} CH_3\bullet + OH_{(s)}$$

$$O_2 + 2* \overset{La_2O_3}{\rightleftharpoons} 2O_{(s)}$$

The O_2 adsorption and desorption step is generally very fast in OCM and can approach equilibrium. Thus, when O_2 presents in gas phase in large concentration, the concentration of surface absorbed oxygen species is not expected to change significantly. Also, under current experiment inlet condition, CH_4 concentration does not change much (10% decrease in maximum at 740 ^oC). Therefore, the rate of CH_4 activation (r_2) is expected not to change dependent on the local position in the reaction chamber.

Similarly, normalized flow rate profiles for CO and CO2 shows a monotonic increase towards the reactor exit. Decreasing the gap size leads to a shift of both curves to higher values, suggesting an increase of catalytic reaction steps r_6, r_9 and r_{11} leading to increase of C_1 products. Moreover, the increasing trend becomes more pronounced as closed to reactor exit.

Flow rate profiles for C_2 products almost keep increasing towards reactor outlet, with the exception that for the case with the smallest gap size, C_2 begins to decrease near the reactor outlet. By decreasing the gap size, flow rate profiles for both C_2H_4 and C_2H_6 shifts towards lower values, which clearly demonstrates a continuous suppressing for C_2 formation. This phenomenon agrees well with results from Figure 16.

Moreover, it is more interesting to take a step further by looking at the yield and net formation rate of C_2 species. Profiles for C_2 yields are acquired by applying Eqn. 4.1 and 4.2 at each local position for data sampling within the reaction chamber. Moreover, profiles for the net formation rate of C_2 products are derived from the following equation:

$$r_{product}\left(\frac{mol}{m^3 \cdot s}\right) = \frac{F_{x+\triangle x} - F_x}{A \cdot x} \qquad \text{(Eqn. 4.3)}$$

Where A is the cross-sectional area of the reaction chamber, F_x is the average molar flow rate at position x, and $\triangle x$ is the distance interval to acquire spatially resolved data, i.e. 2.54 mm in this experiment.

Profiles for C_2 yields show similar trend to normalized C_2 flow rates in Figure 21, since gap size has only slight effect on CH_4 conversion. Decreasing the gap size increases the C_2 dehydrogenation steps, and ultimately leads to a decrease of the yields for C_2 species. At the smallest gap size, due to the continuous suppressing of C_2 formation, the curve for C_2H_4 yield is almost flat at the exit end (~25 – 33 mm), while C_2H_6 yield achieves a maximum at ~27 mm.

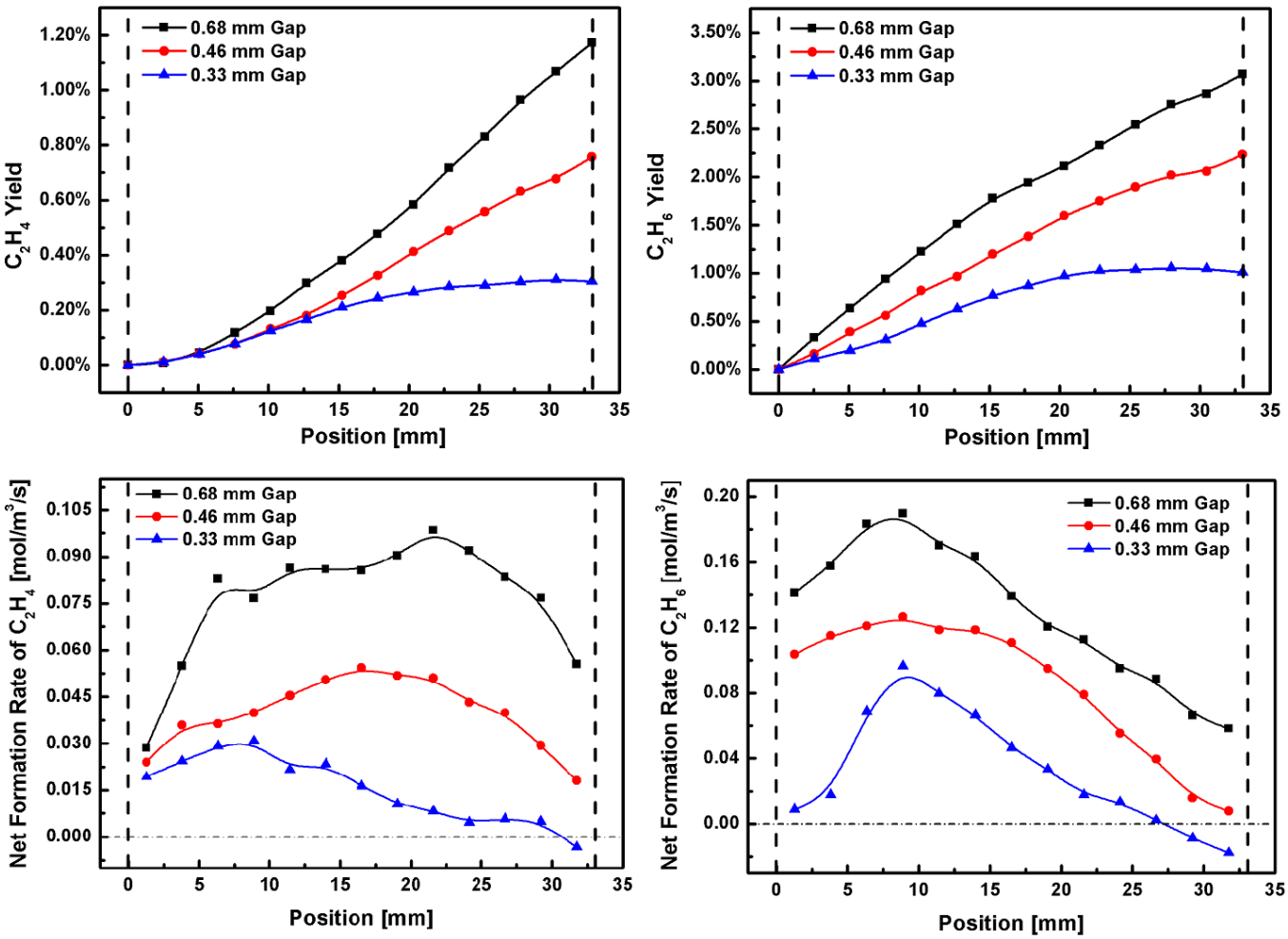

Figure 21. Spatially resolved profiles of yields and net formation rates for C_2H_4 and C_2H_6 at 738.5°C (reactor outlet temperature). Inlet feed condition: He dilution = 50%; C/O ratio = 2.0; residence time = 0.29 sec.

Additionally, more information can be gained by looking at the spatially resolved profiles of net formation rates for C_2 species. The initial uptake in curves for C_2H_6 suggests that CH_3 direct coupling (r_4) is the dominant step with respect to C_2H_6 consumption steps (r_5, r_6) near the inlet, since rates for consumption steps are limited by small amount of C_2H_6. However, as C_2H_6 is produced continuously due to its net formation, consumption steps keep increasing and become more dominant, reflected by the appearance of maximum at ~9 mm and a decreasing of reaction rate all way to reactor outlet.

In comparison, formation rate profiles of C_2H_4 have similar trends except that the peaks are broader, and the location for maximum shifts towards reactor inlet as gap size decreases. This is mainly due to the difference in the formation step for C_2H_4 (r_7) and C_2H_6 (r_4). Unlike the CH_3 coupling step (r_4) which depends on the limited CH_3 radicals, C_2H_4 formation step has more potential to increase since it is first order dependent to C_2H_6 concentration. Large gap size (680 μm) favors C_2H_6 via CH_3 coupling, thus C_2H_4 formation step keeps increasing until consumption steps (r_8, r_9) take over at ~23 mm. As gap size decreases, although C_2H_4 formation step (r_7) is enhanced due to the increasing rate of catalytic dehydrogenation steps of C_2H_6 (r_6), C_2H_4 is expected to consumed faster since C_2H_4 dehydrogenation steps both in gas phase as well as on catalytic surface are increased. Thus, the net result is that the peak value for C_2H_4 selectivity shifts towards reactor inlet. It is also interesting to see that, due to the continuous suppressing of gas-phase reaction, and the increasing reaction rates of C_2 consumption steps, the net formation rates of C_2 products become negative in the case for the smallest gap size and thus a slight decrease of C_2 flow rates is observed at reactor outlet.

4.7 CONCLUSION AND SUMMARY

In summary, OCM reaction has been tested as the model reaction in a novel microreactor system developed in our group, which is able to incorporate La_2O_3-based thin-film catalyst. Precise control of the critical dimension, as well as the acquisition of spatial resolved compositional profiles, allow us to investigate the interplay between gas-phase and catalytic chemistries for this reaction.

Results suggest decreasing the gap size barely influences CH_4 conversion, however, it does significantly shift the system towards the direction of catalytic reactions, which favors deep oxidation reaction to produce C_1 species, while suppresses gas-phase reactions from which C_2 can be generated via CH_3 coupling. This trend is further confirmed by spatially resolved profiles of C_2 flow rates and net formation rates, which shift continuously towards lower values over the entire range of reaction chamber. These results clearly reveal the complex interaction between homogeneous-heterogeneous chemistries in OCM reaction. More importantly, it demonstrates the ability to steer and control the relative contribution of gas-phase versus catalytic reactions to the overall system. Thus, it is quite promising that this methodology can be extended to investigate the coupling effect of other reaction systems where gas-phase and catalytic chemistries coexist.

5.0 NUMERICAL SIMULATION OF OCM REACTION SYSTEM

5.1 INTRODUCTION

The incorporation of detailed elementary reaction network into CFD study is a major trend nowadays not only due to the dramatic increase of the computational capability, but also that more accurate numerical models need to be formulated to provide insights into various reaction systems. This methodology finds various fields for application, such as reactor optimization [40, 63], process intensification [64, 65] and pollutant control [34, 35, 66]. The gas-phase combustion chemistries for light hydrocarbons (C_1 to C_4) have been extensively researched for decades due to their great industrial significance and therefore their mechanism are relatively mature and well understood [67, 68]. In comparison, the establishment of catalytic reaction mechanism is relatively new and only a few have been proposed and validated today, such as catalytic partial oxidation (CPO) of light alkanes on noble metals (Pt, Rh, and Pd) [69-73], due to the potential utilization of short contact reactor technology.

For the OCM reaction, there are several microkinetic models been reported from previous literatures [52, 54]. Couwenberg et al. developed a one-dimensional microkinetic model that in well agreement with experiment results [74, 75]. The model includes the effect of mass transport limitation which is caused by the very high consumption rates of radical intermediates such as methyl (CH_3) and hydroperoxy (HO_2) radicals. Su et al. developed a microkinetic model based on thermodynamic consistency [53], two key parameters have been identified and by adjusting

their values, an upper bound of 28% for C_2 yield has been predicted for CH_4/O_2 co-fed, single pass OCM process. Moreover, Sun [50] and Thybaut [27] recently proposed an OCM microkinetic model which is able to capture the performance for multiple potential catalysts by identifying and fitting several most important parameters. Such methodology, as they claimed, can combine with high throughput experimentation (HTE) to accelerate catalyst development process.

In this Chapter, a numerical model is built to study OCM reaction by applying commercial software COMSOL Multiphysics. A two-dimensional reactor model is used, which incorporates both gas-phase and catalytic reaction mechanisms. By mimicking the experiment operating conditions as close as possible, the current numerical study aims to support experimental observations described in Chapter 4.0, and provide further insights into the system behavior. Additionally, this numerical model is used to predict reaction behavior that experiment cannot achieve, such as the start-up behavior of OCM (transient) and the influence of pressure on reaction behavior.

In the following, Chapter 5.2 will describe the detailed methodology regarding to how the model built in COMSOL. The settings of the reactor geometry, inclusion of elementary reaction mechanisms, as well as the governing equations will be fully discussed. The settings of the solver and detailed computation procedure will also be explained. Next, in Chapter 5.3, simulation results at both transient and steady-state will be presented and discussed.

5.2 MODELING PROCEDURES

5.2.1 Reactor Modeling and Geometry Settings

Figure 22 shows the reactor geometry used for numerical modeling in this work. Considering the internal structure of the main microchemical reactor described in Chapter 3.2, a rectangular-shaped reaction chamber was applied. In this configuration, reactive gas mixture (CH_4/O_2/He) is fed from the bottom (gas inlet), travels through the reaction chamber and finally leaves from the top (gas outlet). The boundary on the right represents the reactive surface, mimicking the La_2O_3-based thin-film catalyst used in the experiment. To reduce the size of the model and thus the need for computation resources, only half of the reaction chamber was modeled by setting the left boundary as the symmetry plane.

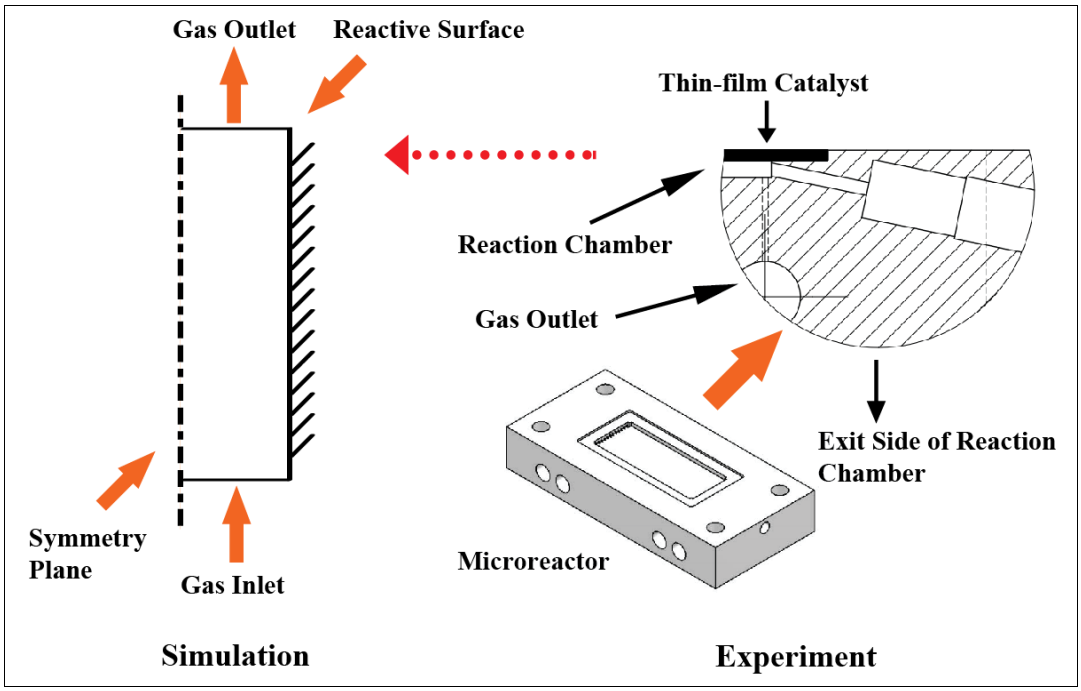

Figure 22. The schematic of the reactor geometry for modeling and its comparison with the actual experiment setup

The dimensions (length, width) of the reactor geometry for modeling were determined by the dimensions (length, height) of the actual reactor used for experiment. The total length of the actual reaction chamber is 36 mm. To save computational resources, only one sixth of the length, i.e. 6 mm was modeled. The width of the reaction chamber was modeled exactly, which is the half of the actual reaction chamber. To match the experiment, the critical dimension (height of reaction chamber) was sequentially decreased from 680 μm to 460 and 330 μm.

5.2.2 Reaction Mechanisms for OCM

In this work, the microkinetic model developed by Sun [50] and Thybaut [27] were chosen, which accounts for both gas-phase as well as catalytic chemistries for OCM process. Specifically, the gas-phase mechanism consists of 39 elementary reaction steps among 13 molecules and 10 radicals. Catalytic reaction network contains 14 elementary steps and 9 surface species.

The development of gas-phase kinetics was initiated by Chen [49] to study the OCM behavior in the absence of catalyst at atmosphere pressure condition. The effect of pressure was incorporated into the mechanism later [51] and was finally used for the coupling of gas-phase and catalyst kinetics. The detailed gas-phase reaction mechanism was quoted in the appendix, which mainly includes the following reaction steps: primary initiation (reaction 1); CH_3 radical generation (reaction 2 – 5) by hydrogen abstraction; CH_3 radical oxidation leading to CH_3O and CH_2O radicals (reaction 6 – 8); CH_3 radical coupling to C_2H_6 (reaction 9); oxidation of CH_3O and CH_2O radicals to form CO and CO_2 (reaction 11 – 16); oxidative dehydrogenation of C_2H_6 and C_2H_4 to C_2H_4 and C_2H_2, respectively (reaction 17 – 30 and 39); C_3-involved steps (reaction 31 – 34); H_2-O_2 reactions (reaction 35 – 38).

The molecules are: dihydrogen (H_2), water (H_2O), hydrogen peroxide (H_2O_2), dioxygen (O_2), methane (CH_4), methanal (CH_2O), carbon monoxide (CO), carbon dioxide (CO_2), acetylene (C_2H_2), ethylene (C_2H_4), ethane (C_2H_6), propylene (C_3H_6) and propane (C_3H_8).

The radicals are: hydrogen atom (H), atomic oxygen (O), hydroxyl (OH), hydroperoxy (HO_2), formyl (CHO), methoxy (CH_3O), methyl (CH_3), vinyl (C_2H_3), ethyl (C_2H_5), propyl (C_3H_7) radicals.

In gas-phase kinetics, Arrhenius equation was used to calculate the reaction rate constants and NASA thermodynamic database was applied to calculate the equilibrium coefficient. All mathematical implementation can be found in detail in the appendix.

The catalytic reaction network consists of 14 elementary reactions steps and was developed for general OCM catalyst. Several important characteristics are covered in the mechanism, such as oxygen activation, generation of radicals, non-selective deep oxidation on catalyst surface, radical quenching and CO_2 inhibition effect. The mechanism includes the CH_4 activation on the catalytic surface by the dissociation of O_2 (reaction 40); activation of CH_4 by breaking C-H bond assisted by absorbed oxygen species, producing CH_3 radicals in the gas phase (reaction 41); hydrogen abstraction of C_2H_4 and C_2H_6 (reaction 42, 43); regeneration of active sites by the formation and desorption of H_2O (reaction 44, 45); CH_3 and HO_2 radical quenching effect (reaction 46, 53); deep oxidation of CH_3O(s) leads to formation of CO and CO_2 (reaction 47 – 50); adsorption and desorption steps of CO and CO_2 (reaction 51, 52).

Since the proposed microkinetics was developed for OCM process using La–Sr/CaO as the catalyst, it has been tested that a direct application based on all original parameters could not capture correctly the system behavior for OCM experiment described in Chapter 4.0. However, since elementary reaction steps for OCM are quite similar for different catalysts, the

microkinetics is believed to be corrected by slight modifications of several parameters. It has been tested that two parameters need to be adjusted: 1) reaction enthalpy of hydrogen abstraction of CH_4 was changed to 40.0 kJ/mol (original: 61.4 kJ/mol); initial sticking probability of CO was adjusted to 8.0×10^{-4} (original: 2.7×10^{-4}). These modifications are believed to enhance the hydrogen abstraction steps of CH_4, C_2H_4 and C_2H_6 (steps 41, 42 and 43), as well as the CO adsorption step on surface (step 51). Additionally, the enhanced rate of reaction 42 can lead to more C_2H_3 radials pumped into the gaseous phase, resulting in a significant increase of C_2H_2 concentration (step 28). However, the applied gas-phase mechanism does not have relevant steps to capture the oxidation of C_2H_2 to C_1 products. This deficiency can lead to an overestimation of C_2H_2, which was not observed during OCM experiment in Chapter 4.0. Therefore, to remedy this issue, step 28 was omitted in the simulation.

5.2.3 Numerical Model

The finite element method (FEM) was applied to discretize the 2D continuity, momentum and species conservation equations in the fluid. The reactor modeling was implemented by using COMSOL Multiphysics and three interfaces have been used: 1) COMSOL Multiphysics Main Interface; 2) The Transport of Diluted Species Interface; 3) The Laminar Flow Interface.

While COMSOL Main Interface provides a general GUI platform for FEM-based modeling, one of its important features – the Weak Form (boundary mode) – has been applied into the model to incorporate partial differential equations (PDEs) on the right boundary, the one acting as the reactive surface on which surface chemistry occurs. Thus, the gas-phase domain and the catalytic surface are coupled together by providing flux values of relevant gas-phase

species. The detailed method for the weak form implementation is discussed in COMSOL instruction manuals [76].

In formulating the governing equations for mass transport, even though physics for mixture-averaged diffusion model and Maxwell-Stefan multicomponent transport may capture the system behavior with better accuracy, current model is built based on the physics for diluted species transport [77, 78]. In the model, Fickian binary diffusivities were used and diffusion coefficients for all gas-phase chemical species were calculated by taking inert gas helium (He) as the reference, which was used as the dilution component in the experiment. Additionally, the full Navier-Stokes equation was coupled with equation of continuity to capture flow behavior, which belongs to a weakly compressible single-phase laminar flow (Re < 1) in the current microchemical reactor system.

Also, the energy field has been excluded from current simulation. Instead, the computation domain is set at a specified temperature. Such treatment of energy field is because of the configuration of actual experimental setup. As discussed in Chapter 4.0, a major advantage of current reactor is the ability to create a quasi-isothermal condition, which has been demonstrated experimentally in OCM study that the temperature only changes slightly and is independent of operating conditions. Such simplification was found to reduce the computation efforts greatly without loss of accuracy in terms of capturing system behavior.

5.2.4 Detailed Computational Procedure

Mesh Configuration:

Prior to computation, a mesh was created to discretize the computation domain by free triangulation method [42]. The mesh qualify was controlled by setting the maximum element

size of relevant domain, boundaries and points in the geometry. Figure 23 provides a typical mesh configuration for this model. The main subdomain (gas phase) applied relative large triangular elements, with the maximum element size set to 20 μm. The maximum element sizes were further tightened down for areas near the four corners of the reaction chamber (3 μm), inlet (5 μm) and reactive surface (8 μm), where the stiffness might occur. For example, the coupling between gas-phase and catalytic chemistries on the reactive surface could lead to large gradients of species concentrations. The configuration of the mesh was further verified by comparing the numerical results of important parameters before and after the mesh refinement, such as concentration of CH_3, HO_2, and C_2H_6. No apparent improvement was observed (maximum relative deviation less than 0.1%). Thus, the mesh configuration was proved to be sufficient for the OCM study. For the case with 0.68 mm gap size, the number of elements is 28169 and the degree of freedom (DOF) is 409,817.

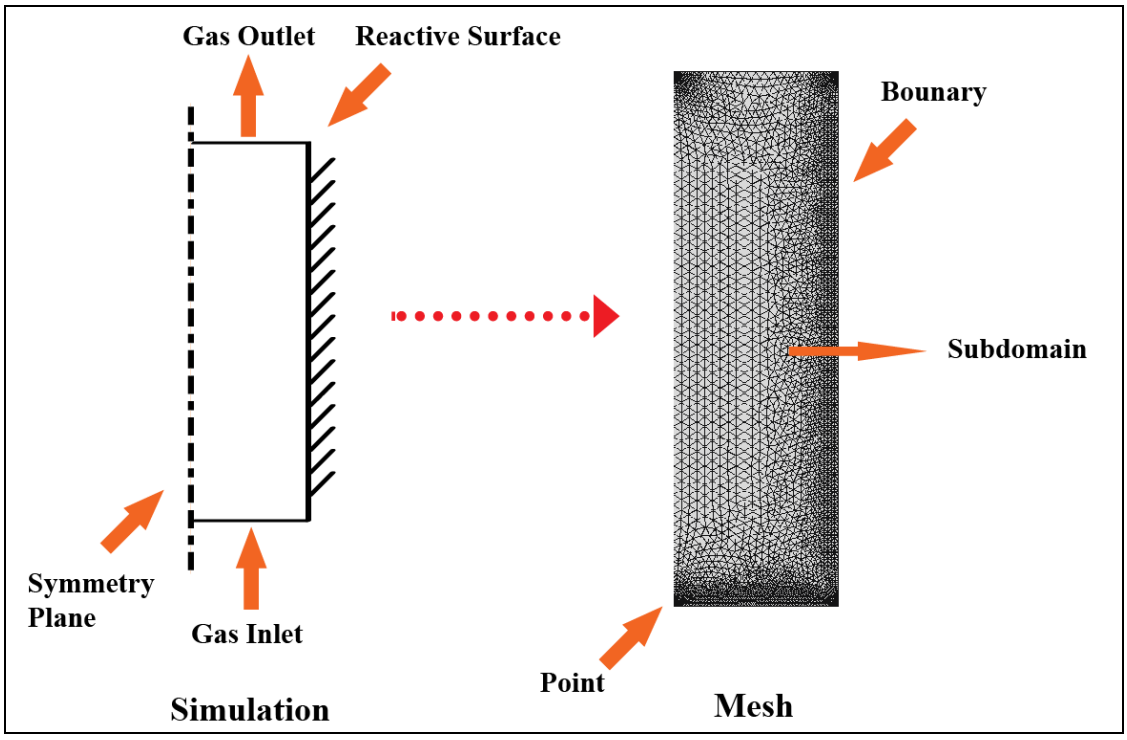

Figure 23. A typical mesh configuration for 2D numerical modeling of OCM reaction.

Model Configuration:

For OCM study, both transient and state-steady models were computed. The transient model is mainly used to capture the startup behavior of OCM reaction in the micro-scaled reaction chamber. Therefore, at time zero, the reaction chamber was assumed to be filled with pure helium. A flat flow condition was applied at the inlet boundary, which was calculated from residence time (RT) used in experiment. The $CH_4/O_2/He$ reactive mixture with proper compositions was also applied at inlet boundary for mass transport physics. The total computation time was set to 1 RT based on the corresponding operating conditions.

Moreover, results for steady-state model were acquired by using the result at the last time point from transient model as the initial guess, which was generally demonstrated to be a good initial guess that led to decent convergence of the solver. The steady-state solution was used to capture the final state of OCM behavior, based on which reaction pathways analysis was performed.

Solver Settings:

The PARDISO Direct Solver was applied to solve the OCM model. PARDISO solver is a high-performance, robust, and memory efficient software for solving large sparse symmetric and unsymmetrical linear systems of equations [79, 80]. In this model, dependent variables have widely different magnitudes, e.g. the variable pressure (p) is on the magnitude of 10^5 while concentration (mol/m^3) of H radical is of 10^{-7}. This might lead to ill-conditioned matrix after the assembly of the discretized PDEs. Therefore, to remedy this situation, manual scaling was used and all dependent variables were given a value with proper order of magnitude, based on

previous numerical studies reported for OCM. The original variable which was divided by the scaling parameter (same unit) has resulted in a scaled variable. 10^{-4} and 10^{-3} were specified as the absolute and relative tolerances, respectively, for all scaled variables. Specifically, the absolute and relative tolerances were applied by the following equation to control the error in each iteration step:

$$\left(\frac{1}{N}\sum_i\left(\frac{|E_i|}{A_i + R|U_i|}\right)^2\right)^{1/2} < 1 \qquad \text{(Eqn. 5.1)}$$

where A_i denotes the absolute tolerance for DOF i; R is the relative tolerance, and N is the number of degrees of freedom; U is the solution vector corresponding to the solution at a certain time step; E denotes the solver's estimate of the (local) error in U committed during this time step.

These tolerance values were found to result in a sufficiently accurate computation, since no apparent improvement was observed as tolerance values tighten down to 10^{-5} and 10^{-4}, respectively. Reaction pathway analysis was performed for steady-state solution of OCM. Major species have been identified and corresponding formation/consumption rates were calculated by integration on the relevant geometric entity. Specifically, for gas-phase species, formation/consumption rates are acquired by performing integration over reaction chamber (gas-phase reaction pathways), as well as over the reactive surface (catalytic reaction pathways). For surface species, integration only needs to be performed on the catalytic surface.

All numerical models were implemented in COMSOL Multiphysics (version 4.2a) and computed on a Dell Studio XPS 435^T workstation. The workstation is equipped with Intel Core i7 processors and 24 GB of memory. Typically 12 to 48 hours are required to solve a transient model. For the steady-state model, the computation time required is usually between 1 to 6 hours,

depending on the quality of the initial guess. For both transient and steady-state models, the ranges of computation time are acceptable for this work and agree with similar type numerical models reported by other groups [50, 53]. OCM models were also computed on Pople cluster in Pittsburgh Computing Center. Pople is an SGI Altix 4700 shared-memory NUMA system which has 192 blades. Each blade is equipped with 2 Itanium2 Montvale 9130M dual-core processors. Steady-state models were computed by using two blades (8 cores in total) and the computation time was compared with the one from Dell workstation just mentioned. It has been found out that it usually took around 8 to 12 hours to achieve a steady-state solution. The much longer computation time for solving the model on Pople is probably due to the inefficiency of the parallel algorithm applied to solve such type of problem. Therefore, all the models were computed using the Dell workstation.

5.3 RESULTS AND DISCUSSION

5.3.1 Characteristics of OCM system

To begin with, several important dimensionless numbers were calculated to capture the general characteristics of this system. The following operating conditions are used as the reference case:

1) Temperature: 740 ^{o}C;
2) Gap size: 680 μm;
3) Inlet gas composition: 40% CH_4 + 10% O_2 + 50% He;
4) Residence time: 0.29 sec.

The corresponding linear velocity in the reaction chamber is 0.13 m/s, thus the Mach number is calculated as

$$Ma = \frac{v}{a} = \frac{0.13}{340.3} = 3.8 \times 10^{-4} \qquad \text{(Eqn. 5.2)}$$

where Ma denotes Mach number; v (m/s) represents the averaged linear velocity with the reaction chamber; a is the speed of sound.

Since the Mach number for this model is close to zero, it can be claimed that the fluid has an incompressible characteristic. The actual implementation for the model applies a weakly compressible Navier-Stokes equation and it holds under conditions when the Mach number is less than 0.3.

Moreover, when the averaged linear velocity is held at 0.13 m/s, and approximate fluid density and viscosity of the reactive mixture by pure He for simplicity, the Reynolds number can be calculated as

$$R_e = \frac{\rho v d}{\mu} = \frac{0.4537 \times 0.13 \times 680 \times 10^{-6}}{5.83 \times 10^{-5}} = 0.688 \qquad \text{(Eqn. 5.3)}$$

where R_e denotes the dimensionless Reynolds number; ρ (kg/m^3) is the density of the reactive mixture; d (m) represents the critical dimension, i.e. the height of reaction chamber; μ (Pa·s) is the dynamic viscosity of the fluid. The small value of the Reynolds number confirms the laminar type of fluid in this system.

The Damkohler number was calculated to capture the chemical reaction timescale with respect to transport phenomena in the system. Since both gas-phase and catalytic reactions occurred for OCM system, two Damkohler numbers are applied which are defined by the following equation:

$$Da_{gas} = \frac{gas-phase\ \ reaction\ \ rate}{total\ \ transport\ \ rate} = \frac{\int r_{gas} dA}{\int_{outlet} F_{tot} ds} \quad \text{(Eqn. 5.4)}$$

$$Da_{cat} = \frac{catalytic\ \ reaction\ \ rate}{total\ \ transport\ \ rate} = \frac{\int_{cat\_surf} r_{cat} ds}{\int_{outlet} F_{tot} ds} \quad \text{(Eqn. 5.5)}$$

where Da_{gas} and Da_{cat} represent Damkohler number due to gas-phase and catalytic reactions, respectively; r_{gas} (mol/m^3/s) and r_{cat} (mol/m^2/s) denote the overall reaction rates for a certain species due to gas-phase and catalytic reactions, respectively; F_{tot} (mol/m^2/s) represents the total flux rate due to diffusion and convection.

As can be seen in Eqn. 5.4 and 5.5, the total gas-phase reaction rate is derived by integrating the rate for a certain species overall the 2D domain. Similarly, total reaction rate due to catalytic reactions is acquired by integrating the rate over the entire reactive surface. Moreover, transport rate can be approximated by integrating the total mass flux at the reactor outlet for simplicity. All the rates are then multiplied by an identical width of reaction chamber (unit: m) and convert to the final value with the unit of mol/s.

One of the reactants (CH_4) and products (C_2H_6) were selected to calculate the Damkohler numbers to represent OCM system. For the reactant CH_4, the values for Da_{gas} and Da_{cat} are calculated to be 9.25×10^{-3} and 8.20×10^{-2}, respectively. They are relatively small due to the large convective flux of CH_4 as a reactant. On the contrary, values for Da_{gas} and Da_{cat} are 5.08 and 4.10, which indicates that the system is very sensitive to both gas-phase and catalytic chemistries.

5.3.2 Transient Behavior of OCM

To demonstrate the startup behavior of OCM in the micro-scaled reaction chamber, 2D transient profiles of three important species have been selected and presented in Figure 24, 25 and 26. Three species chosen belong to one the most important radicals in OCM system (CH_3), and a typical C_1 (CO_2) and C_2 (C_2H_6) products. The time range chosen to be presented in these figures is from 0.005 sec to 0.05 sec, which is ~1/6 of the total RT at current operating conditions. Transient results at longer time are not shown, since the orders of magnitude for species concentrations vary too dramatic and is not convenient for presentation.

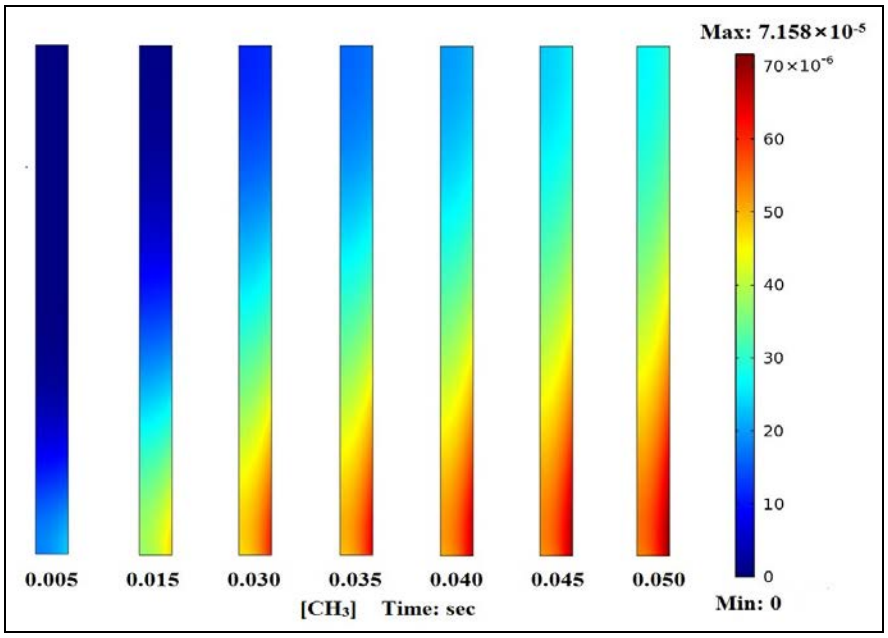

Figure 24. Snapshots of CH_3 radical concentration (mol/m^3) profiles to simulate the startup behavior of OCM reaction at 740^{o}C (gap size = 680 μm). Inlet feed condition: He dilution = 50%; C/O ratio = 2.0; residence time = 0.29 sec.

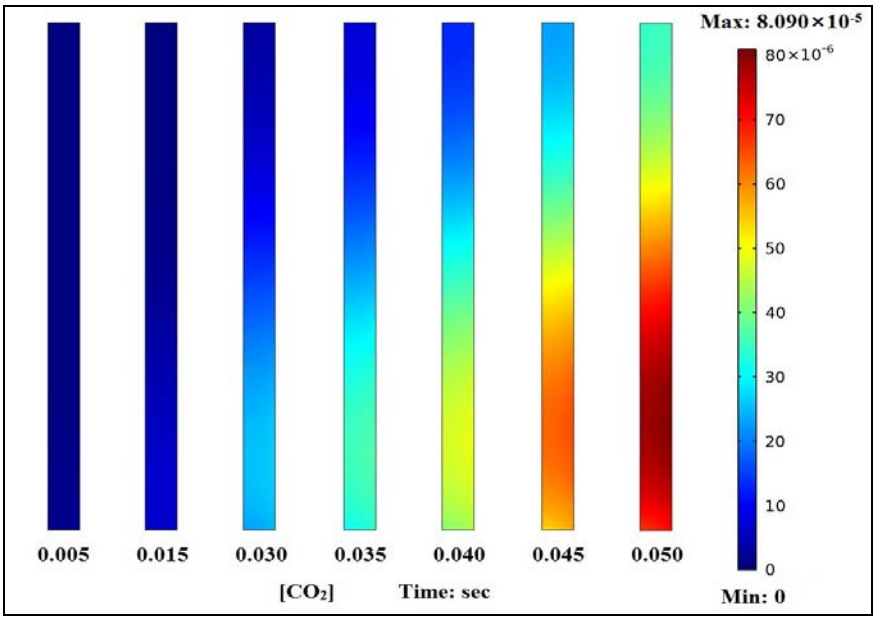

Figure 25. Snapshots of CO_2 concentration (mol/m^3) profiles to simulate the startup behavior of OCM reaction at 740^{o}C (gap size = 680 µm). Inlet feed condition: He dilution = 50%; C/O ratio = 2.0; residence time = 0.29 sec.

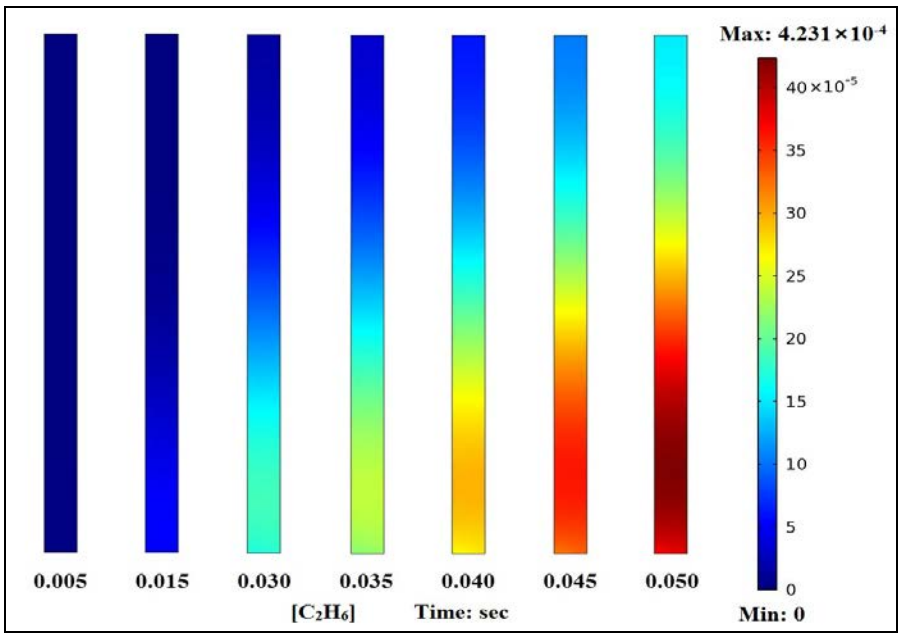

Figure 26. Snapshots of C_2H_6 concentration (mol/m^3) profiles to simulate the startup behavior of OCM reaction at 740^{o}C (gap size = 680 µm). Inlet feed condition: He dilution = 50%; C/O ratio = 2.0; residence time = 0.29 sec.

It can be seen that OCM is initiated in the vicinity of the reactive surface at reactor entrance, leading to a large local concentration of CH_3, which is then quickly propagated to surrounding areas by both diffusion and convection. This is in well agreement with the proposed reaction network shown in Figure 12, which suggests that OCM is initiated by CH_4 activation on catalyst surface (major route, r_2), resulting in the formation of CH_3 radicals. Also, transient concentration profiles show that CH_3 radicals form a boundary layer near the catalytic surface and travel up towards reactor outlet. The form of boundary layer is mainly due to fast generation (r_1, r_2) and consumption steps (r_3, r_4) for CH_3 radicals.

In comparison, CO_2 and C_2H_6 concentration profiles do not show a large gradient. CO_2 concentration decreases slightly from the reactive surface towards the gaseous phase, in accordance with the fact that CO_2 is mainly formed catalytically. C_2H_6 concentration profiles are almost flat and independent of the x-axis position, since it is exclusively formed by fast CH_3 coupling step (r_4) in the gas phase. Also, although the maximum concentrations of CO_2 and C_2H_6 are initially achieved at reactor inlet, the maximum locations are not stationary which travel towards reactor exit as time elapses. This effect is due to the net formation rates of both species and fast mass diffusive and convective transport in axial direction.

Another interesting effect to see from these transient profiles is that, although only ~1/6 of total RT of OCM process has been presented, decent concentrations for all three species are achieved at 3 mm (y-axis position), i.e. ~1/2 of the reactor length. This indicates diffusion plays an important role in mass transport, which can be confirmed by calculating the Peclet number of this system. When the height of reaction chamber is 680 μm, the velocity is ~0.124 m/s (RT = 0.29sec) and diffusion coefficient is in order of magnitude of 10^{-4} (m^2/s) at 740 ^oC, the Peclet number can be calculated as:

$$Pe = \frac{uL}{D_A} = \frac{0.124 \times 680 \times 10^{-6}}{10^{-4}} = 0.84$$

This value of Peclet number means that the diffusive flux is comparable to convective one under current experiment conditions. This also confirms the necessity to solve the full Navier-Stokes equation, rather than applying the simple plug-flow or boundary layer model.

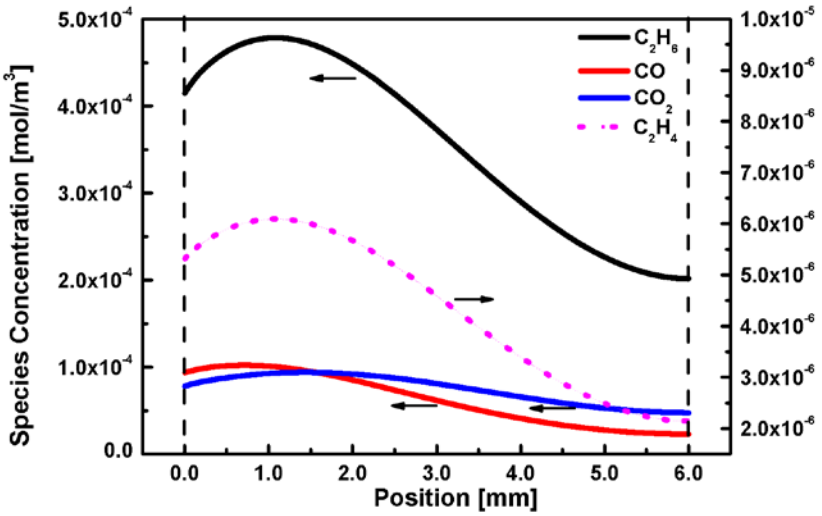

Figure 27. Concentration (mol/m^3) profiles for C_1 (CO, CO_2) and C_2 (C_2H_4, C_2H_6) products at 0.05 sec at the centerline of reaction chamber at 740 ^oC (chamber gap size = 680 μm). Inlet feed condition: He dilution = 50%; C/O ratio = 2.0; residence time = 0.29 sec.

Lastly, Figure 27 shows the 1D concentration profiles of C_1 (CO, CO_2) and C_2 (C_2H_4, C_2H_6) products at the centerline of reaction chamber at 0.05 sec. Among these profiles, C_2H_6 has the largest concentration compared to other products, which confirms that C_2H_6 is the primary product. In comparison, C_2H_4 concentration is two orders of magnitude smaller than C_2H_6, although the shapes of two profiles are quite similar. Concentrations for CO and CO_2 are in same order of magnitude. It is interesting to see than even though CO_2 is the secondary product

originated almost exclusively from CO oxidation, the location of maximum for CO_2 is ahead of CO towards reactor outlet. This can be explained by the strong diffusion effect in the axial direction as well as the relatively fast CO oxidation on the catalytic surface.

5.3.3 Steady-state Results and Reaction Pathways Analysis

Figure 28 and 29 show concentration profiles of important molecules and radicals in OCM system at steady-state conditions. The case with 680 μm in gap size was modeled, with all operating parameters settings identical to the actual experiment described in Chapter 4.0.

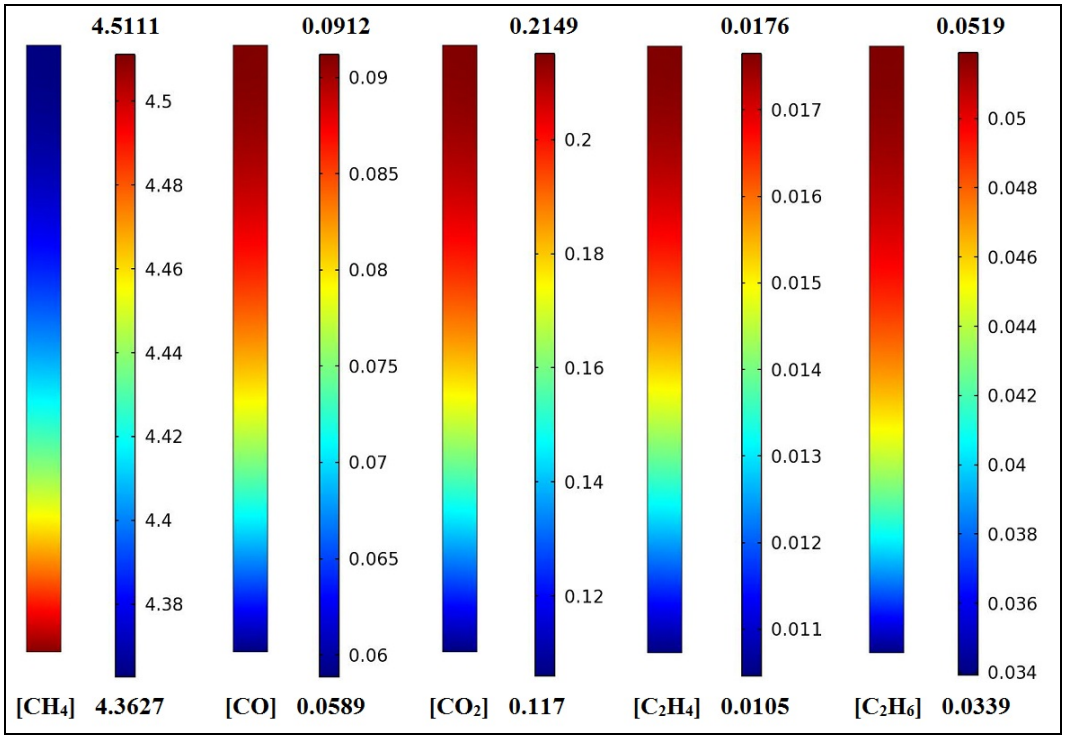

Figure 28. Concentration profiles for CH_4 and C_1 (CO, CO_2), C_2 (C_2H_4, C_2H_6) products for OCM reaction at the steady-state condition (Temperature = 740 ^oC, gap size = 680 μm). Inlet feed condition: He dilution = 50%; C/O ratio = 2.0; residence time = 0.29 sec.

As moving towards reactor exit, Figure 29 suggests the following trends: 1) a monotonic decrease for CH_4 concentration; 2) a monotonic increase for all C_1 and C_2 products; 3) no dramatic gradient is observed for all species in the x-axis direction.

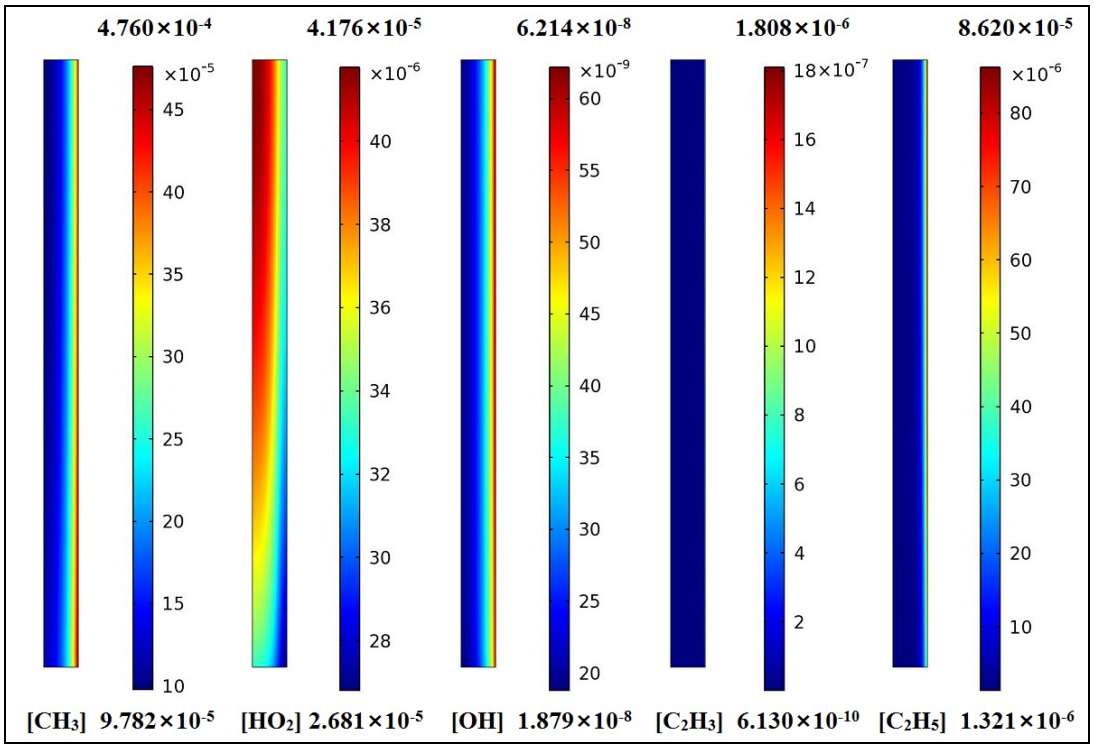

Figure 29. Concentration profiles of important radicals for OCM reaction at the steady-state condition (Temperature = 740 ^{o}C, gap size = 680 μm). Inlet feed condition: He dilution = 50%; C/O ratio = 2.0; residence time = 0.29 sec.

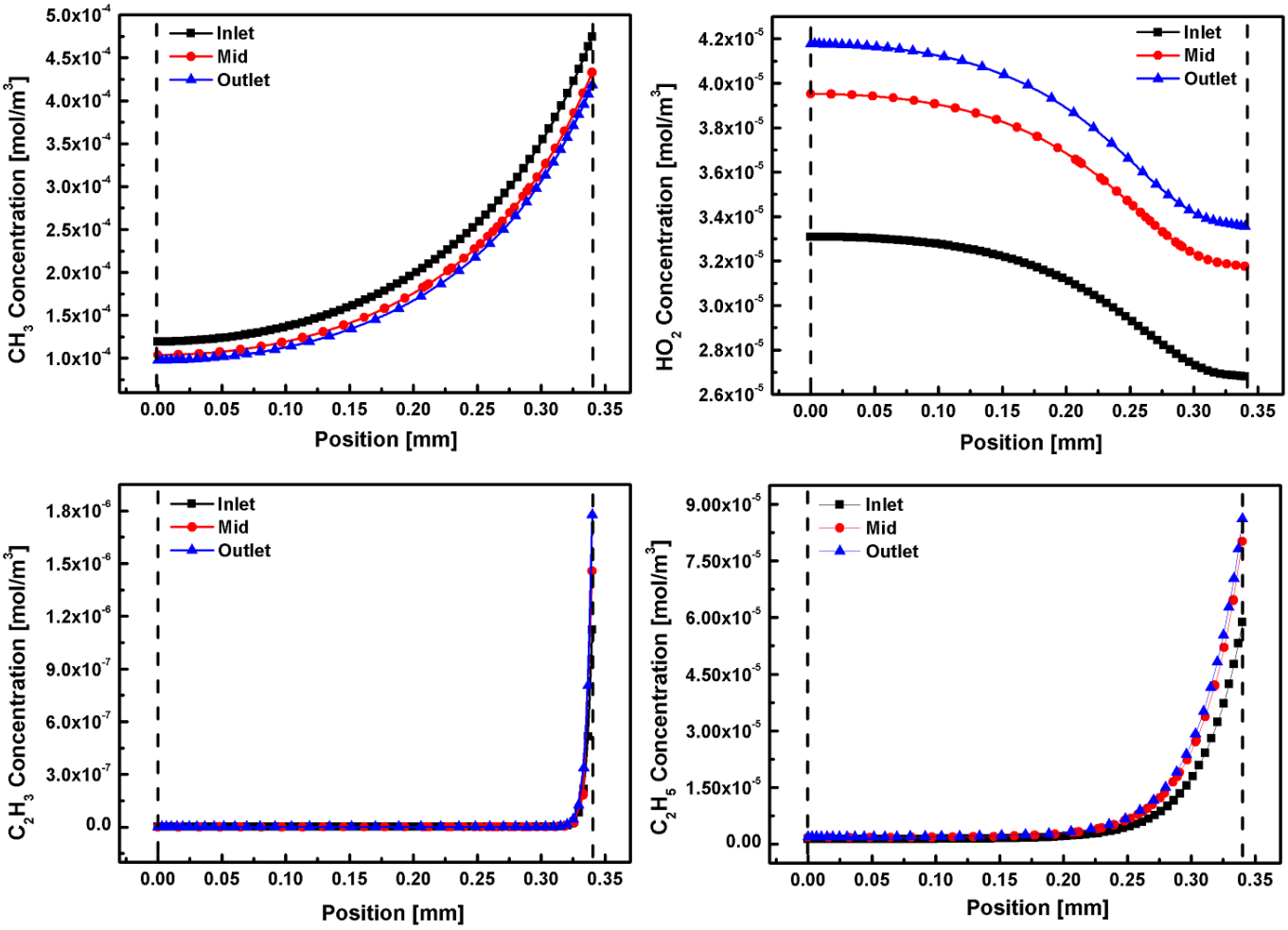

Figure 30. Radial concentration (mol/m^3) profiles for important radicals (CH_3, HO_2, C_2H_3 and C_2H_5) at the inlet, middle and outlet of reaction chamber at 740 ^oC (chamber gap size = 680 μm). Inlet feed condition: He dilution = 50%; C/O ratio = 2.0; residence time = 0.29 sec.

It is more interesting to see the 2D concentration profiles for important radicals as Figure 29 presented. To get a clearer picture, 1D profiles for CH_3, HO_2, C_2H_3 and C_2H_5 in the radical direction at the inlet, middle and outlet of the reaction chamber are also acquired (Figure 30). A general trend can be seen is that concentration gradient exists in horizontal direction for all radicals presented, though in quite different ways. CH_3 radical forms a boundary layer at reactive surface, which is mainly due to fast catalytic CH_4 activation (r_2) and consumption steps (r_3, r_4).

Its concentration reaches 10^{-4} in order of magnitude, which agrees well with previous literature [75]. OH radical also forms a thin boundary layer at the reactive surface with much smaller concentration compared to CH_3 radicals (10^{-7} vs. 10^{-4} mol/m^3). Moreover, C_2H_3 and C_2H_5 radicals also form in relatively large concentration (10^{-6} and 10^{-5} mol/m^3) close to catalytic surface. Interestingly, much thinner boundary layers are formed compared to CH_3 concentration profile. These results can be explained by that La_2O_3-based catalyst can act as an excellent free radical generator in OCM process, on which C_2H_3 and C_2H_5 radicals are mainly formed via the two Eley-Rideal type reaction steps:

$$C_2H_4 + O_{(s)} \xrightleftharpoons{La_2O_3} C_2H_3\bullet + OH_{(s)}$$

$$C_2H_6 + O_{(s)} \xrightleftharpoons{La_2O_3} C_2H_5\bullet + OH_{(s)}$$

The very thin boundary layer indicates that C_2H_3 and C_2H_5 radicals are highly reactive and can be instantaneously decomposed before being transported to surrounding areas.

Another very interesting effect can be seen via the concentration profile for HO_2 radical, which shows completely different behavior compared to profiles presented for other four radical species. Two effects are observed for HO_2 radical concentration profile: 1) the largest concentration of HO_2 radical is present at the centerline of reaction chamber and decreases gradually towards the catalytic surface; 2) HO_2 concentration profile gradually evolves towards the catalytic surface as the reactive mixture approaches reactor outlet. By analyzing the reaction rates for relevant elementary steps, HO_2 is confirmed to be formed mainly at the area closed to the centerline. On the contrary, more HO_2 can be consumed by reacting with highly reactive radicals such as CH_3 and C_2H_5 close to catalytic surface, where thin boundary layers for are formed. This has resulted in a net consumption of HO_2 at the area closed to surface. However, the overall behavior for the system is forming HO_2 radicals at a slow rate. Thus, a net

accumulation of HO_2 radical leads to a gradual evolvement towards the reactive surface as fluid passes through the reactor.

Reaction Pathway Analysis

For a certain species, the analysis was performed by firstly identifying the formation and consumption steps for both gas-phase and catalytic reaction steps. Then the averaged rates were acquired by integrating the local rates at corresponding geometrical domains. By dividing the consumption rate (gas-phase/catalytic chemistry) by the total formation rate of a species, the relative importance of gas-phase/catalytic chemistry can be quantified.

As shown in Figure 31 for the reaction pathways analysis for the OCM system, the number in the parenthesis denotes the percentage of a certain species being consumed via this reaction channel (100 as basis). Thus, we can see that ~10% of CH_4 is converted, among which 90% is consumed on the catalytic surface; more CH_3 radicals are consumed by direct oxidation than the coupling reaction (r_3/r_4 = 56:32); around 65% and 58% of C_2H_6 and C_2H_4 have been consumed on the catalytic surface, respectively; CO is formed by either direction oxidation of CH_3 radicals, or the oxidation of C_2H_3 radicals originated from C_2 decomposition on the catalytic surface; CO_2 is formed almost exclusively from catalytic surface.

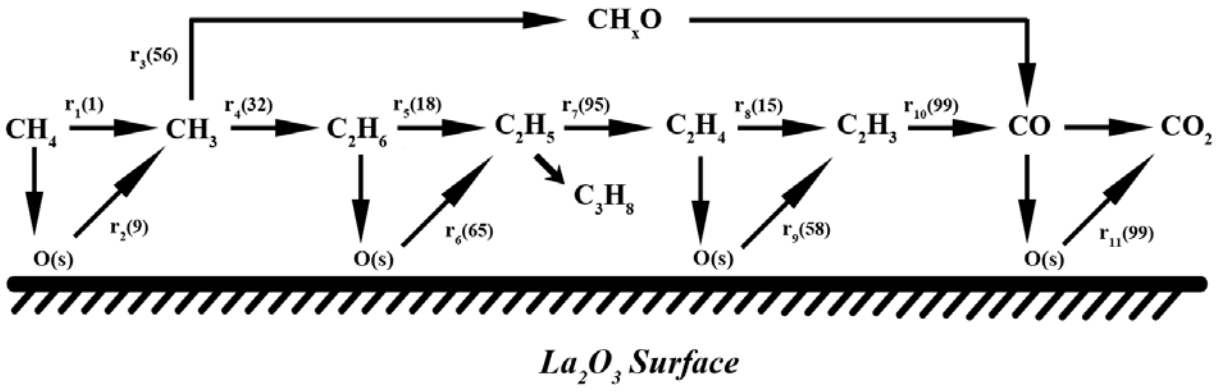

Figure 31. Reaction pathway analysis for OCM reaction at the steady-state condition (Temperature = 740 ^{o}C, gap size = 680 μm). Inlet feed condition: He dilution = 50%; C/O ratio = 2.0; residence time = 0.29 sec.

Conversion and Selectivity Data

To verify the correctness of the numerical model due to temperature change, steady-state simulations were performed at 630, 740 and 800 ^{o}C under three gap distances (680, 460 and 330 μm) and compared with experiment data. As shown in Figure 32 and 33, the numerical results are in well agreement with experiment data.

Numerical results confirm that CH_4 conversion is not influenced much by the gap size effect. However, decreasing the gap size can lead to a higher conversion O_2. Reaction pathway analysis suggests that (gap size: 680 μm), ~85% of the converted O_2 is consumed in the gas phase at 740 ^{o}C mainly by reacting with radicals (H, CH_3, C_2H_3 and C_2H_5). Decreasing the gap size favors the formation of CH_3, C_2H_3 and C_2H_5 radicals, and more O_2 are needed for the oxidation of these radical species via the following reaction pathways:

$$CH_3\bullet + O_2 \xrightleftharpoons{gas-phase} CH_2O + OH\bullet$$

$$C_2H_5\bullet + O_2 \xrightleftharpoons{gas-phase} C_2H_4 + HO_2\bullet$$

$$C_2H_3\bullet + O_2 \xrightleftharpoons{gas-phase} CH_2O + CHO$$

Also, enhanced surface chemistry can lead to a faster consumption of surface oxygen species, which is generally in equilibrium with gaseous O_2 due to the fast adsorption and desorption steps (step 40).

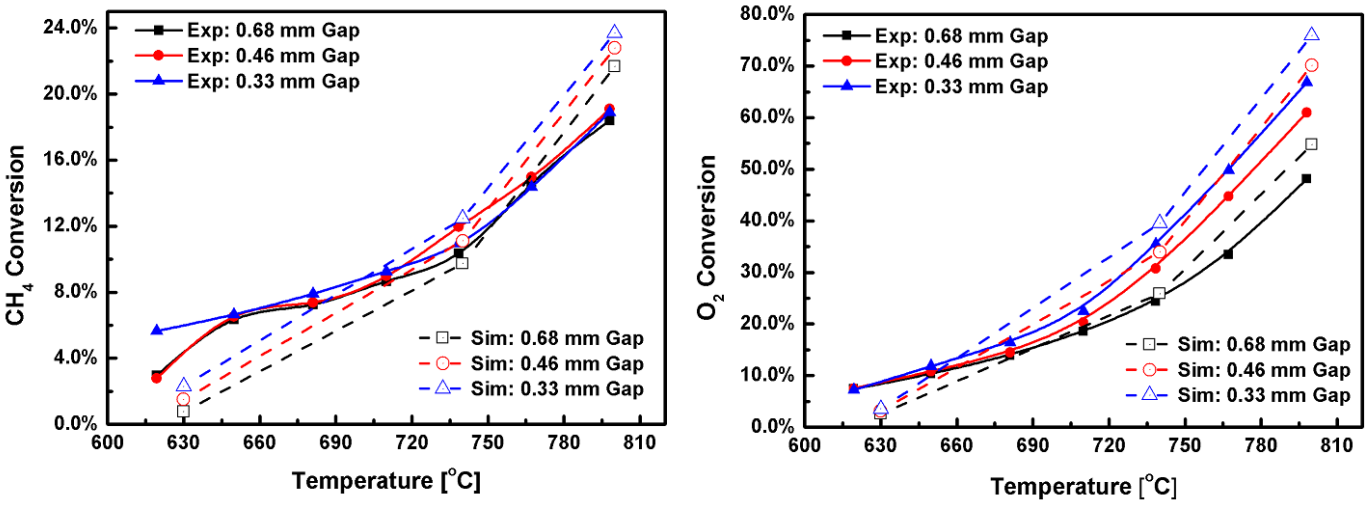

Figure 32. Comparison between simulation and experiment results for CH_4 (left) and O_2 (right) conversions at elevated temperature for OCM. Three curves represent different cases by varying the critical dimension (i.e. gap distance) of the reaction chamber. Inlet feed condition: He dilution = 50%; C/O ratio = 2.0; residence time = 0.29 sec.

Moreover, selectivity curves for C_1 and C_2 also show good agreement with experiment data. Selectivity to C_1 generally decreases with increasing temperature. This can be seen by comparing r_3/r_4 ratio, which is 65:21, 56:31 and 59:33 for 630 ^oC, 740 ^oC and 800 ^oC, respectively. The ratio shows an initial decrease from 630 ^oC to 740 ^oC, which is because r_4 has a second order dependence on CH_3 radicals mainly formed catalytically. In comparison, r_3 increases slower in response to temperature increases and only has a first order dependence on CH_3 concentration. This increasing trend of r_4 against r_3 is believed to be sufficient to explain the increasing selectivity to C_2H_4 and C_2H_6 at this temperature range.

However, from 740 ^{o}C to 800 ^{o}C, r_3/r_4 ratio does not change much. This is because the temperature is sufficiently high that the increasing rates of r_3 and r_4 due to temperature are comparable. Additionally, high temperature also enhances the dehydrogenation steps that can lower C_2H_6 selectivity, and accompanied by an increase of selectivity to C_2H_4. Another issue is the decreasing trend of CO_2 selectivity towards higher temperature. This can be explained by the "inhibition effect" for CO_2 which can have a strong interaction with different OCM catalysts by direct adsorption [81]. In fact, during the simulation, the coverage of surface-absorbed CO_2 indeed increases from ~0.0014 to 0.008 and 0.01 at 630 ^{o}C, 740 ^{o}C and 800 ^{o}C, respectively. This increasing coverage can lower the rate for CO_2 formation via catalytic oxidation of surface-absorbed CO.

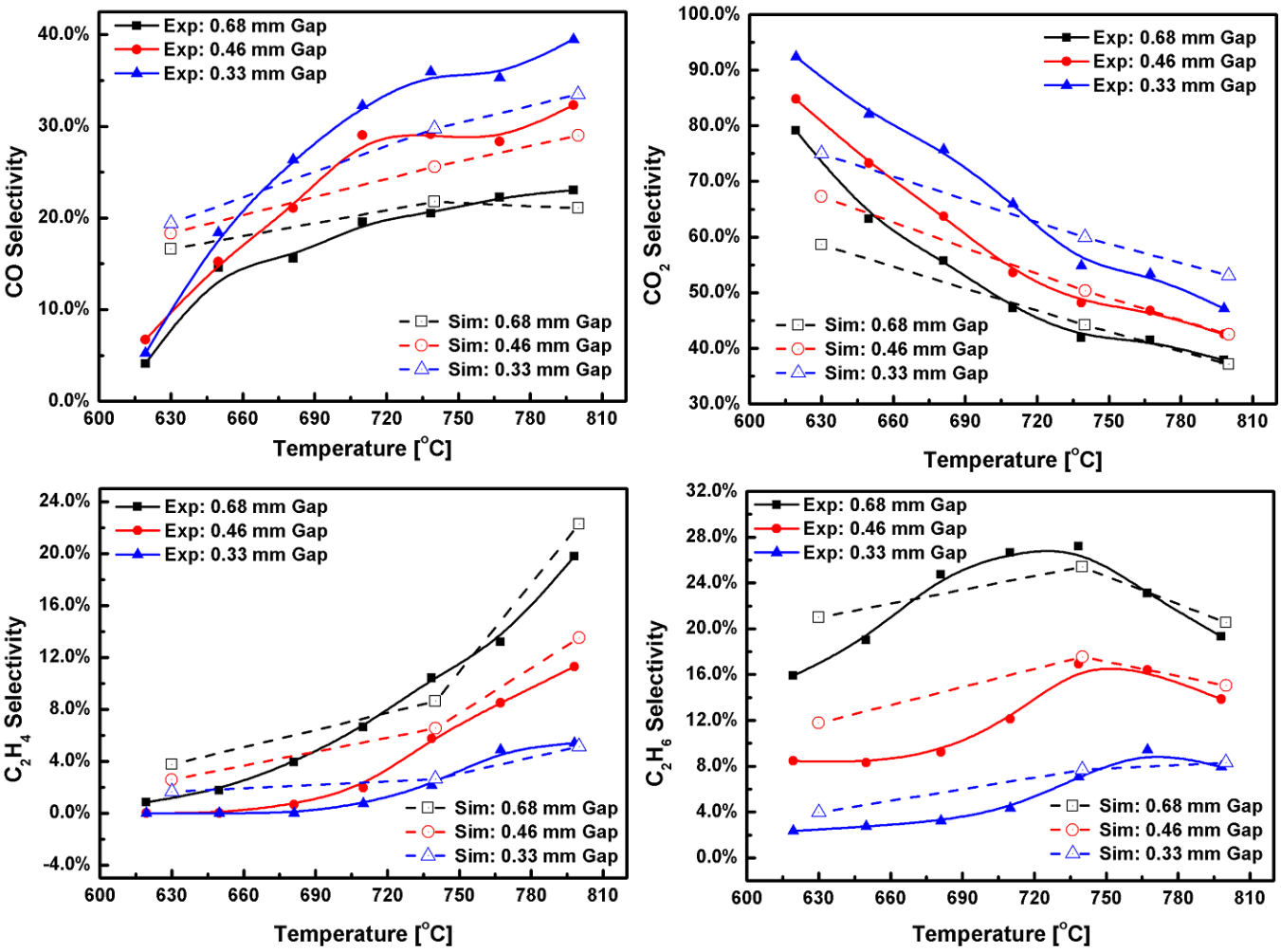

Figure 33. Comparison between simulation and experiment results for selectivity to C_1 (CO, CO_2) and C_2 (C_2H_4, C_2H_6) products at elevated temperature in OCM reaction under different gap sizes. Inlet feed condition: He dilution = 50%; C/O ratio = 2.0; residence time = 0.29 sec.

An important experimental findings discussed in Chapter 4.0 is that, decreasing the gap size can significantly shift the system towards C_1 formation against C_2 species. This is confirmed by numerical results and can be explained by that more C_2 species are destroyed catalytically as surface-to-volume increases. As shown in Figure 33, at 740 ^oC, for the case with 680 μm in gap size, 65% and 58% C_2H_4 and C_2H_6 are consumed on catalytic surface, respectively. The two values increase to 74% and 70% as gap size decreases to 460 μm, and to 93% and 90% for 330

μm case. The decomposition of C_2H_4 and C_2H_6 forms C_2H_3 and C_2H_5, which are decomposed quickly near the catalytic surface resulting in an increase of C_1 formation.

5.3.4 Spatially Resolved Profiles

To gain more insights into the simulation results for OCM system, spatially resolved profiles of flow rates of important species were acquired. For simplicity, results for cases with 680 μm and 330 μm in gap size were presented and compared with experiments. All flow rates were normalized based on the inlet total volumetric flow rate for convenience.

As presented in Figure 34, for CH_4 and O_2, the linear-type flow rate profiles are captured well by simulation, although there are some deviations for the absolution conversions for both species. For C_1 and C_2 products, the values at reactor exits are well captured, which is consistent with previous findings that integral selectivity to C_1 and C_2 products has a good agreement with experimental results. Moreover, since zero fluxes were manually imposed for all species other than CH_4, O_2 and He at the inlet of reaction chamber as boundary conditions, it is not strange that differences can be observed at reactor inlet for CO, CO_2 and C_2H_6. Also, in general, the spatially resolved profiles for C_2 are in good match with experiment, whereas there are large deviances for C_1 products. Especially is the profile for CO, which shows drastically different behavior. For the smallest gap size (330 μm), computed CO profile indicate CO is formed rapidly in the first half of the reaction chamber, which has been consumed later on leading to a slight decrease of CO flow rate. Compared with experiment curves, numerical simulation seems to overestimate the catalytic consumption step of CO due to the decrease of gap size.

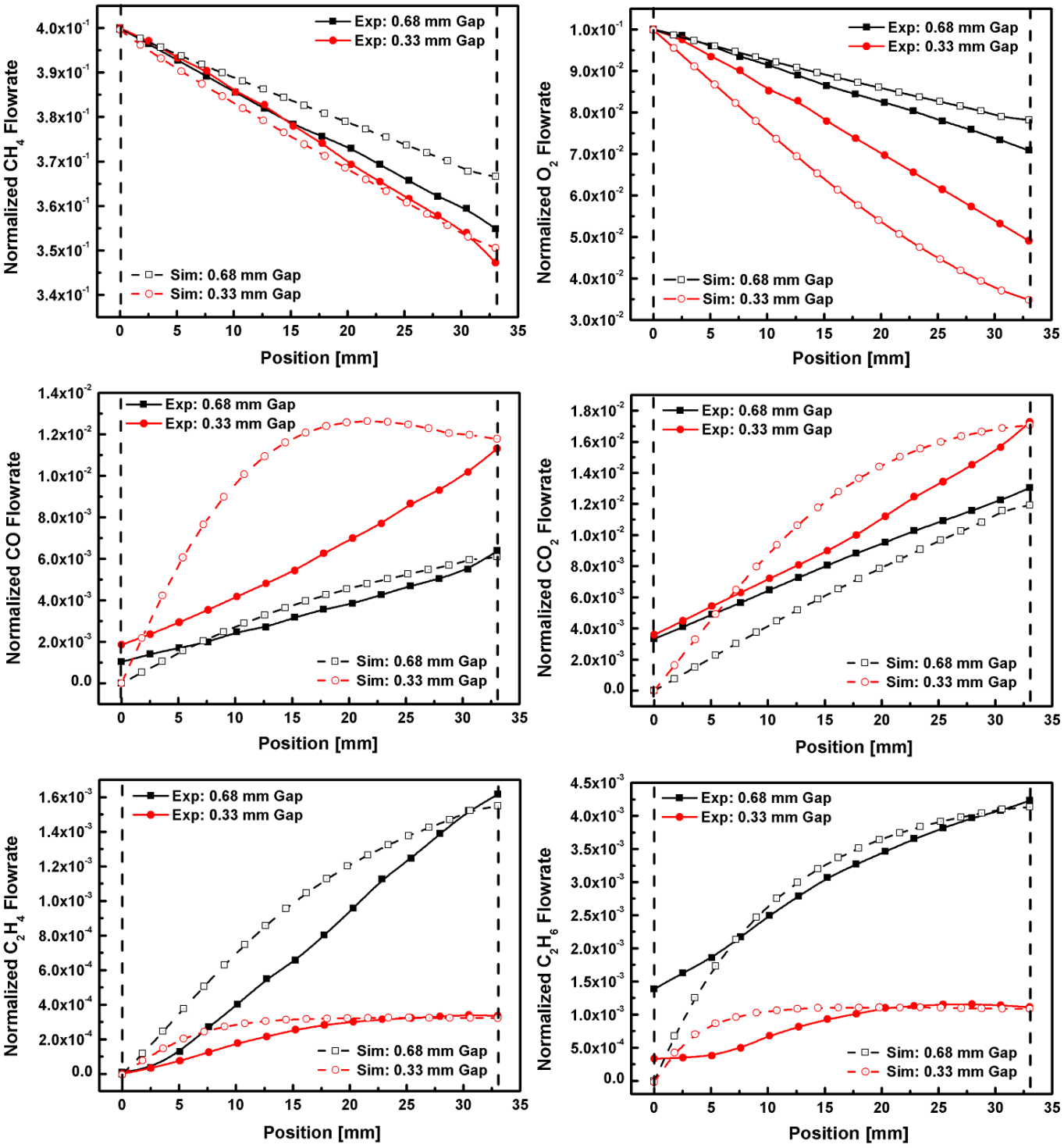

Figure 34. Comparison between experiment and simulation for the spatially resolved profiles of normalized flow rates for CH_4, O_2, CO, CO_2, C_2H_4 and C_2H_6 at 740°C (reactor outlet temperature). Inlet feed condition: He dilution = 50%; C/O ratio = 2.0; residence time = 0.29 sec

Since the reaction kinetics applied in this simulation is simply gained from reported literature for a similar catalyst (La–Sr/CaO) used in OCM reaction, and slight modifications were made on several catalytic reaction steps by using reactor exit data as the reference, thus deviances of spatially resolved profiles from actual experiment is not surprising. In order to further optimize this numerical model, reaction mechanism for this La_2O_3-based thin-film catalyst should be rigorously derived and developed. Then several simplifications applied in this model can be changed to more accurate physics, such as replacing the dilution model with the multicomponent transport. The energy balance and wall effect can also be incorporated into the system.

5.4 CONCLUSION AND SUMMARY

In summary, a 2D FEM-based model was built by using COMSOL Multiphysics to study the behavior of OCM reaction. In this model, the full Navier-Stokes equation was solved due to the low Peclet number of the system, which was coupled with mass transport as well as elementary reaction steps for both gas-phase and catalytic chemistries.

Steady-state as well as transient models were solved with results suggesting that catalytic reaction pathways on La_2O_3 surface are mainly responsible for the generation of important radicals, such as CH_3, C_2H_3 and C_2H_5. Reaction pathway analysis was performed with rates for important steps quantified. The influences of temperature and gap size on system behavior were studied and found in good agreement with experiment results. It can be concluded that: 1) r_3/r_4 ratio can be influenced by temperature, which plays key role in determine C_1 and C_2 selectivity; 2) decreasing the gap size can shift the system towards C_1 formation, mainly via re-adsorption

and decomposition of C_2 species formed by CH_3 coupling in the gas phase. Lastly, spatially resolved profiles for the flow rate of important species were acquired and compared with experiment. Results shows conversion for CH_4 and O_2, and the trend for C_2 are well captured. However, there are large deviances for C_1 products, indicating the potential drawbacks for the applied reaction mechanism.

6.0 EXPERIMENT ON OXIDATIVE DEHYDROGENATION OF ETHANE

6.1 INTRODUCTION TO ODH REACTION SYSTEM

Due to the continuously decreasing trend of liquid fossil fuel resources, the efficient utilization of the current light hydrocarbons becomes increasingly important. There are several strategies to deal with this issue. One of them is to first convert the light hydrocarbons into syngas, a mixture of CO and H_2, which can be further processed into desired chemical products and liquid fuel by a variety of industrially available technologies, i.e. the Fischer-Tropsch (FT) process to convert syngas into liquid transportation fuel [82]. Another alternative is to directly update small molecules (CH_4 and C_2H_6) into more useful/value chemicals. As Chapter 4 already pointed out, intensive effects have been devoted into developing commercially feasible chemical process for oxidative coupling of methane, which eventually turns out to be unsuccessful due to economic infeasibility.

In comparison, dehydrogenation of ethane to ethylene is a well-established industrial process. The product C_2H_4 is one of the most important building stocks in current petrochemical industry, which the global capacity estimated to be over 110 million tons per year [83]. Industrially, the large scale production of C_2H_4 is achieved by using steam crackers, in which endothermic pyrolysis reaction is carried out:

$$C_2H_6 \rightarrow C_2H_4 + H_2 \qquad \Delta H^0_{rxn} = 136 \;\; kJ/mol$$

Due to its endothermic nature, the reaction usually proceeds in large, heat-integrated reactors with significant amount of external heating. Also, the residence time for the reaction is relatively long, which is around 1 second. Therefore, such process can only be economic on very large scales, and the feasibility of scaling down the process for remote areas application becomes questionable.

The oxidative dehydrogenation of C_2H_6 to C_2H_4 (ODH), which was first demonstrated by Huff and Schmidt in 1993 [84], suggested a different route without drawbacks from the steam cracking method:

$$C_2H_6 + 0.5O_2 \rightarrow C_2H_4 + H_2O \qquad \Delta H^0_{rxn} = -105 \ \ kJ/mol$$

With the addition of relative small amount of oxygen (oxygen lean), the overall process turns out to be exothermic, thus no external heating is needed. Also, C_2H_4 can be produced within short contact times (~5ms). These characteristics favor its onsite production in small scale in remotes places. Moreover, with hydrogen addition to reactants streams passing through Pt-Sn catalyst, the selectivity of C_2H_4 was found to reach ~85% when over 70% C_2H_6 was converted [48]. This makes ODH competitive to conventional steam cracking in terms of C_2H_4 yield.

Spatially resolved sampling technique, after its first demonstration by Horn et al. [85], provides the possibility to disclose more insightful information for the reactive flow behavior, by understanding the rapid changes of spatial and temporal temperature and species compositional profiles. Very recently, the ODH studies over Rh and Pt coated monoliths have been expanded by incorporating this technique [61]. Spatially resolved profiles suggest that CPO of C_2H_6 over Rh can be considered as a multi-zone short contact time reactors (SCTRs), i.e. rapid oxidation of C_2H_6 was initiated with complete consumption of O_2 within the first few millimeters of the

reaction chamber, leading to the fast production of H_2, CO and H_2O.The was followed by a endothermic reforming reaction with additional syngas produced.

$$C_2H_6 + 2H_2O \rightarrow 2CO + 5H_2 \qquad \Delta H^0_{rxn} = 347 \quad kJ / mol$$

Comparatively, the multi-zone effect was not observed for CPO of C_2H_6 over Pt. The oxidation reaction was lower with CO and H_2O as primary oxidation products. The difference in reaction behavior suggests that reforming ability is an important distinguishing factor between Rh and Pt catalysts.

On the other hand, another reaction that ODH gains tremendous academic interest lies in the fact that it belongs to homogeneous-heterogeneous coupling reaction mechanism. Since the operating temperature of ODH is between 850 ^oC to 1050 ^oC, which is sufficiently high gas-phase kinetics participation. Various numerical simulations have been carried out to understand the complex interaction between gas-phase and catalytic chemistries in ODH. One remarkable example was demonstrated by Huff et al. [31] in studying the CPO of C_2H_6 on Pt catalyst, in which a one-dimensional plug-flow model was built with detailed elementary gas-phase and catalytic reaction steps included. Results suggest that the reaction is initiated by C_2H_6 oxidation on Pt leading to the formation of CO, CO_2 and H_2O. The heat released from the process causes a dramatic temperature increase in the gas phase and drives C_2H_6 dehydrogenation to C_2H_4. Thus, gas-phase does contribute significantly to the overall process. In the work recently done by Vincent et al. [23], the numerical model of ODH was further extended with more sophistication. Comprehensive gas-phase (44 species, 271 reversible steps) as well as catalytic reaction (35 absorbed species, 283 reversible steps) mechanism was developed based on experimental study. A 2D cylindrical channel was modeled with boundary layer approximation. Results show the rapid consumption of oxygen at the entrance leads to the selective oxidation of hydrogen on

catalytic surface. Heat released due to this is the key driver for gas-phase dehydrogenation of C_2H_6 to C_2H_4.

All these previous studies reveal the complex interaction between gas-phase and catalytic chemistries in ODH reaction. This brings forward a very interesting question: if the ODH is carried out in our microchemical reactor system, how the system will behave? How will the system respond to the decrease of the height of reaction chamber? Various kinetics mechanisms indicate that, for ODH on Pt catalyst, surface reaction pathway favors C_1 (CO, CO_2) formation, while C_2H_4 is predominantly produced by gas-phase dehydrogenation of C_2H_6, it is reasonable to predict that, decreasing the gap size can shift the system towards C_1 formation, a conclusion similar to OCM reaction as described in Chapter 4.0. More interestingly is to compare the system behavior of ODH over Pt and Rh as decreasing the gap size, as a major difference between two catalysts is the steam reforming ability on the catalytic surface. It is possible that the enhancement of steam reforming is more pronounced on Rh due to the change of gap size, leading to an increasing contribution of syngas against C_2H_4.

In summary, the work presented in this chapter aims to investigate ODH on Pt and Rh catalysts in the microchemical reactor system. Since the methodology is similar to OCM study described in Chapter 4.5, the experimental procedure is only briefly discussed in Chapter 6.2. So far, results for ODH on Pt have been collected, which will be presented in discussed in Chapter 6.3. Also, ongoing work for ODH, as well as problems need to be solved is discussed in Chapter 6.4.

6.2 EXPERIMENTAL PROCEDURE

Prior to reaction experiments, Pt- and Rh-based thin-film catalsts were synthesized based on the following method. Pt and Rh belong to commonly-used catalysts for ODH reaction which can lead to decent yields of C_2H_4 (Pt) and syngas (Rh). The Pt- and Rh-based catalyst on silicon substrate was prepared by dip coating method with corresponding precursors $H_2PtCl_6 \cdot 6H_2O$ (Sigma-Aldrich) and $RhCl_3 \cdot xH_2O$ (Rh 38-40 %, Sigma-Aldrich). The metal precursors were dissolved in ethanol (>99.8%, Pharmco-AAper) to prepare 20 mmol/L coating solution. Then, the silicon substrates (Cemat Silicon S.A.), which was ultrasonically cleaned for 10 minutes in acetone and rinsed several times with ethanol, was dipped into the coating solution and removed. It was then quickly inserted into a tube furnace which was preheated to 600 ^oC for 30 minutes. The dip coating and heating were repeated for 5 times. The coated substrate was finally acquired after calcination at 450 ^oC for 2 hours in air and reduced at 450 ^oC for 2 hours in hydrogen.

The reactivity and stability of Pt-based thin-film catalyst was then tested. Detailed experiments were then carried out in the microchemical reactor system. C_2H_6 (99.5%), O_2 (99.99%) and He (99.999%) were controlled by mass flower controllers and fed into the reactor. Reactor exit composition data were collected by GC at elevated temperatures controlled by the tube furnace. Temperature and species composition profiles were collected by mounting thermocouple/fused-quartz capillary on the sampling device, which was also connected to a MS. For the detailed methodology, please refer to the experiment procedure for OCM in Chapter 4.5, since ODH was carried out in a similar way.

6.3 RESULTS AND DISCUSSION

6.3.1 Catalyst Characterization and Stability Test

The Pt catalyst on silicon substrate was characterized by SEM with equipped EDX as shown in Figure 35. The elemental analysis identified only Pt and Si present in the sample, indicating the complete decomposition of precursor and reduction of active metal. As shown in SEM images (Figure 35, a and b), fresh Pt catalyst after synthesis shows relatively high surface coverage and small particle size, as a result of immediate ignition of ethanol in the oven preheated to a temperature (600 ^{o}C) higher than the autoignition point (362 ^{o}C). As shown in Figure 35 (c), after the ODH reaction at 800 ^{o}C, the coverage of Pt on silicon decreases as Pt particles sinter and form sphere morphology due to thermodynamic driving force. However, large scale SEM image (Figure 35, d) shows the majority of Pt particles maintain relatively small particle size.

The stability of Pt based thin-film catalyst was tested by running ODH reaction at 800 ^{o}C (highest temperature investigated) for 12 hours. Composition data for gas mixture at reactor outlet were taken from GC every half an hour. During the entire period of time, the reactivity of Pt catalyst was observed to be constant without any deactivation. Additionally, to study ODH behavior due to the change of the height of reaction chamber, it is critical to verify that the reactivity of Pt catalyst is not influenced by thermal cycling. The reason is that, the reactor system needs to be assembly and dissembled to change the height of reaction chamber, during which thermal cycling cannot be avoided. Thus, the catalyst was tested based on the following procedure: 1) ramping up temperature from 25 ^{o}C to 800 ^{o}C within 2 hours; 2) running the ODH reaction at 800 ^{o}C for 8 hours; 3) let the system cool down naturally to room temperature; 4) repeat steps 1 to 3 for three times. Experiment results showed that no apparent deactivation was

observed during thermal cycling tests, indicating Pt based thin-film catalyst was sufficiently stable for further study.

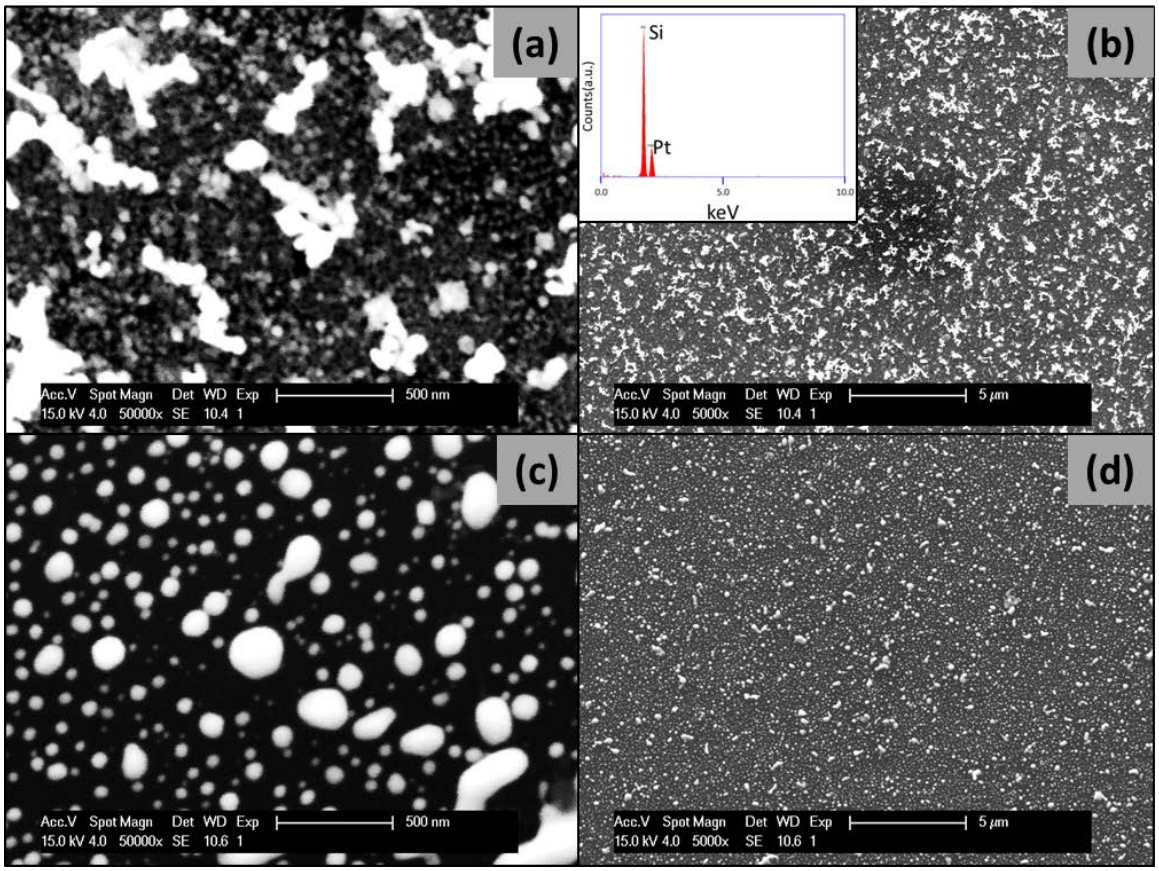

Figure 35. Pt on silicon substrate before (a and b) and after (c and d) ODH reaction with EDX (inserted).

6.3.2 Temperature Profiles

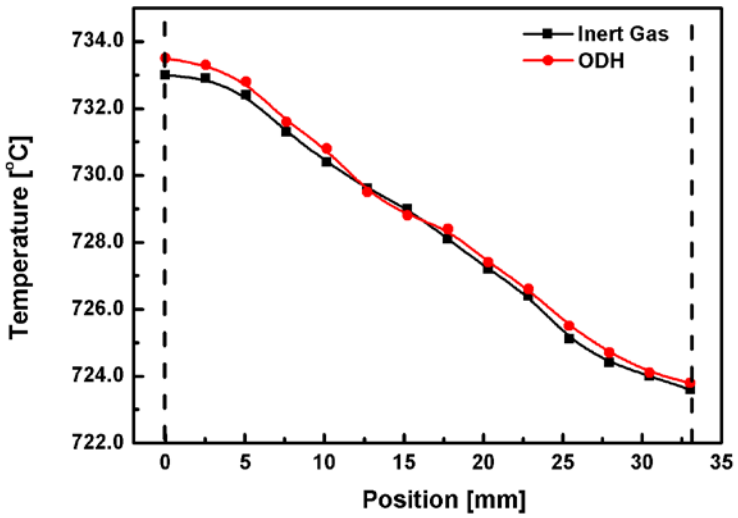

Figure 36. Comparison between two typical spatially-resolved temperature profiles within the reaction chamber with and without ODH reaction at 700.0°C (reactor outlet temperature) with 680 μm in gap height: 1) pure He flowed through the reactor, flow rate = 50 sccm; 2) with ODH reaction occurring, inlet feed condition: He dilution = 80%, C/O ratio = 2.0, flow rate = 50 sccm

Similar to OCM reaction, spatially resolved temperature profiles were first acquired and compared at elevated temperatures for the following two cases, with volumetric flow rate maintaining constantly at 50 sccm: 1) 100% helium; 2) reactive mixture with 80% helium dilution, C_2H_6/O_2 = 2. Typical temperature profiles were presented in Figure 36 when the reactor outlet temperature was held at 700 ^oC. Results show that temperature slight decreased towards reactor exit, and the maximum temperature difference is around 10 ^oC. Also, temperature profiles were found not influenced by the appearance of ODH reaction and adjustment of major operating parameters. Therefore, the same conclusion can be made for ODH that, the reaction can proceed in a quasi-isothermal reaction chamber.

6.3.3 Conversion and Selectivity

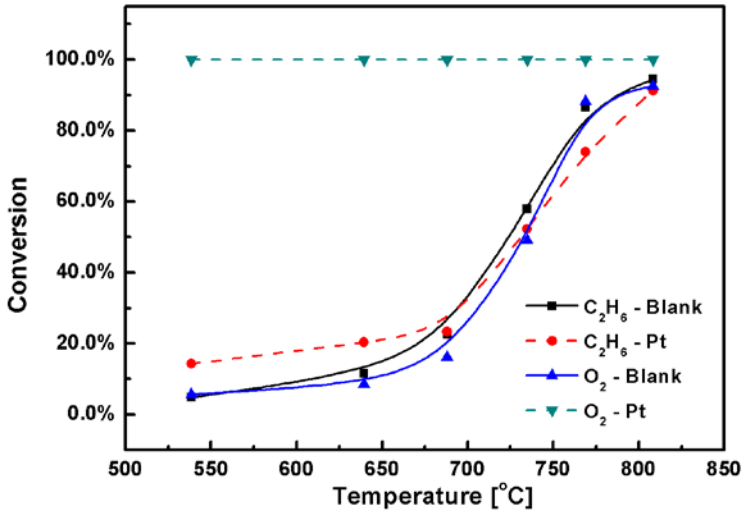

Figure 37. Conversion of C_2H_6 and O_2 at elevated temperature (measured at reactor outlet) for ODH reaction carried out in a blank reactor (full line) and using Pt-based thin-film catalyst, with the height of reaction chamber fixed at 680 μm. Inlet feed condition: He dilution = 80%; C/O ratio = 2.0; residence time = 0.13 second

As presented in Figure 37, the conversion data at reactor exit for both C_2H_6 and O_2 were compared for ODH reaction in blank reactor and with Pt-based thin-film catalyst fitted in the reaction chamber. The reactant mixture with 80% He dilution and C/O ratio fixed at 2 was applied as the reference. Generally, as temperature goes high, C_2H_6 conversion for two cases increases with relative slow pace in low temperature range (530 to 680 ^oC), then followed by a rapid increase between 680 ^oC and 800 ^oC. However, in the blank reactor, O_2 is consumed quite slowly at low temperature range and the trend over entire temperature is similar to C_2H_6. In comparison, by using Pt catalyst, 100% conversion of O2 was already achieved at the lowest temperature. Correspondingly, conversion of C_2H_6 was to some extent higher in the reactor with

Pt catalyst than blank reactor. These results suggest that, at low temperature, the inclusion of Pt catalyst can effectively accelerate the overall reaction by introducing relevant catalytic reaction pathways. However, this influence gradually decreases as the system approaches higher temperature, where homogeneous reaction pathways are expected to become more dominant. At the highest temperature investigated, over 90% of C_2H_6 and O_2 have been converted.

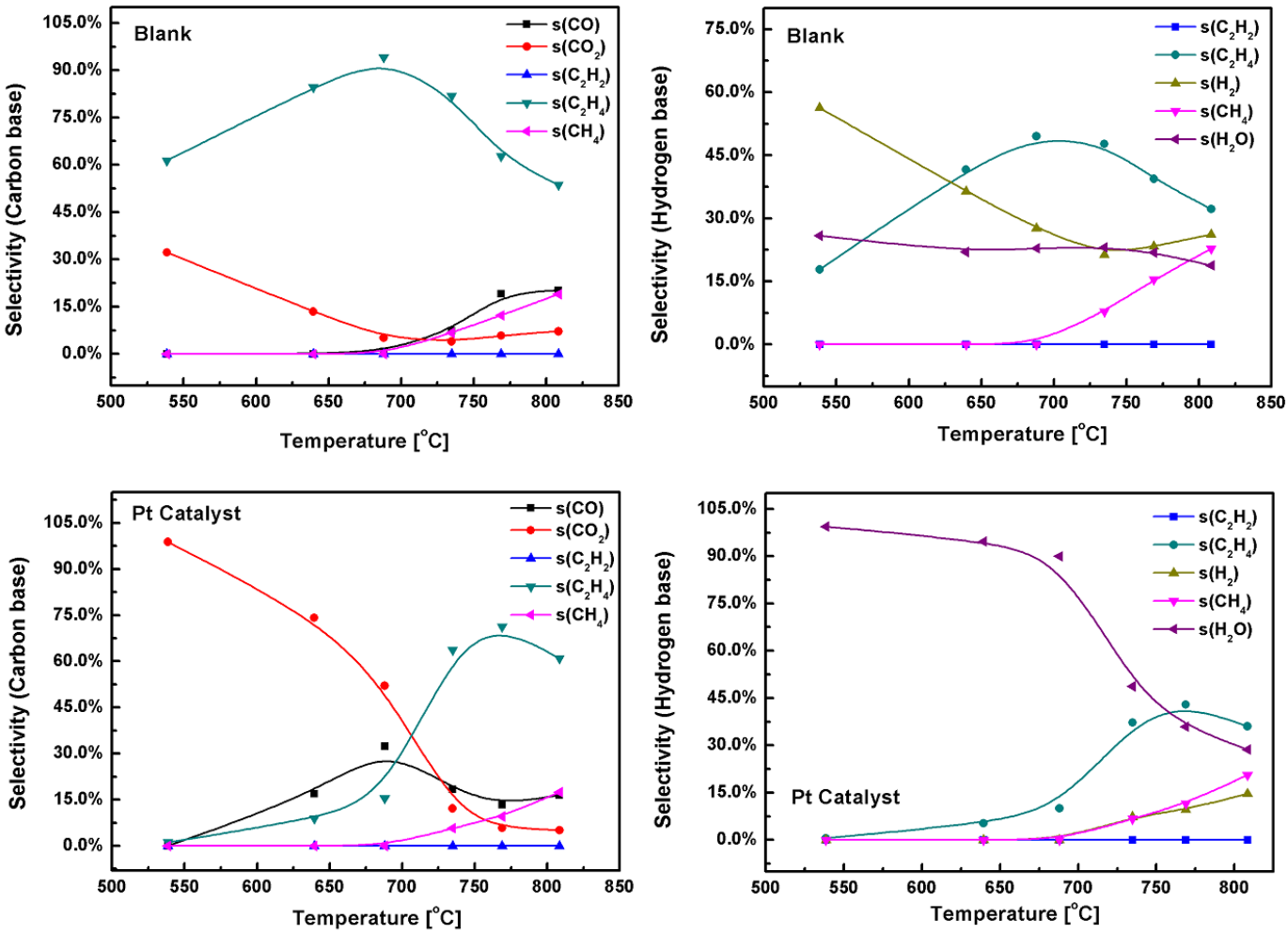

Figure 38. Carbon (left) and hydrogen (right) selectivity (element based) for important species at elevated temperature (measured at reactor outlet) for ODH reaction carried out in a blank reactor (top) and using Pt-based thin-film catalyst (bottom), with the height of reaction chamber fixed at 680 μm. Inlet feed condition: He dilution = 80%; C/O ratio = 2.0; residence time = 0.13 second.

Additionally, comparison of the selectivity curves (C and H element) indicates that ODH behaviors are fundamentally different between the two. As indicated in Figure 38, major products for ODH reaction are CO, CO_2, C_2H_4, CH_4, H_2 and H_2O. No acetylene (C_2H_2) was observed in the experiment.

The use of Pt catalyst favors total oxidation of C_2H_6 to form CO_2 and H_2O at low temperature, which is believed due to catalytic reactions steps. Selectivity to CO_2 and H_2O approaches almost 100% at 540 ^oC. As temperature increases, less available surface oxygen lowers the total oxidation rate and selectivity to CO_2 and H_2O decrease dramatically. Also, the increasing desorbing rate of CO leads to an increase proportion of CO as a product. C_2H_4 increases due to a more pronounced role for the gas phase mechanism. As the system approaches 800 ^oC, selectivity to C_2H_4 is hampered by the continuous increase of CH_4 formation, which may be explained by that high temperature favors relevant gaseous cracking steps towards CH_4.

Comparing the curves for the selectivity of the desired product ethylene, for the blank reactor, 90% peak value is reached at ~690 ^oC, while using Pt catalyst lowers this value to 74% at a much higher temperature 770 ^oC. This suggests two things: 1) the use of Pt catalyst has detrimental effect to ODH reaction; 2) pure homogeneous chemistry is sufficiently fast to ensure high yields of C_2H_4 and syngas under current reactor configuration and operating conditions.

6.3.4 Spatially Resolved Profiles

In order to gain further insights into the system behavior, and considering the drastic differences at different temperature for ODH reaction, spatially resolved profiles for species compositions have been acquired under 500 ^oC, 700 ^oC and 780 ^oC (oven temperature), with Pt-based thin-film catalyst applied. Figure 39, 40 and 41 below show the normalized flow rate for

important species, which is defined as the actual volumetric flow rate, divided by the total flow rate at reactor inlet.

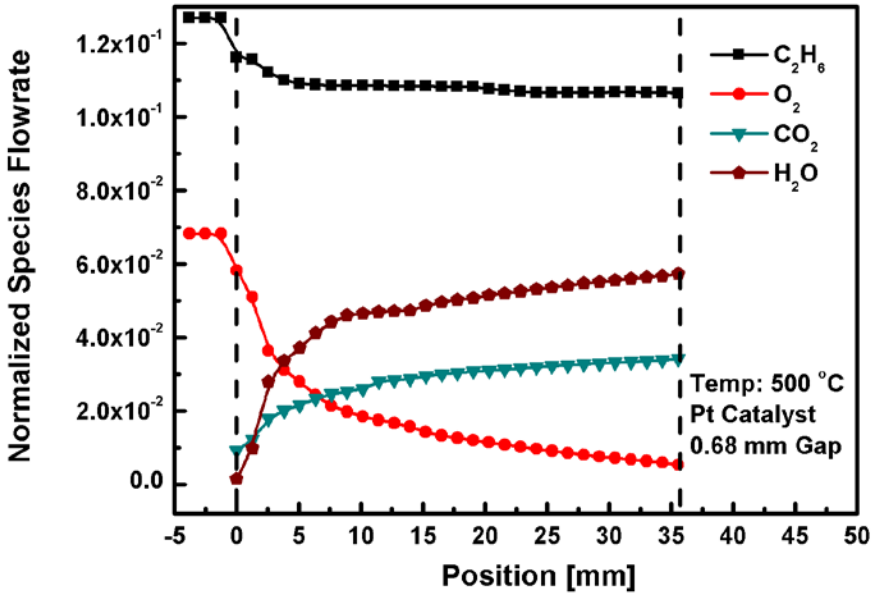

Figure 39. Spatially resolved profiles of normalized flow rates for all important species in ODH reaction at 500^{o} (reactor outlet temperature). Pt-based thin- film was used as the catalyst. Inlet feed condition: He dilution = 80%; C/O ratio = 2.0; residence time = 0.13 second.

At 500 ^{o}C (oven temperature), ~15% C_2H_6 and 100% O_2 have been consumed with CO_2 and H_2O been identified as products. Spatially profiles suggest over 60% of O_2 has been consumed in the first 5 mm within the reaction chamber, accompanied by a fast increase CO_2 and H_2O signal. Thus, at this temperature, Pt-catalyzed total oxidation dominates the reaction behavior and the homogeneous kinetics is trivial.

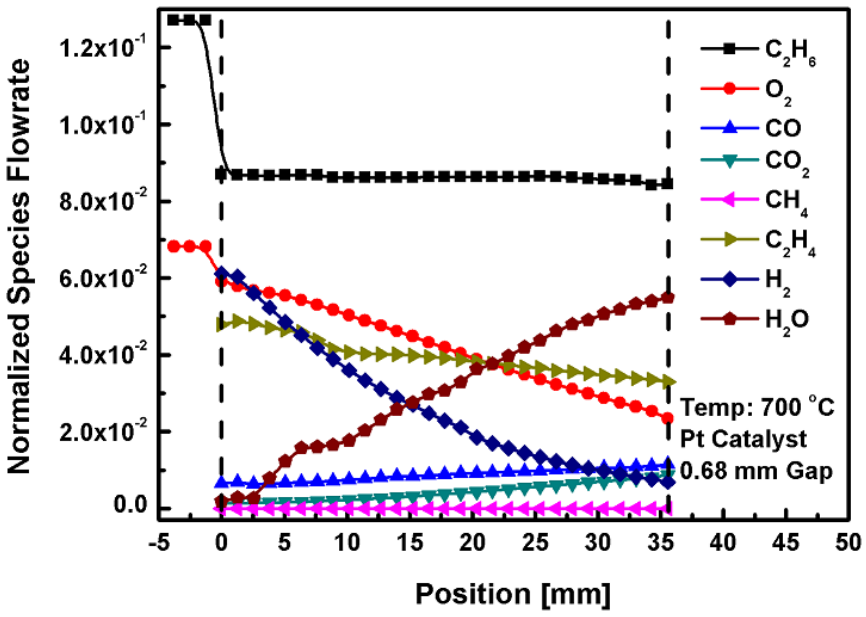

Figure 40. Spatially resolved profiles of normalized flow rates for all important species in ODH reaction at 700^{o} (reactor outlet temperature). Pt-based thin- film was used as the catalyst. Inlet feed condition: He dilution = 80%; C/O ratio = 2.0; residence time = 0.13 second.

As the temperature increases to 700 ^{o}C, the system behaves totally different: 1) C_2H_6 consumes instantaneously to the exit conversion at reactor inlet; 2) C_2H_4, H_2 appear in large concentrations at reactor entrance due to consumption of C_2H_6; 3) H_2, O_2 signals decreases with H_2O signal continue to increase; 4) CO, CO_2 concentrations are tiny at reactor inlet, which show a monotonic increase towards reactor exit; 5) trivial amount of CH_4 amount is observed. The trends are in well agreement with conversion and selectivity curves presented previously. A major point can be concluded from these trends is that: the gas-phase chemistry is extremely fast and reactions occur instantaneously, once reactants are fed into the reaction chamber. Also, C_2H_4 gradually decrease towards reactor exit, which may be explained by the occurrence of steam reforming of C_2H_4 on catalytic surface, when H_2O is in large excess.

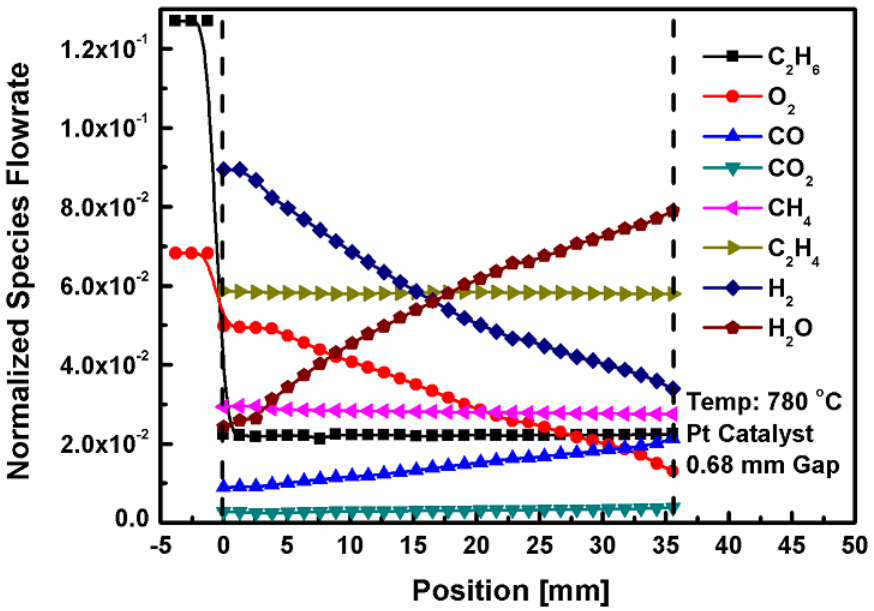

Figure 41. Spatially resolved profiles of normalized flow rates for all important species in ODH reaction at 780° (reactor outlet temperature). Pt-based thin- film was used as the catalyst. Inlet feed condition: He dilution = 80%; C/O ratio = 2.0; residence time = 0.13 second.

Similar conclusion can be made for spatially resolved species profiles at 780 °C (oven temperature). Due to the fast gas-phase kinetics, C_2H_6, C_2H_4 signals are almost flat. CH_4 is also formed at reactor inlet without further change downstream. The gradual decrease of H_2 and O_2 leads to increasing formation of H_2O. Also, high temperature favors CO formation, with tiny amount of CO_2 formed.

6.4 CONCLUSION AND OUTLOOK

In summary, ODH reaction has been selected as the second model reaction to be tested in the microreactor system developed in our group. Pt- and Rh-based thin-film catalysts were synthesized for ODH study. ODH was carried out with (Pt) and without catalyst (blank reactor)

when the height of reaction chamber was fixed at 680 μm. Conversion and selectivity data for the two cases demonstrate that blank reactor leads to a better yield for C_2H_4, while Pt catalyzed reaction has detrimental effect to C_2H_4 selectivity.

Spatially resolved profiles for species composition were acquired at 500 ^oC, 700 ^oC and 780 ^oC for Pt-catalyzed ODH, which show drastically different behavior. At low temperature heterogeneous reactions dominate, leading to fast consumption of C_2H_6 and O_2 in the first few millimeters in the reaction chamber. The primary products are CO_2 and H_2O. However, profiles for two higher temperatures indicate an extremely fast gas-phase reactions taken place at reactor inlet, which may be due to the isothermal condition, as well as the relative large residence time (~ 0.15 second).

This extremely fast kinetics results in an ineffectiveness to capture the reactive flow behavior by spatially resolved sampling technique. The effects for ODH due to the change of gap size also cannot be studied. Therefore, the ongoing work focuses on the following aspects: 1) increasing the total volumetric flow rate (decreasing the residence time) or increase inert dilution; 2) study the gap size effect for Pt-catalyzed ODH; 3) study the Rh-catalyzed ODH and compare to results using Pt-based catalyst.

7.0 PLAN AND OUTLOOK

The successful design of the current microchemical reactor system may open a new pathway to study the HH coupling reaction systems in a more accurate manner. Combined with FEM-based CFD modeling coupled with detailed elementary gas-phase and catalytic chemistries, the HH coupling effect is hopefully to be thoroughly understood. In below, several important reaction systems are discussed as potential candidates for future study, which are hydrogen oxidation, oxidative dehydrogenation of ethane, and catalytic partial oxidation of propane to syngas. These reactions are all belong to the category of high temperature oxidation of light alkanes.

The purpose of such selection is to demonstrate the idea and methodology in similar and relative simple reaction systems. In general, the catalytic surface in these reactions serves as two roles: it may lower gas-phase kinetics by capturing important radicals and convert them via other catalytic reaction channels; or it accelerates the gas-phase kinetics by pumping radicals and reactive intermediates into the gas phase. Additionally, another important factor needs to be considered is the intrinsic nature of the reaction system, i.e. to how large extent that catalytic chemistry contributes to the overall reaction behavior against gas-phase chemistry.

7.1 HYDROGEN OXDIATION REACTION

Catalytic oxidation of hydrogen is a very important yet simple reaction, which belongs to a subset of the oxidation of light hydrocarbons (e.g. CH_4 and C_2H_6). This reaction has been studied for many years and is relatively well understood [68, 86]. It has found various fields for application, such as rocket propulsion and catalytic combustion in a microburner as a portable energy device [87]. However, the reaction is characterized by wide flammability limits (~3-75% vol. based in air) and thus has been restricted from practical application due to its hazardous explosive nature.

As mentioned in Chapter 1.2, Veser et al. reported a safe operation during the catalytic oxidation of hydrogen in a micro-based reactor [16], in which successful suppression of gas-phase chemistry was expected to be achieved via radical as well as thermal quenching. Further numerical tests performed by Chattopadhyay et al. confirmed the radical quenching effect, as well as the possibility to alter HH coupling behavior by adjusting the critical dimension of reaction chamber [1]. Additionally, the complete suppressing of homogenous reaction pathways at small critical dimensions indicates a possible way to operate hydrogen oxidation reaction as an intrinsically safe chemical process.

In the future, hydrogen oxidation reaction can be studied based on the methodology developed in the study of OCM and ODH reaction systems. Both numerical simulation and experiment can be carried out for this reaction. On the numerical side, previous numerical model has several drawbacks: 1) isothermal assumption; 2) only steady-state solution was acquired; 3) boundary layer approximation; 4) wall effect was not considered. Actually, a new model that overcomes these drawbacks has been developed and studied a while ago. However, it fails to acquire the final solution due to the very fast gas-phase and catalytic chemistries and the

coherent coupling between the two. Thus, the tiny time step results in an unacceptable computation time to solve the entire transient behavior. Therefore, the model needs to be somehow optimized (algorithm/mesh configuration) to reduce the computation time and only then hydrogen oxidation can be systematically studied.

Experimentally, while the entire methodology is similar, the major challenge is the high temperature and the potential danger of explosive mixture. To study HH coupling behavior, system temperature needs to be reached well above 1000 ^{o}C to trigger the gas-phase reaction pathways [16]. Thus, an update of current microchemical system is necessary by replacing MACOR by more thermally resistant materials. Still, hermetic sealing as well as inert surface of reaction chamber is required. Although looks quite challenging, it is worthwhile to continue since an intrinsically safe process might be robustly demonstrated by both experiment and simulation.

7.2 OXIDATIVE DEHYDROGNATION OF ETHANE (ODH)

As discussed in Chapter 6.0, oxidative dehydrogenation of ethane to ethylene (ODH) is seen as a potential alternative to produce C_2H_4, which has been demonstrated experimentally to achieve a comparable yield compared to conventional steam cracking method used in industry. Due to the HH coupling characteristic of ODH, experimental efforts have already been devoted in the study of ODH system. As pointed out in Chapter 6.0, the major issue now confronted for is that the extremely fast gas-phase kinetics can occur in the reaction chamber, which is the major obstacle for acquiring well-resolved spatial compositional profiles.

Compared to other ODH studies in monolith reactor [31, 88, 89], this issue is believed to be originated from two aspects: 1) relatively long residence time (RT = ~0.15 sec) compared to conventional operating in short-contact-time reactor (SCTR) (RT =~5 ms), i.e. RT in this study is ~25 times than in SCTR. Since gas-phase chemistry is the dominating factor in ODH, it is not surprising that gas-phase kinetics is so fast in this study; 2) isothermal condition created in the microchemical reactor system makes it more difficult for spatial concentration profiles to be decoupled. Spatial temperature profile for ODH running in SCTR starts with very low temperature (~100 ^{o}C) [61], although it can reach over 1000 ^{o}C due to strong exothermic nature of ODH. This low temperature at reactor entrance, which suggests relatively slow gas-phase kinetics, may favor a better resolved composition profile. Comparatively, in the current experimental setup, reactants have already been preheated to a specified temperature controlled by tube furnace, indicating a fast reaction as soon as fuel and oxidant are contacted at reaction inlet.

To overcome this obstacle and get better resolved spatial profiles, the first thing to try is to increase the total volumetric flow rate (lower the RT) of reactants at inlet, as it might lower the reaction rates of gas-phase chemistry. After this issue being solved, the gap size effect can be systematically studied for both Pt- and Rh-catalyzed ODH, the former of which favors ethylene production while the latter favors syngas. The experimental procedure is expected to be similar as for OCM study.

By studying the gap size influence, we can know better how homogeneous and heterogeneous chemistries contribute to the overall system, and through which steps they are interacted with each other. For Pt-catalyzed ODH to product C_2H_4, previous literature [90] reported that catalytic oxidation of C_2H_6 was initiated closed to reactor inlet, and the heat

released due to this step was responsible for C_2H_6 dehydrogenation in gaseous phase. Also, catalyst surface favors the formation of C_1 species. Therefore, it is reasonable to predict that, decreasing the gap size can lead to a faster decrease of C_2H_6 and O_2 signals, and the system can be biased towards C_1 formation against C_2H_4. The heat effect, however, is less likely to be observed because of the isothermal condition of reaction chamber. In comparison, Rh-catalyzed ODH is expected to have more interactions between gas-phase and catalytic chemistries, since Rh favors steam reforming (SR) for C_2H_4 and C_2H_6. Thus, as the gap size decreases, SR steps are expected to be enhanced, resulting in an increasing formation rate of syngas.

Another experiment worthwhile to be carried out is to run Pt- and Rh-catalyzed ODH autothermally, as what have been done in SCTR. To achieve this, an initial temperature ramp is necessary to trigger ODH reaction, then the tube furnace can be shut down and thermal insulation is needed to wrap around the reactor system to prevent heat loss. The difference compared to running ODH isothermally lies in that, thermal effect is expected to become more pronounced and can be fully coupled with the gap size effect. Therefore, the system can show more complexity under this condition. It may also be interesting to study the effect of hydrogen addition, which is expected to drive temperature up at inlet due to its catalytic oxidation on the reactive surface.

Lastly, numerical simulation can be carried out to study the ODH behavior for all cases that has been mentioned for ODH experiment. This is feasible since both gas-phase and catalytic chemistries (on Pt and Rh) are relatively well understood [23, 36]. By modeling ODH behavior under isothermal condition, energy field can be excluded as what has been done for OCM simulation. Energy conservation equation can be then included to study ODH at autothermal

conditions as well as the effect of hydrogen addition. By comparing with experiment results, it is hope that how the gap size effect interacts with thermal effect can be thoroughly revealed.

7.3 CATALYTIC PARTIAL OXDAITION OF PROPANE (CPOP)

Another potential system for future study is the catalytic partial oxidation of propane (CPOP) to produce syngas. As suggested by Beretta et al. [21] very recently, CPOP running in short-contact-time reactor (SCT) over Rh-based catalyst was observed to have a synergy effect between catalytic (releasing reactive molecules by steam reforming) and gas-phase chemistries (gas-phase kinetics enhanced by the additives). The spatially resolved temperature and species composition profiles suggest a multi-zone effect, with a fast consumption of C_3H_8 and O_2 close to reactor inlet that drives temperature up dramatically in the gas phase, accompanied by the endothermic steam reforming (SR) of CH_4, C_2 and C_3 species with extra syngas produced. The entire behavior is quite similar to Rh-catalyzed ODH.

Similar to Rh-catalyzed ODH, it is interesting to run CPOP with the tube furnace specified at fixed temperature. By performing the spatially resolved measurement for temperature within the reaction chamber at varying conditions, a conclusion can be made whether an isothermal environment can be created that is similar to previous OCM and ODH study. Gap size effect can be studied afterwards, and more interaction behavior is expected since more molecules can involve in the interaction between gas phase and catalytic surface, compared to the case for ODH.

Moreover, it is also worthwhile to run CPOP at autothermal condition. Similar temperature and species compositional profiles are expected to appear as suggested by previous

literature [21]. Decreasing the gap size may: 1) drive the temperature to higher values near inlet due to a fast oxidation reaction; 2) shift the temperature curve down in the “reforming” zone due to more endothermic SR steps; 3) dramatically impact the species compositional profiles, especially ones for the reactive intermediates, i.e. CH_4, C_2 (C_2H_4, C_2H_6) and C_3 (C_3H_6) species.

Lastly, numerical simulation can be performed for CPOP reaction with detailed elementary reaction steps incorporated [91, 92]. Both isothermal and adiabatically autothermal conditions can be considered in the model. Similar to ODH, by comparing with experimental data, it is hope that the HH interaction behavior in response to the change of gap size, and the accompanied thermal effect can be fully explained.

APPENDIX A

DESIGN OF THE MICROCHEMICAL REACTOR SYSTEM

A.1 THE DESIGN OF THE SEALING INTERFACES

Two different sealing mechanisms were used in the reactor system design: 1) sealing interface between alumina tubes and MACOR-based parts; 2) sealing on the top surface of the main reactor part.

For the former, as Figure 42 shown below, at all connection interfaces between alumina tubes and MACOR-based parts, a concentric gap was designed (gap size, 0.250 mm) for the joint pairs, which were assembled together followed by a standard treatment method.

The detailed treatment is specified as two consecutive steps: 1) Ceramic paste (503-VFG, Aremco Products) is filled in the concentric gap for the well-positioned joint pair, which will be bonded together after being located in a tube furnace for heat treatment. 2) After first-stage treatment, ceramic paste thinner (503-T, Aremco Products) is applied at all bonded interfaces and the second heat treatment is required to finish the assembly process. For any joint pair, the first step is needed to bond two parts with each other, and by applying a compatible thinner in the second step, smaller ceramic particles in the thinner will diffuse and fill in the porous structure of the interface, turning it into a much dense structure for gas-tight sealing purpose.

The detailed heat treatment procedure is: a) stay at room temperature for 3 hours; b) then gradually ramp up to 93 ^{o}C within 30 minutes; c) stay at 93 ^{o}C for 2 hours; d) ramp up the temperature to 260 ^{o}C within 30 minutes; e) stay at 260 ^{o}C for 2 hours; f) ramp up the temperature to 371 ^{o}C within 30 minutes; g) stay at 371 ^{o}C for 2 hours; h) cool down naturally to room temperature. Additionally, it needs to be emphasized that each joint interface needs such a heat treatment for assembly. Since there are twelve interfaces for the entire micro-chemical reactor system, the assembly process should be conducted in a very rigorous procedure: 1) assemble all relevant alumina tubes with MACOR-based elbows; 2) connect left and right elbows with the main reactor by locating the alumina tubes into the correct places; 3) connect the main reactor with the small alumina tube for the in-situ data acquisition device (spatially resolved measurement).

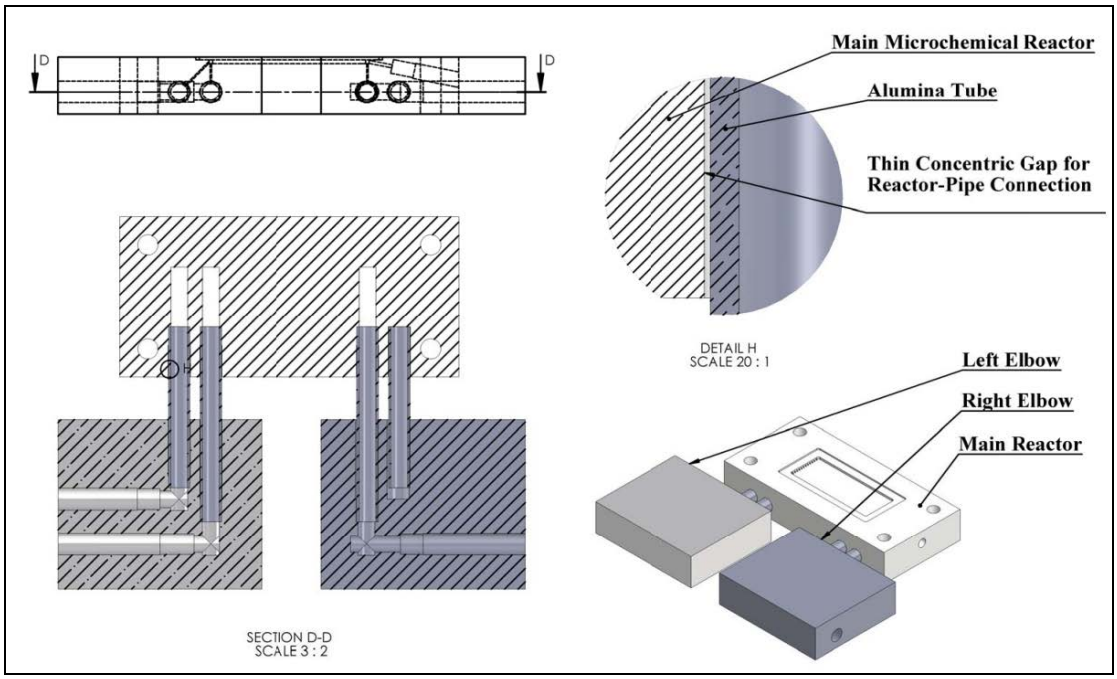

Figure 42. Sealing mechanism 1: design of the sealing interface between alumina tubes and MACOR-based parts, e.g. interfaces between main microchemical reactor and elbows (drawn in AutoCAD 2009).

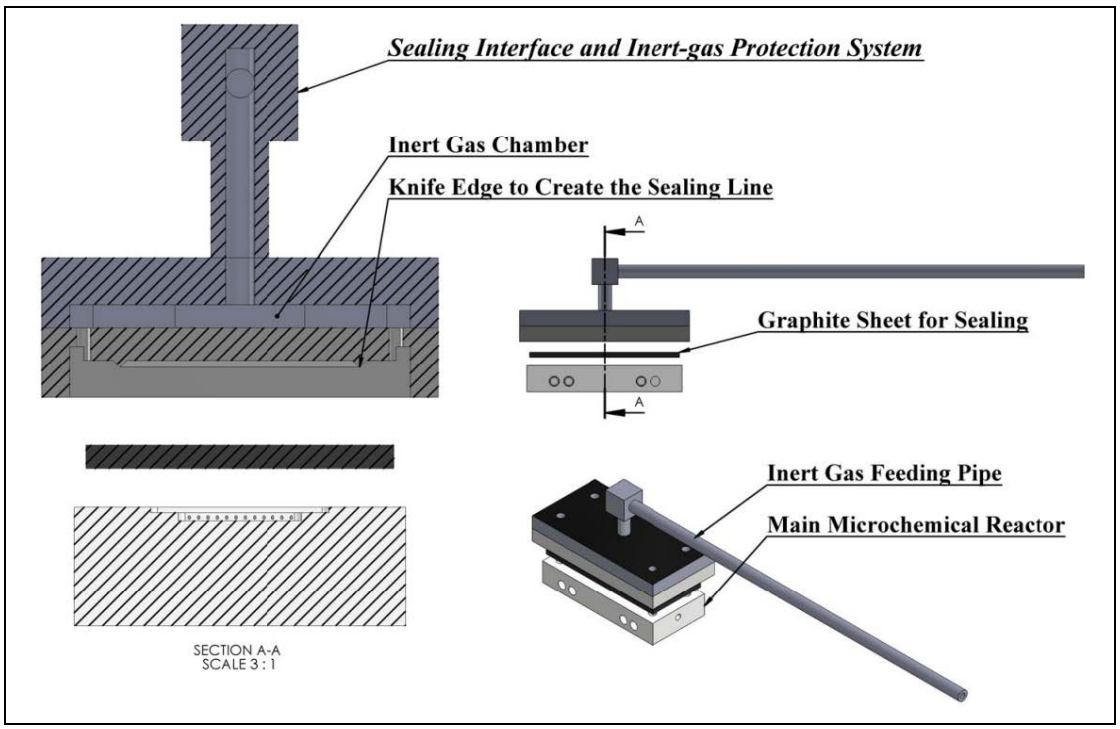

Figure 43. Sealing mechanism 2: design of the inert gas protection system and sealing interface for the reaction chamber at the top surface of the main reactor (drawn in AutoCAD 2009).

Figure 43 shows the schematic of the second type of sealing interface. A customized inert gas protection system (part 4) was designed, which includes a sealing plate, an accessory plate and a gas feeding pipe. The accessory plate has a void chamber to store the inert gas and a channel to connect to the feeding pipe. The sealing plate has a series of uniformed distributed microchannels (ϕ = 0.06", 14 channels) on the top, and a closed curve with knife edge (angle = 90^{o}), which covers the area of silicon substrate that sits on top of the main reactor. Also, the gas-feeding pipe is made to be a long channel with one end connected to the accessory plate, and the other is welded to a Swagelok hose connector (ID = 1/8") for inert gas feeding. All three parts were welded together to form a complete sealing system. Detailed design information can be found in Appendix D.

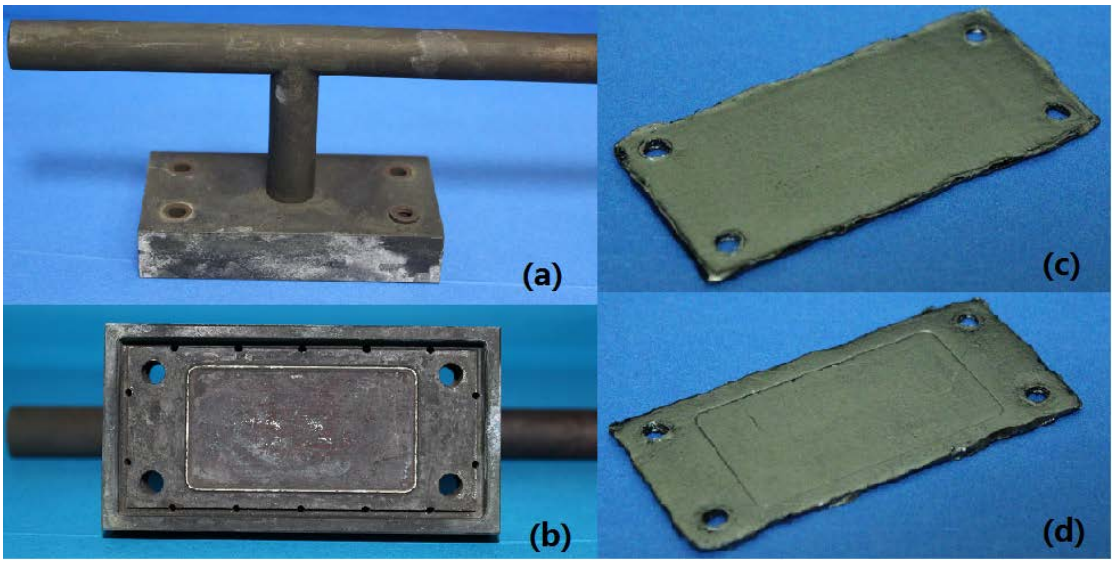

Figure 44. Actual photo of the inert gas protection system (a, b) and the comparison between the graphite gasket before (c) and after (d) mechanical compression.

As shown in Figure 43 and 44, the sealing between the sealing plate and the main reactor is achieved by inserting and compressing a well-cut graphite gasket (McMaster-Carr). Gas-tight sealing is realized by forming a closed sealing line between the knife edge and graphite gasket due to mechanical compression. After assembly, the inert gas protection system can provide an evenly-distributed inert gas on the peripheral of the graphite gasket, and thus protect it from oxygen attack from the surrounding oxygen environment.

Repeated tests demonstrate that, by applying the two sealing mechanisms mentioned above, the overall leakage level for assembled micro-chemical reactor system is less than 5% of the total flow rate, either under thermal cycling operations from room temperature up to 800 ^{o}C, or operating at 800 ^{o}C for 12 hours.

A.2 THE DESIGN OF DATA ACQUISITION DEVICE FOR SPATIALLY RESOLVED MEASUREMENT

A novel data acquisition device was designed and incorporated into to this micro-chemical reactor system, with the purpose of measuring spatially resolved profiles of temperature and species compositions within the reaction chamber in situ. By referring to an in-situ sampling system developed by Horn et al. [20, 93], a customized profile sampling device was developed for the microchemical reactor system.

As shown in Figure 45 and 46, a one-dimensional translational actuator (Zaber Technologies) has been mounted on a standard lab jack with triangular aluminum support put in between to provide an incline with appropriate angle (5.00^{o}), which is compatible with the angle of the thin alumina tube that has been inserted into the main reactor part. The actuator can be controlled by an incorporated micrometer. Also, the displacement range of the actuator was selected to be 40 millimeters, which is slightly larger than the overall length of the reaction chamber (~36 mm). In order to hold the thermocouple and quartz capillary on the actuator, a Teflon-made clamp was designed and mounted on the actuator. Moreover, a union tee (1/8”, Swagelok) was welded on the actuator with one end connected to the quartz capillary and the other end to a mass spectrometer (MS) (OmniStar^{TM}, Pfeiffer Vacuum) for gas composition analysis. Temperature and species compositional profiles can be achieved by one-dimensional translational scanning of thermocouple/quartz capillary in the direction of the gas flow. So far, the movement is controlled by adjusting the micrometer manually. To enable automatic scanning is feasible, but it is not necessary at this moment. Therefore, all the spatially resolved profiles in this thesis are acquired under the manual mode.

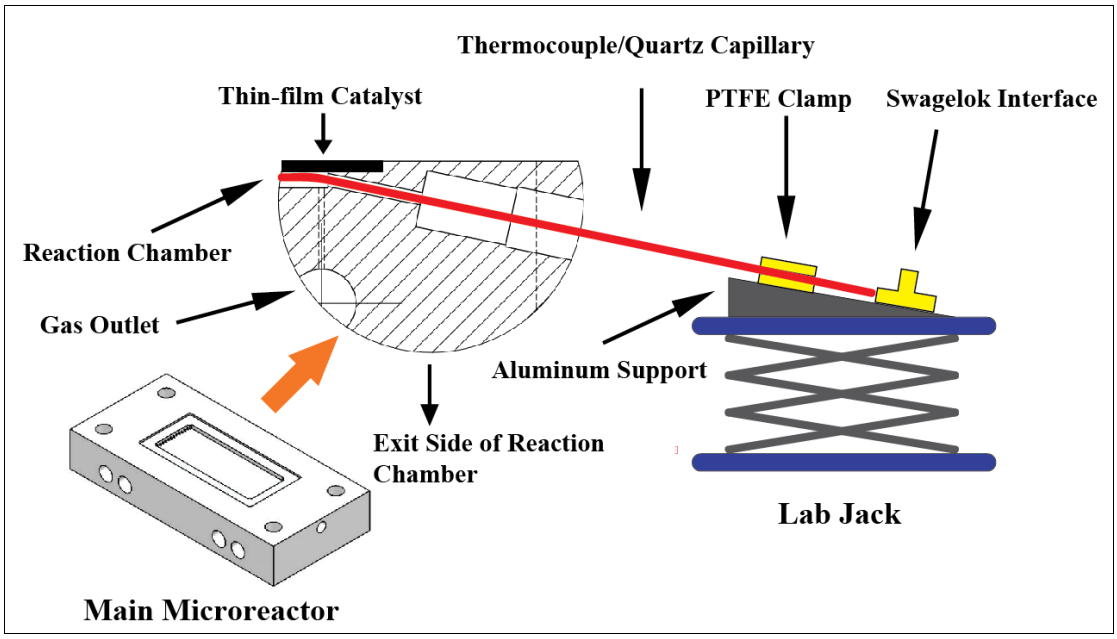

Figure 45. Schematic of the design of the in-situ measurement device and its incorporation into the main microchemical reactor (drawn in AutoCAD 2009).

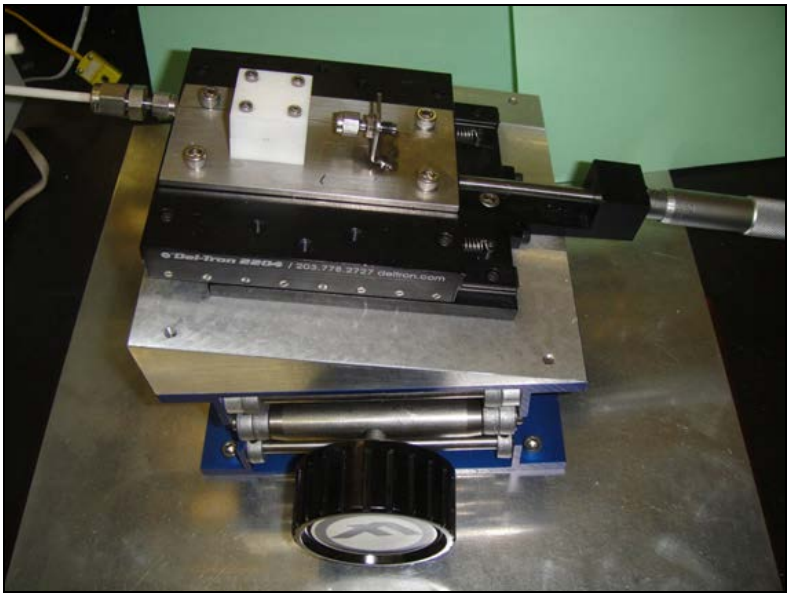

Figure 46. The photo of the actual in-situ measurement device.

APPENDIX B

MATHEMATICAL EXPRESSIONS FOR THE NUMERICAL MODEL

B.1 REACTOR MODELING

In this model, fluid flow belongs to single-phase, compressible laminar flow. Navier-Stokes equation and the equation of continuity are coupled together to describe the flow behavior:

Compressible formulation of the continuity equation:

$$\frac{\partial \rho}{\partial t} + \nabla \bullet \left(\rho \mathbf{u} \right) = 0 \qquad \text{(Eqn. B.1.1)}$$

where ρ (kg/m^3) denotes the density of fluid (gas mixture) and **u** (m/s) is the velocity vector.

Navier-Stokes equation:

$$\rho \frac{\partial \mathbf{u}}{\partial t} + \rho \mathbf{u} \bullet \nabla \mathbf{u} = -\nabla p + \nabla \bullet \left(\mu \left(\nabla \mathbf{u} + \left(\nabla \mathbf{u} \right)^T \right) - \frac{2}{3} \mu \left(\nabla \bullet \mathbf{u} \right) \mathbf{I} \right) + \mathbf{F} \qquad \text{(Eqn. B.1.2)}$$

where p (Pa) is pressure; μ (Pa·s) denotes mixture viscosity and **F** (N/m^3) is the volume force vector. Ideal gas law provides the equation of state for a multicomponent gas mixture as

$$\rho = \frac{p}{R_g T}\bar{M} = \frac{p}{R_g T}\sum_{k=1}^{K_g} X_k M_k \qquad \text{(Eqn. B.1.3)}$$

where R_g is the universal gas constant, equals to 8.314 (J/(mol·K)); $\bar{M}$ (kg/mol) represents the mean molecular weight; M_k (kg/mol) is the molecular weight of gas-phase species, which has been indexed by k from 1 to K_g. K_g is the number of total gas-phase species.

Current model assumes chemical species are transported through diffusion and convection, and implement the mass balance equation

$$\frac{\partial c}{\partial t} + \mathbf{u}\cdot\nabla c = \nabla\cdot\left(D\cdot\nabla c\right) + R \qquad \text{(Eqn. B.1.4)}$$

where c (mol/m^3) is the concentration of chemical species; D (m^2/s) denotes the diffusion coefficient; R (mol/(m^3·s)) is the net formation rate of the species; and **u** (m/s) denotes the velocity vector.

In equation 3, binary diffusion coefficients are used with argon as the reference, which can be expressed based on the kinetic gas theory

$$D_{AB} = 2.66\times10^{-2}\frac{\sqrt{T^3(M_A+M_B)/(2\times10^3 M_A M_B)}}{p\sigma_A\sigma_B\Omega_D} \qquad \text{(Eqn. B.1.5)}$$

where D_{AB} (m^2/s) is the binary diffusion coefficient; M_A and M_B (kg/mol) are molecular weight of species A and B, respectively; σ_A (Å) denotes the characteristic length of

the Lennard-Jones/Stockmayer potential; Ω_D represents the collision integral and its full explanation can be found elsewhere.

Although energy balance equation has been excluded from the model due to the assumption of isothermal environment in the reaction chamber, thermodynamic data is still required to calculate the equilibrium constants for gas-phase elementary reactions. Here, polynomial expressions are used with input of seven coefficients (NASA format) of chemical species:

$$\frac{C_p^0}{R_g} = a_1 + a_2 T + a_3 T^2 + a_4 T^3 + a_5 T^4 \qquad \text{(Eqn. B.1.6)}$$

$$\frac{H^0}{R_g T} = a_1 + \frac{a_2}{2} T + \frac{a_3}{3} T^2 + \frac{a_4}{4} T^3 + \frac{a_5}{5} T^4 + \frac{a_6}{T} \qquad \text{(Eqn. B.1.7)}$$

$$\frac{S^0}{R_g} = a_1 lnT + a_2 T + \frac{a_3}{2} T^2 + \frac{a_4}{3} T^3 + \frac{a_5}{4} T^4 + a_7 \qquad \text{(Eqn. B.1.8)}$$

Where C_p^0 (J/(mol·K)) denotes heat capacity at constant pressure; H^0 (J/mol) is molar enthalpy of the species; S^0 (J/(mol·K)) denotes molar entropy of chemical species. The superscript 0 refers to the standard state. For gas-phase species, the standard state is the ideal gas at 1 atmosphere. a_i (i = 1, 2 … 7) are polynomial coefficients in NASA thermodynamic database.

B.2 GAS-PHASE CHEMISTRY

In general, a gas-phase reaction system can be described as

$$\sum_{k=1}^{K_g} \upsilon_{ki}^{'} X_k \rightleftharpoons \sum_{k=1}^{K_g} \upsilon_{ki}^{''} X_k \qquad \left(i = 1, \ldots, N_g\right) \qquad \text{(Eqn. B.2.1)}$$

In equation 9, gas-phase chemical species are indexed by k, with K_g is the total number of gas-phase chemical species; elementary reactions are indexed by i, with N_g the total number of gas-phase reactions in the mechanism; the name of species k are represented by X_k; $\upsilon_{ki}^{'}$ and $\upsilon_{ki}^{''}$ are the stoichiometric coefficients of species k in the forward and reverse direction of reaction i, respectively.

The "rate of progress" of reaction i can be expressed as q_i (mol/(m^3·s)) below

$$q_i = k_{f,i} \prod_{k=1}^{K_g} \left[X_k\right]^{\upsilon_{ki}^{'}} - k_{r,i} \prod_{k=1}^{K_g} \left[X_k\right]^{\upsilon_{ki}^{''}} \qquad \text{(Eqn. B.2.2)}$$

where $k_{f,i}$ and $k_{r,i}$ are the reaction rate constants for the forward and reverse direction of reaction step i, respectively, and $\left[X_k\right]$ (mol/m^3) is the concentration of species k. Reaction rate constants can be written is a modified three-parameter Arrhenius form

$$k_{f,i} = A_f T^{\beta} \exp\left(-\frac{E_f}{R_g T}\right) \qquad \text{(Eqn. B.2.3)}$$

where A_f denotes pre-exponential factor for the forward direction of reaction i; E_f is the activation energy (J/mol) for the forward direction of reaction i; β represents the dependence factor with respect to temperature. The reverse direction of reaction i can be expressed in exactly the same way.

For elementary reaction steps that include third-body effect, the rate-of-progress q_i needs to be modified by multiplying a third-body concentration

$$q_i^{'} = \left(\sum_{k=1}^{K_g} \alpha_{k,i} [X_k] \right) \left(k_{f,i} \prod_{k=1}^{K_g} [X_k]^{\upsilon_{ki}^{'}} - k_{r,i} \prod_{k=1}^{K_g} [X_k]^{\upsilon_{ki}^{''}} \right) \quad \text{(Eqn. B.2.4)}$$

where $\alpha_{k,i}$ is the third-body efficiency factor for species k in reaction step i.

The net production or consumption rate $\dot{\omega}_k$ (mol/(m^3·s)) of species k can be expressed as

$$\dot{\omega}_k = \sum_{i=1}^{N_g} \upsilon_{ki} q_i \quad \text{(Eqn. B.2.5)}$$

which includes the contribution of all reaction steps in the mechanism. υ_{ki} is the difference of stoichiometric coefficients of species k between the both directions in reaction step i and it can be written as

$$\upsilon_{ki} = \upsilon_{ki}^{''} - \upsilon_{ki}^{'} \quad \text{(Eqn. B.2.6)}$$

The reaction rate constants of several reverse direction steps are calculated by using equilibrium constant given by

$$K_{p,i}^0 = \exp\left(\frac{\Delta S_{r,i}^0}{R_g} - \frac{H_{r,i}^0}{R_g T} \right) \quad \text{(Eqn. B.2.7)}$$

where $\Delta S_{r,i}^0$ (J/(mol·K)) and $H_{r,i}^0$ (J/mol) are the net change in entropy and enthalpy of reaction step i given by

$$\Delta S_{r,i}^0 = \sum_{k=1}^{K} \upsilon_{ki} S_k^0 \quad \text{(Eqn. B.2.8)}$$

$$\Delta H_{r,i}^0 = \sum_{k=1}^{K} \upsilon_{ki} H_k^0 \quad \text{(Eqn. B.2.9)}$$

Finally, the reverse reaction rate constant can be calculated by

$$k_j^r = \frac{k_j^f}{K_{0,j}^{eq}} \qquad \text{(Eqn. B.2.10)}$$

B.3 SURFACE CHEMISTRY

Surface chemistry consists of three basic steps in this model: adsorption, surface reaction, and desorption. Considering a surface reaction mechanism consists of N_s (reversible or irreversible) elementary reaction steps with K_g gas-phase and K_s surface species, respectively, which can be represented in the general form:

$$\sum_{k=1}^{K_g+K_s} \upsilon_{ki}^{'} X_k \rightleftharpoons \sum_{k=1}^{K_g+K_s} \upsilon_{ki}^{"} X_k \qquad \left(i = 1,\ldots,N_s\right) \qquad \text{(Eqn. B.3.1)}$$

The rate of progress q_i (mol/(m^2·s)) is defined as

$$q_i = k_{f,i} \prod_{k=1}^{K_g+K_s} \left[X_k\right]^{\upsilon_{ki}^{'}} - k_{r,i} \prod_{k=1}^{K_g+K_s} \left[X_k\right]^{\upsilon_{ki}^{"}} \qquad \text{(Eqn. B.3.2)}$$

Molar production rate $\dot{s}_k$ (mol/(m^2·s)) of gas-phase and surface species are given by

$$\dot{s}_k = \sum_{i=1}^{N_s} \upsilon_{ki} q_i \qquad (k = 1,\ldots,K_g + K_s) \qquad \text{(Eqn. B.3.3)}$$

For the adsorption step, the following equation is applied to convert stick coefficient to reaction rate constant

$$k_{ads,i} = \frac{\gamma_k}{(\Gamma_{tot})^m} \sqrt{\frac{R_g T}{2\pi M_k}} \qquad \text{(Eqn. B.3.4)}$$

where $k_{ads,i}$ is the rate constant of catalytic reaction step i; γ_k is the sticking coefficient of species k; Γ_{tot} (mol/m^2) is the density of active site; m is the reaction order; M_k (kg/mol) is the molecular weight of the gas-phase species k involved in the adsorption process.

Also, surface reactions lead to the following boundary condition at the gas-solid interface

$$j_k = F_{catgeo}\, \dot{s}_k\, M_k \qquad (k = 1,\ldots,N_g) \qquad \text{(Eqn. B.3.5)}$$

where j_k (kg/(m^2·s)) is the normal component of diffusive flux of species k at the interface; F_{catgeo} is the ratio between active catalytic surface area and geometric surface area, which is set to 20 due to the porous structure in the La_2O_3-based thin-film catalyst.

In the transient mode, on the catalytic surface, molar production rate $\dot{s}_k$ (mol/(m^2·s)) of surface species can be used to calculate their corresponding concentration $[X_k]$ (mol/m^2) by

$$\frac{\partial [X_k]}{\partial t} = \dot{s}_k \qquad (k = N_g + 1,\ldots,N_g + N_s) \qquad \text{(Eqn. B.3.6)}$$

Finally, the concentration of free site $[X_{site}]$ can be calculate based on the conservation of active site on the surface

$$[X_{site}] = 1 - \sum_{k=N_g+1}^{k=N_g+N_s} [X_k] \qquad \text{(Eqn. B.3.7)}$$

Surface site density Γ_{tot}, as well as sticking coefficients γ are treated as constants in this work.

APPENDIX C

MICROKINETICS FOR OXIDATIVE COUPLING OF METHANE

C.1 GAS-PHASE REACTION MECHIANSM FOR OCM

Table 1. Elementary reaction steps in the gas phase in the oxidative coupling of methane (OCM) and corresponding parameter values [50]

Reaction		A (s^{-1}or $m^3mol^{-1}s^{-1}$ or $m^6mol^{-2}s^{-1}$)	Ea ($kJmol^{-1}$)
$CH_4 + O_2 = CH_3• + HO_2•$	(1)	0.983×10^{07}	193.86
$CH_4 + H• = CH_3• + H_2$	(2)	0.234×10^{09}	51.17
$CH_4 + O• = CH_3• + OH•$	(3)	0.127×10^{10}	33.83
$CH_4 + OH• = CH_3• + H_2O$	(4)	0.743×10^{09}	41.43
$CH_4 + HO_2• = CH_3• + H_2O_2$	(5)	0.401×10^{08}	99.61
$CH_3• + O_2 = CH_3O• + O•$	(6)	0.308×10^{09}	141.00
$CH_3• + O_2 = CH_2O + OH•$	(7)	0.459×10^{08}	103.66
$CH_3• + HO_2• = CH_3O• + OH•$	(8)	0.885×10^{08}	0.00
$CH_3• + CH_3• + M = C_2H_6 + M$	(9)	0.650×10^{08}	0.00
$CH_3O• + M = CH_2O + H• + M$	(10)	0.258×10^{15}	115.00
$CH_2O + OH• = CHO• + H_2O$	(11)	0.580×10^{09}	5.00
$CH_2O + HO_2• = CHO• + H_2O_2$	(12)	0.417×10^{07}	40.12
$CH_2O + CH_3• = CHO• + CH_4$	(13)	0.700×10^{08}	25.03
$CHO• + M = CO + H• + M$	(14)	0.280×10^{10}	64.36
$CHO• + O_2 = CO + HO_2•$	(15)	0.171×10^{06}	0.00
$CO + HO_2• = CO_2 + OH•$	(16)	0.308×10^{09}	107.34
$C_2H_6 + H• = C_2H_5• + H_2$	(17)	0.910×10^{09}	51.70
$C_2H_6 + OH• = C_2H_5• + H_2O$	(18)	0.545×10^{09}	17.16
$C_2H_6 + CH_3• = C_2H_5• + CH_4$	(19)	0.239×10^{08}	64.73
$C_2H_5• + HO_2• = CH_3• + CH_2O + OH•$	(20)	0.948×10^{07}	0.00

Table 1 (continued)

$C_2H_5• + M = C_2H_4 + H• + M$	(21)	0.596×10^{14}	167.66
$C_2H_5• + O_2 = C_2H_4 + HO_2•$	(22)	0.635×10^{07}	53.20
$C_2H_4 + O_2 = C_2H_3• + HO_2•$	(23)	0.281×10^{07}	144.55
$C_2H_4 + H• = C_2H_3• + H_2$	(24)	0.150×10^{09}	42.70
$C_2H_4 + OH• = C_2H_3• + H_2O$	(25)	0.612×10^{08}	24.70
$C_2H_4 + CH_3• = C_2H_3• + CH_4$	(26)	0.199×10^{06}	51.46
$C_2H_4 + OH• = CH_3• + CH_2O$	(27)	0.272×10^{07}	0.00
$C_2H_3• + M = C_2H_2 + H• + M$	(28)	0.121×10^{16}	176.44
$C_2H_3• + O_2 = C_2H_2 + HO_2•$	(29)	0.500×10^{07}	0.00
$C_2H_3• + O_2 = CH_2O + CHO•$	(30)	0.550×10^{07}	0.00
$C_2H_5• + CH_3• = C_3H_8$	(31)	0.800×10^{07}	0.00
$C_3H_8 + H• = C_3H_7•+ H_2$	(32)	0.900×10^{09}	32.00
$C_2H_4 + CH_3• = C_3H_7•$	(33)	0.300×10^{06}	29.00
$C_3H_7• = C_3H_6 + H•$	(34)	0.150×10^{16}	156.00
$O_2 + H• = OH• + O•$	(35)	0.220×10^{09}	70.30
$O_2 + H• + M = HO_2• + M$	(36)	0.139×10^{06}	0.00
$HO_2• + HO_2• = O_2 + OH• + OH•$	(37)	0.200×10^{07}	0.00
$H_2O_2 + M = OH• + OH• + M$	(38)	0.127×10^{12}	199.36
$C_2H_6 = C_2H_5• + H•$	(39)	0.400×10^{17}	378.51

(•) means that the species belong to free radical species.

With the third body efficiencies [51]

M	H_2O/6.5/	O_2/0.4/	CO/0.75/	CO_2/1.5/

C.2 CATALYTIC REACTION MECHANISM FOR OCM

Table 2. Catalytic elementary reaction steps in the oxidative coupling of methane (OCM) and corresponding parameter values for La–Sr/CaO catalyst [27]

Elementary Reaction		A^f or S_0	E_a^f	A^b or S_0	E_a^b
$O_2 + 2* \leftrightarrow 2O_{(s)}$	(40)	0.40	0.0	2.39×10^{15}	110.7
$CH_4 + O_{(s)} \leftrightarrow CH_3• + OH_{(s)}$	(41)	1.85×10^{07}	146.4	1.91×10^{07}	85.0
$C_2H_4 + O_{(s)} \leftrightarrow C_2H_3• + OH_{(s)}$	(42)	1.40×10^{07}	131.4	1.42×10^{07}	90.1
$C_2H_6 + O_{(s)} \leftrightarrow C_2H_5• + OH_{(s)}$	(43)	1.35×10^{07}	166.2	1.37×10^{07}	78.5
$2OH_{(s)} \leftrightarrow H_2O_{(s)} + O_{(s)}$	(44)	2.25×10^{15}	190.3	2.17×10^{15}	98.2

Table 2 (continued)

$H_2O_{(s)} \leftrightarrow H_2O + *$	(45)	2.10×10^{13}	54.2	0.52	0.0
$CH_3\bullet + O_{(s)} \leftrightarrow CH_3O_{(s)}$	(46)	3.30×10^{-5}	0.0	2.24×10^{13}	244.6
$CH_3O_{(s)} + O_{(s)} \leftrightarrow CH_2O_{(s)} + OH_{(s)}$	(47)	1.72×10^{15}	0.0	1.69×10^{15}	155.9
$CH_2O_{(s)} + O_{(s)} \leftrightarrow CHO_{(s)} + OH_{(s)}$	(48)	1.69×10^{15}	35.1	1.75×10^{15}	112.6
$CHO_{(s)} + O_{(s)} \leftrightarrow CO_{(s)} + OH_{(s)}$	(49)	1.72×10^{15}	14.7	1.81×10^{15}	133.9
$CO_{(s)} + O_{(s)} \leftrightarrow CO_{2(s)} + *$	(50)	1.81×10^{15}	0.0	1.39×10^{15}	205.3
$CO + * \leftrightarrow CO_{(s)}$	(51)	2.70×10^{-4}	0.0	1.81×10^{13}	101.4
$CO_2 + * \leftrightarrow CO_{2(s)}$	(52)	1.30×10^{-2}	0.0	1.07×10^{13}	160.9

(*) represents the active site on the surface; the subscript (s) in the formula denotes the species belongs to surface species. Units: A, $m^3mol^{-1}s^{-1}$ $((41)^{f+b}$, $(42)^{f+b}$, $(43)^{f+b}$, $(45)^{b}$, $(46)^{f}$, $(51)^{f}$, $(52)^{f})$; $m^2mol^{-1}s^{-1}$ $((40)^{b}$, $(44)^{f+b}$, $(47)^{f+b}$, $(48)^{f+b}$, $(49)^{f+b}$, $(50)^{f+b})$; $m^5mol^{-2}s^{-1}$ $(40)^{f}$; s^{-1} $((45)^{f}$, $(46)^{b}$, $(51)^{b}$, $(52)^{b})$. Ea, $kJmol^{-1}$.

APPENDIX D

TECHNICAL DRAWINGS OF THE MICROCHEMICAL REACTOR SYSTEM

D.1 DRAWINGS OF THE MAIN MICROCHEMCIAL REACTOR

The main microreactor
(Multiple actual views)

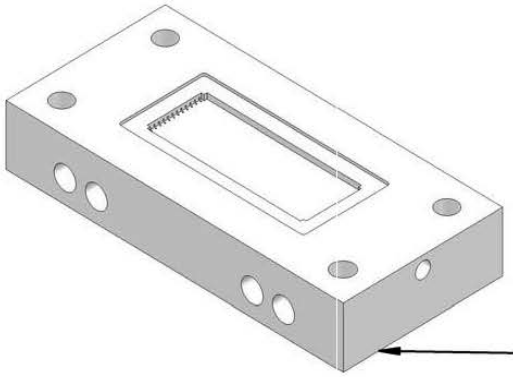

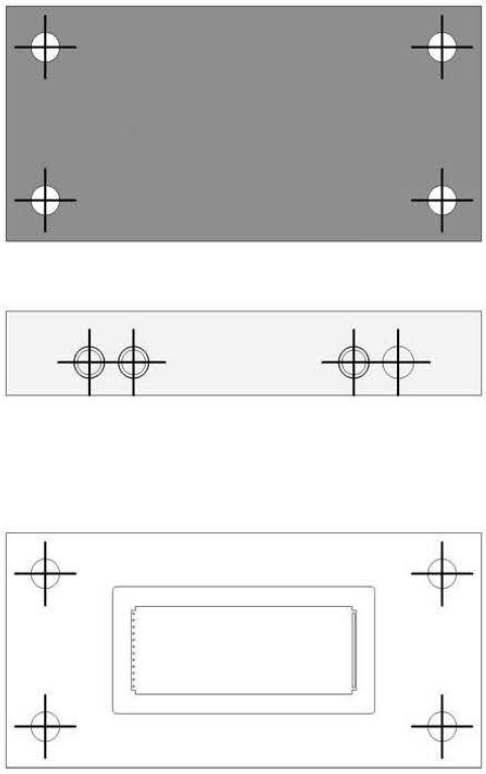

Compared with previous version (first version), several things have been changed:
1) Modify the reaction chamber geometry to better fit silicon chips.
2) Replace outlet microchannel arrays by a rectangualr groove to avoid backmixing.
3) Add one more detection channel with a smaller slope.

		DIMENSIONS ARE IN INCHES TOLERANCES: FRACTIONAL ± ANGULAR: MACH ± BEND ± TWO PLACE DECIMAL ± THREE PLACE DECIMAL ±		NAME	DATE
			DRAWN	Sen Liu	11/16/2010
			CHECKED		
			ENG APPR.		
			MFG APPR.		
		MATERIAL MACOR	Q.A.		
			COMMENTS:		
NEXT ASSY	USED ON	FINISH --			
Microreactor		DO NOT SCALE DRAWING			

PROPRIETARY AND CONFIDENTIAL
THE INFORMATION CONTAINED IN THIS DRAWING IS THE SOLE PROPERTY OF <INSERT COMPANY NAME HERE>. ANY REPRODUCTION IN PART OR AS A WHOLE WITHOUT THE WRITTEN PERMISSION OF <INSERT COMPANY NAME HERE> IS PROHIBITED.

Univ. of Pitt.

Microreactor

SIZE	DWG. NO.	REV.
A		
SCALE:1:1	WEIGHT:	SHEET 1 OF 10

The main microreactor
(Multiple views with hidden lines)

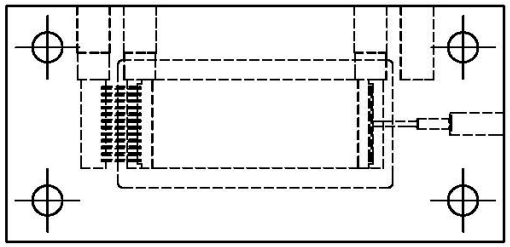

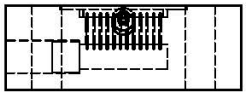

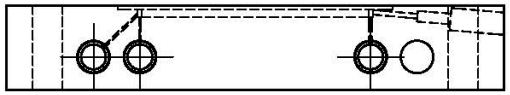

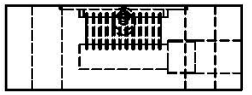

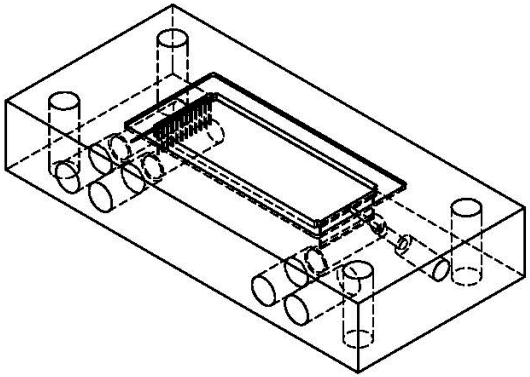

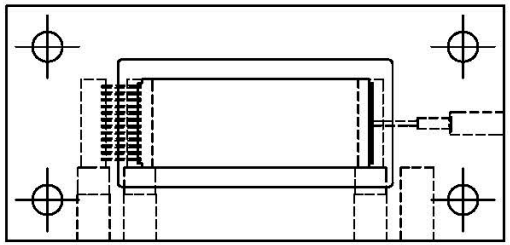

NEXT ASSY	USED ON
Microreactor	

DIMENSIONS ARE IN INCHES
TOLERANCES:
FRACTIONAL ±
ANGULAR: MACH ± BEND ±
TWO PLACE DECIMAL ±
THREE PLACE DECIMAL ±

MATERIAL MACOR

FINISH —

DO NOT SCALE DRAWING

	NAME	DATE
DRAWN	Sen Liu	11/16/2010
CHECKED		
ENG APPR.		
MFG APPR.		
Q.A.		

COMMENTS:

Univ. of Pitt.

Microreactor

SIZE	DWG. NO.	REV.
A		
SCALE:1:1	WEIGHT:	SHEET 2 OF 10

The main microreactor
(Top view with dimensions)

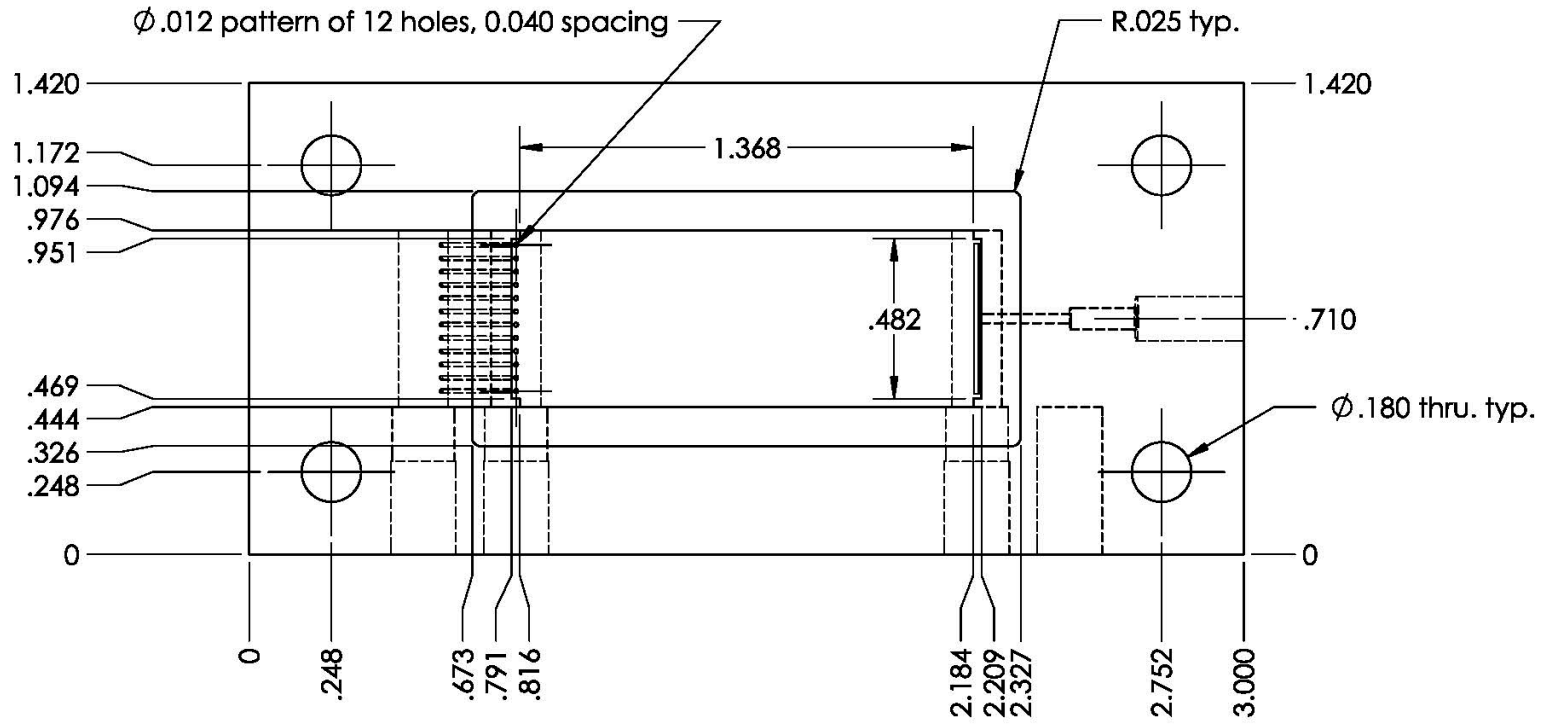

		DIMENSIONS ARE IN INCHES TOLERANCES: FRACTIONAL ± ANGULAR: MACH ± BEND ± TWO PLACE DECIMAL ± THREE PLACE DECIMAL ±		NAME	DATE
			DRAWN	Sen Liu	04/11/2010
			CHECKED		
			ENG APPR.		
			MFG APPR.		
		MATERIAL MACOR	Q.A.		
NEXT ASSY	USED ON	FINISH —	COMMENTS:		
Microreactor		DO NOT SCALE DRAWING			

PROPRIETARY AND CONFIDENTIAL
THE INFORMATION CONTAINED IN THIS DRAWING IS THE SOLE PROPERTY OF <INSERT COMPANY NAME HERE>. ANY REPRODUCTION IN PART OR AS A WHOLE WITHOUT THE WRITTEN PERMISSION OF <INSERT COMPANY NAME HERE> IS PROHIBITED.

Univ. of Pitt.

Microreactor

SIZE	DWG. NO.	REV.
A		
SCALE:1:1	WEIGHT:	SHEET 3 OF 10

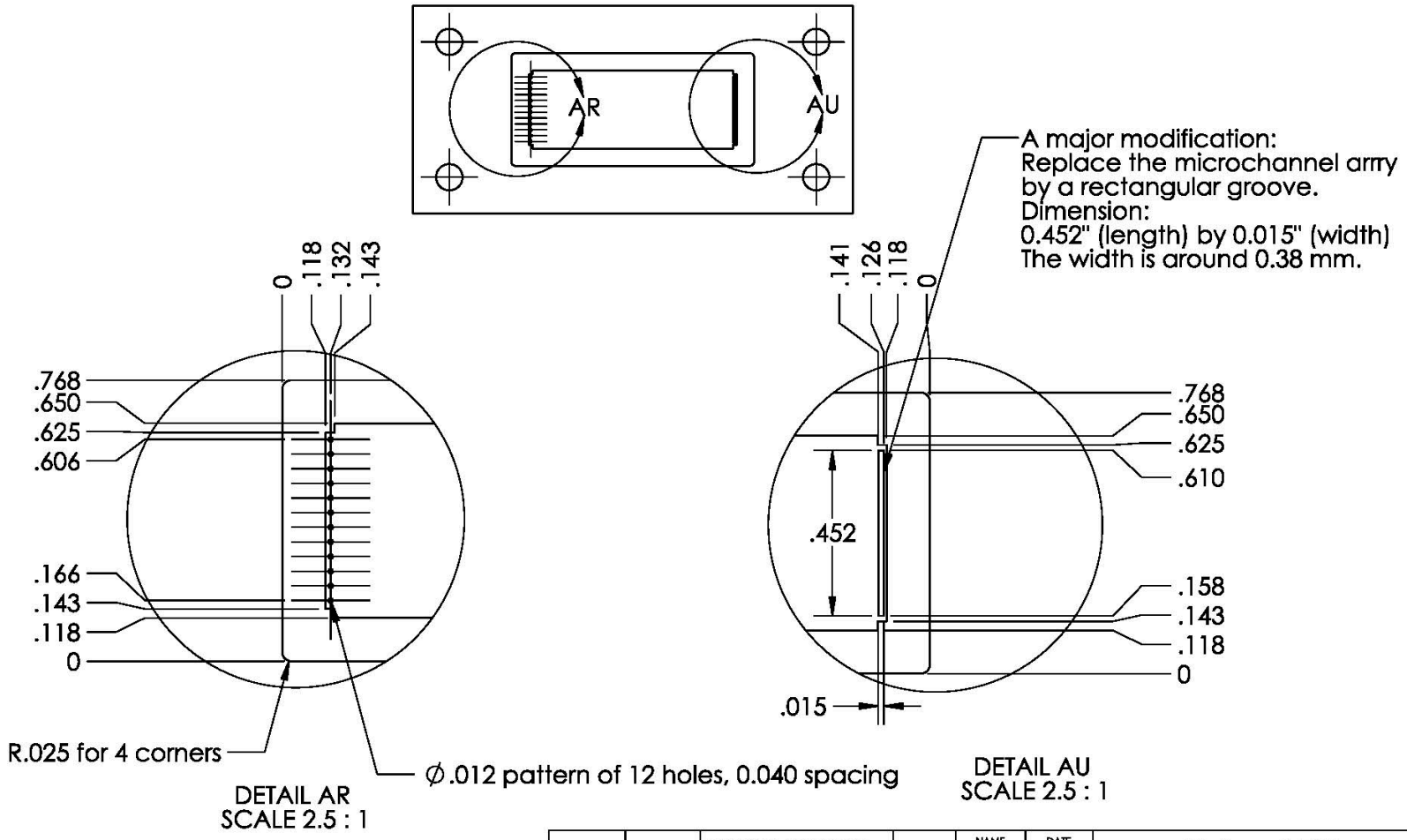

		DIMENSIONS ARE IN INCHES TOLERANCES: FRACTIONAL ± ANGULAR: MACH ± BEND ± TWO PLACE DECIMAL ± THREE PLACE DECIMAL ±		NAME	DATE
			DRAWN	Sen Liu	03/24/2010
			CHECKED		
			ENG APPR.		
			MFG APPR.		
			Q.A.		
		MATERIAL RA330	COMMENTS:		
NEXT ASSY	USED ON	FINISH —			
Microreactor		DO NOT SCALE DRAWING			

Univ. of Pitt.

Top Plate

SIZE	DWG. NO.	REV.
A		
SCALE:1:1	WEIGHT:	SHEET 4 OF 10

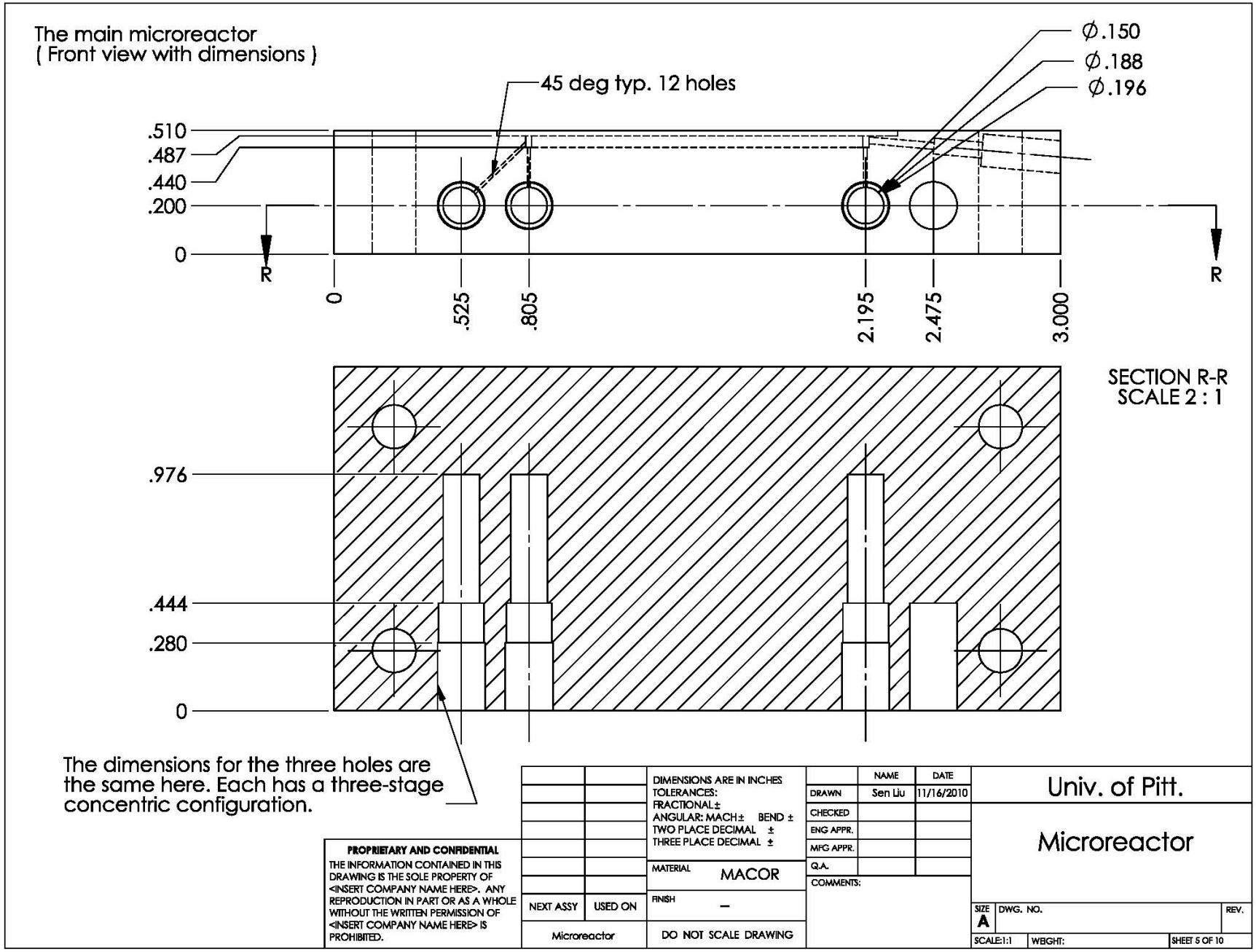
The main microreactor
(Front view with dimensions)
45 deg typ. 12 holes
Ø.150
Ø.188
Ø.196
.510
.487
.440
.200
0
R
R
0
.525
.805
2.195
2.475
3.000
SECTION R-R
SCALE 2 : 1
.976
.444
.280
0
The dimensions for the three holes are the same here. Each has a three-stage concentric configuration.
PROPRIETARY AND CONFIDENTIAL
THE INFORMATION CONTAINED IN THIS DRAWING IS THE SOLE PROPERTY OF <INSERT COMPANY NAME HERE>. ANY REPRODUCTION IN PART OR AS A WHOLE WITHOUT THE WRITTEN PERMISSION OF <INSERT COMPANY NAME HERE> IS PROHIBITED.
NEXT ASSY
USED ON
Microreactor
DIMENSIONS ARE IN INCHES
TOLERANCES:
FRACTIONAL ±
ANGULAR: MACH ± BEND ±
TWO PLACE DECIMAL ±
THREE PLACE DECIMAL ±
MATERIAL MACOR
FINISH —
DO NOT SCALE DRAWING
NAME
DATE
DRAWN Sen Liu 11/16/2010
CHECKED
ENG APPR.
MFG APPR.
Q.A.
COMMENTS:
Univ. of Pitt.
Microreactor
SIZE A
DWG. NO.
REV.
SCALE:1:1
WEIGHT:
SHEET 5 OF 10

The main microreactor
(Section view with dimensions)

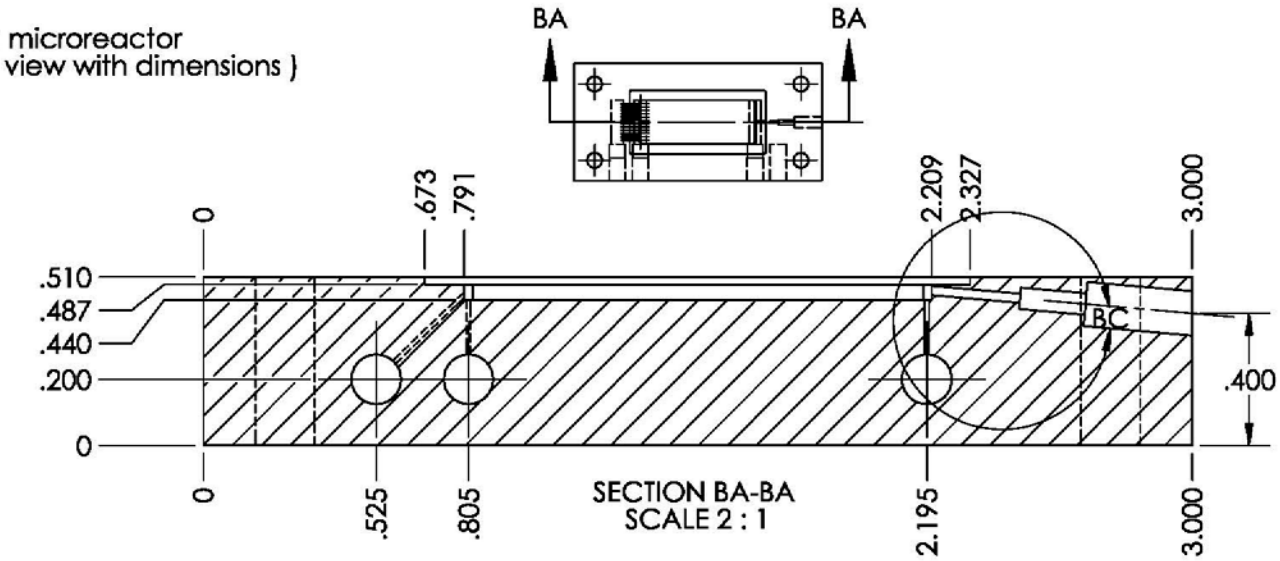

SECTION BA-BA
SCALE 2 : 1

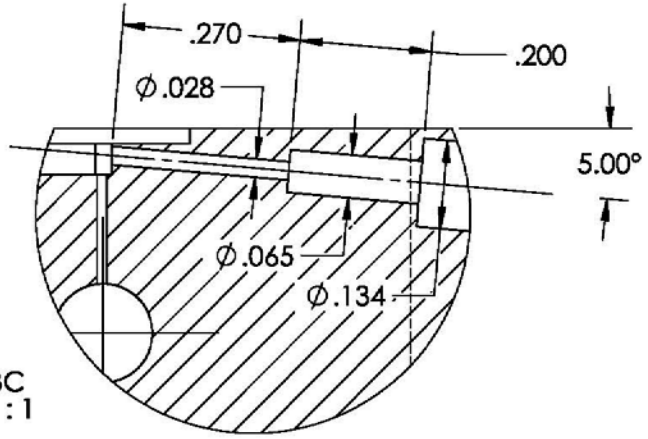

DETAIL BC
SCALE 4 : 1

		DIMENSIONS ARE IN INCHES TOLERANCES: FRACTIONAL ± ANGULAR: MACH ± BEND ± TWO PLACE DECIMAL ± THREE PLACE DECIMAL ±		NAME	DATE	Univ. of Pitt.
			DRAWN	Sen Liu	11/16/2010	
			CHECKED			Microreactor
			ENG APPR.			
			MFG APPR.			
		MATERIAL MACOR	Q.A.			
NEXT ASSY	USED ON	FINISH —	COMMENTS:			SIZE A / DWG. NO. / REV.
Microreactor		DO NOT SCALE DRAWING				SCALE:1:1 / WEIGHT: / SHEET 6 OF 10

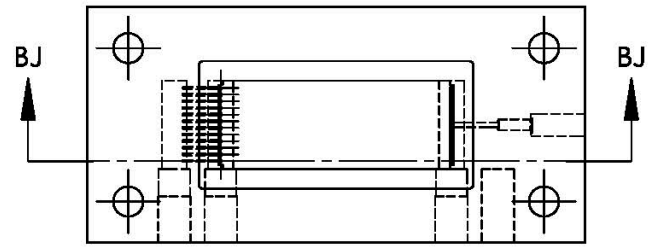

SECTION BJ-BJ

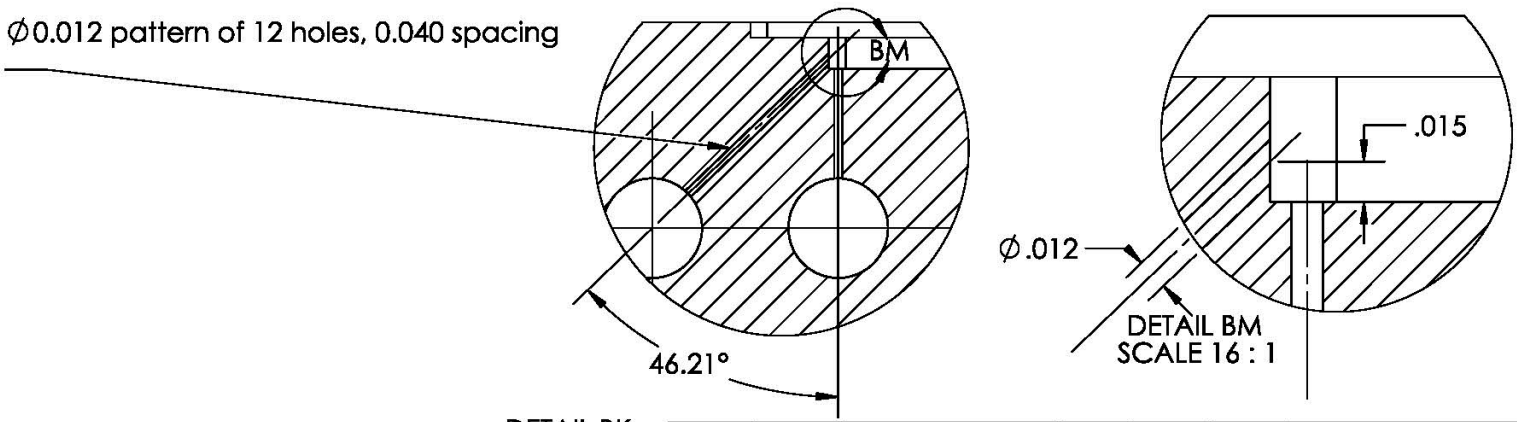

DETAIL BK
SCALE 4 : 1

		DIMENSIONS ARE IN INCHES TOLERANCES: FRACTIONAL ± ANGULAR: MACH ± BEND ± TWO PLACE DECIMAL ± THREE PLACE DECIMAL ±		NAME	DATE
			DRAWN	Sen Liu	03/24/2010
			CHECKED		
			ENG APPR.		
			MFG APPR.		
			Q.A.		
			COMMENTS:		
		MATERIAL RA330			
NEXT ASSY	USED ON	FINISH —			
Microreactor		DO NOT SCALE DRAWING			

Univ. of Pitt.

Top Plate

SIZE	DWG. NO.	REV.
A		
SCALE:1:1	WEIGHT:	SHEET 7 OF 10

D.2 DRAWINGS OF LEFT AND RIGHT ELBOWS

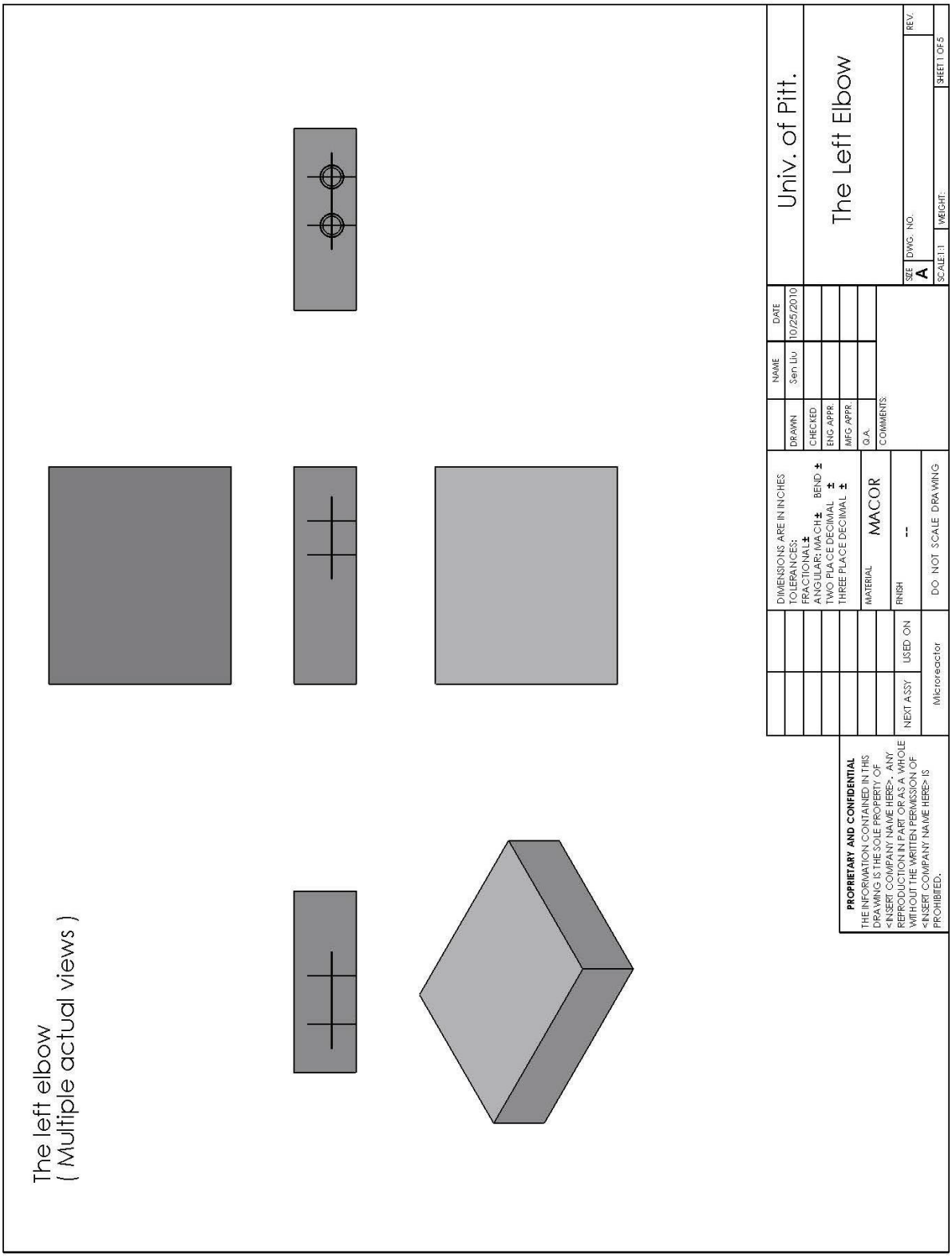

The Left Elbow
(Multiple views with hidden lines)

Since the left elbow has two connecting systems, just define the longer one as the outer connecting system, while the short one as inner connecting system, for differenting between the two.

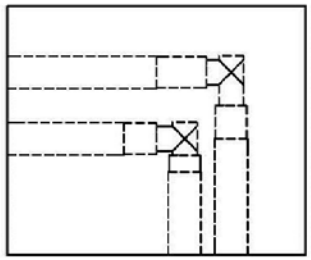

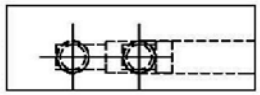

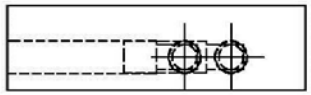

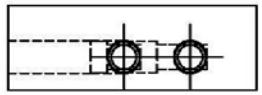

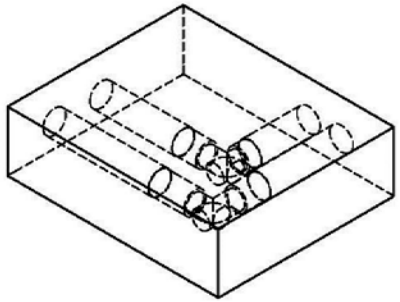

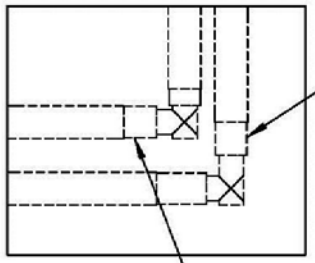

Compared with the design for last version, the major difference for the current design is to reduce the length of the fixing channel (the one with the diameter of 0.188") so as to increase the length of bonding channel (diameter of 0.196")

NEXT ASSY	USED ON
Microreactor	

DIMENSIONS ARE IN INCHES
TOLERANCES:
FRACTIONAL ±
ANGULAR: MACH ± BEND ±
TWO PLACE DECIMAL ±
THREE PLACE DECIMAL ±

MATERIAL MACOR

FINISH —

DO NOT SCALE DRAWING

	NAME	DATE
DRAWN	Sen Liu	10/25/2010
CHECKED		
ENG APPR.		
MFG APPR.		
Q.A.		

COMMENTS:

Univ. of Pitt.

The Left Elbow

SIZE A | DWG. NO. | REV.

SCALE:1:1 | WEIGHT: | SHEET 2 OF 6

The Left Elbow
(Standard 3 view and detail view)

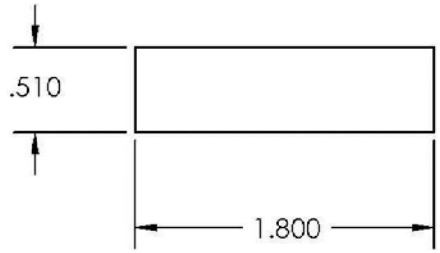

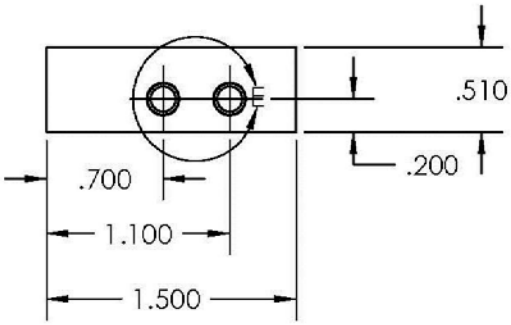

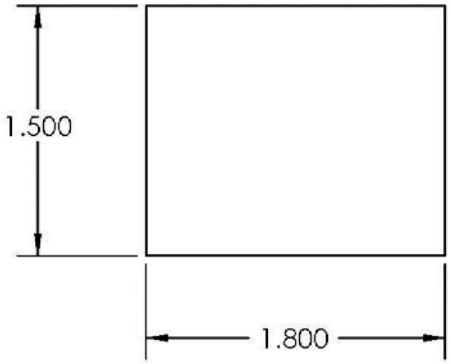

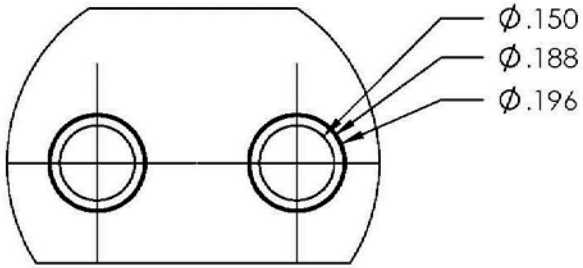

DETAIL E
DETAIL 3 : 1

		DIMENSIONS ARE IN INCHES TOLERANCES: FRACTIONAL ± ANGULAR: MACH ± BEND ± TWO PLACE DECIMAL ± THREE PLACE DECIMAL ±		NAME	DATE
			DRAWN	Sen Liu	10/25/2010
			CHECKED		
			ENG APPR.		
			MFG APPR.		
			Q.A.		
			COMMENTS:		
NEXT ASSY	USED ON	MATERIAL MACOR FINISH —			
Microreactor		DO NOT SCALE DRAWING			

Univ. of Pitt.

The Left Elbow

SIZE	DWG. NO.	REV.
A		
SCALE:1:1	WEIGHT:	SHEET 3 OF 5

The Left Elbow
(Dimensions for the outer connecting system)

The inner and outer connecting systems in all, have four connecting interfaces with ceramic tubes, which have the same three-stage concentric configurations. The diameters are 0.196, 0.188 and 0.150, respectively, although the depth for each diameter is different. The dimensions for depth are annotated clearly in the design files.

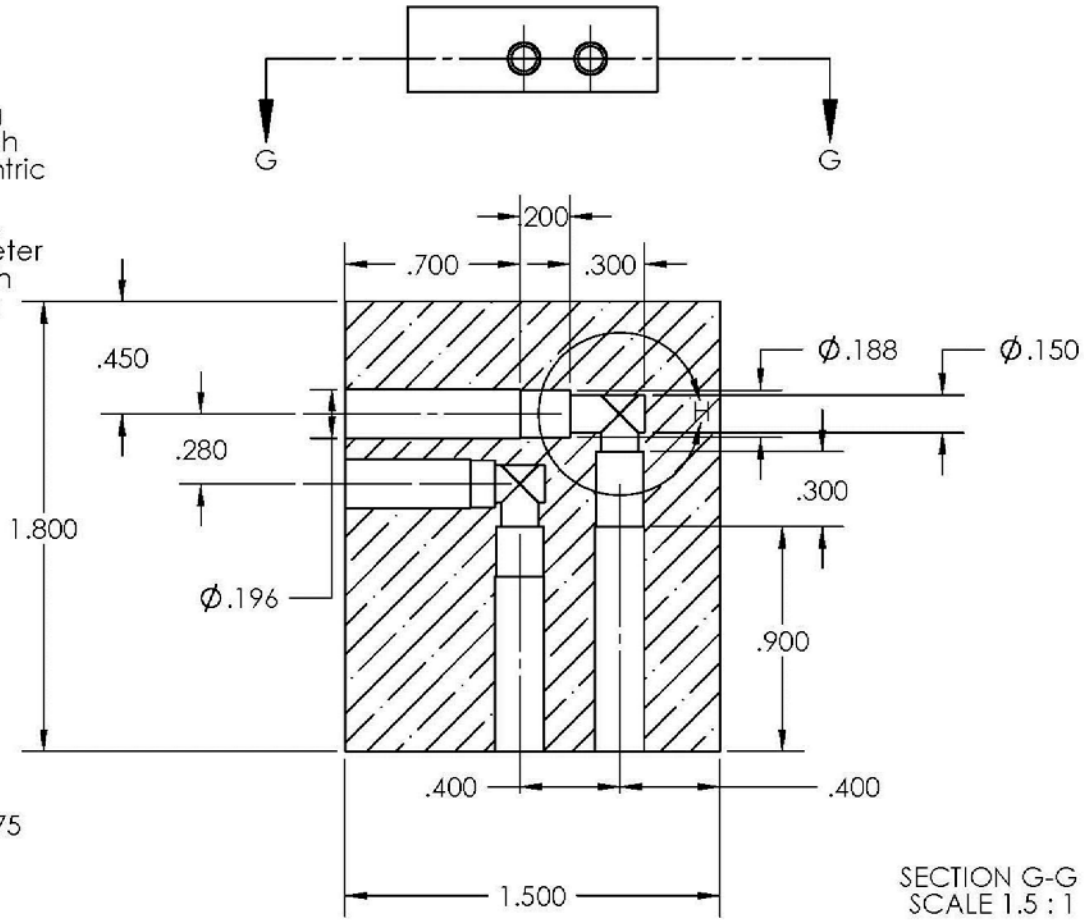

SECTION G-G
SCALE 1.5 : 1

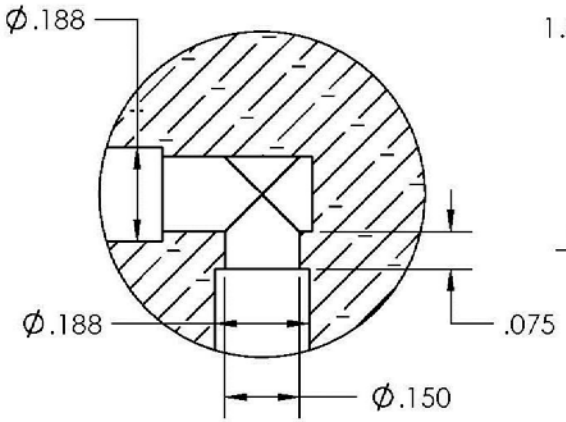

DETAIL H
SCALE 3 : 1

		DIMENSIONS ARE IN INCHES TOLERANCES: FRACTIONAL ± ANGULAR: MACH ± BEND ± TWO PLACE DECIMAL ± THREE PLACE DECIMAL ±		NAME / DATE
		MATERIAL MACOR	DRAWN	Sen Liu / 10/25/2010
		FINISH --	CHECKED	
			ENG APPR.	
NEXT ASSY	USED ON		MFG APPR.	
Microreactor		DO NOT SCALE DRAWING	Q.A.	
			COMMENTS:	

Univ. of Pitt.

The Left Elbow

SIZE	DWG. NO.	REV.
A		
SCALE:1:1	WEIGHT:	SHEET 4 OF 5

The Left Elbow
(Dimensions for the inner connecting system)

The inner and outer connecting systems in all, have four connecting interfaces with ceramic tubes, which have the same three-stage concentric configurations. The diameters are 0.196, 0.188 and 0.150, respectively, although the depth for each diameter is different. The dimensions for depth are annotated clearly in the design files.

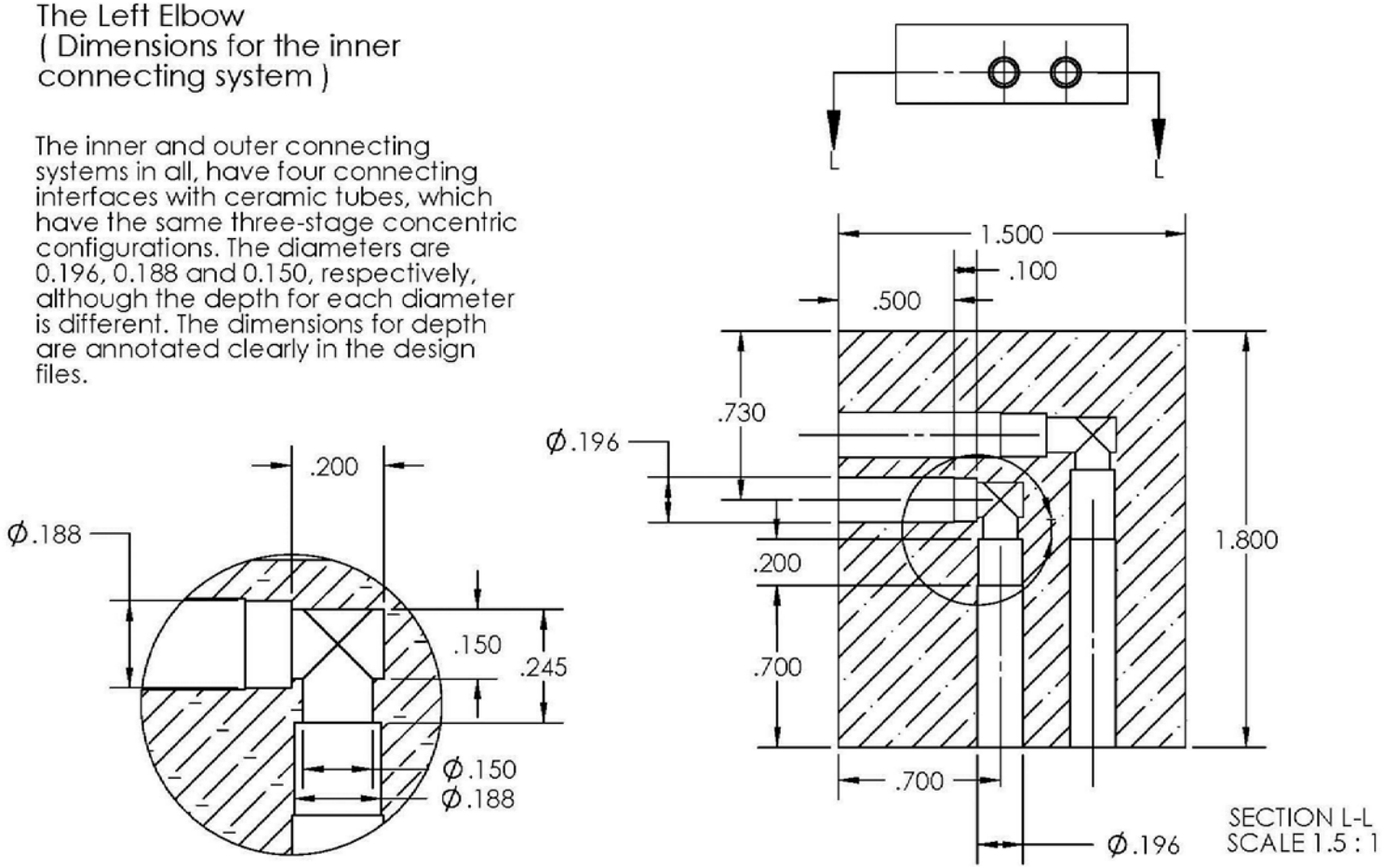

		DIMENSIONS ARE IN INCHES TOLERANCES: FRACTIONAL ± ANGULAR: MACH ± BEND ± TWO PLACE DECIMAL ± THREE PLACE DECIMAL ±		NAME	DATE
			DRAWN	Sen Liu	10/25/2010
			CHECKED		
			ENG APPR.		
			MFG APPR.		
			Q.A.		
		MATERIAL MACOR	COMMENTS:		
NEXT ASSY	USED ON	FINISH —			
Microreactor		DO NOT SCALE DRAWING			

Univ. of Pitt.

The Left Elbow

SIZE	DWG. NO.	REV.
A		
SCALE: 1:1	WEIGHT:	SHEET 6 OF 6

The Right Elbow
(Multiple Actual Views)

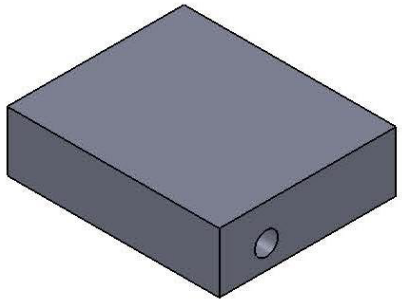

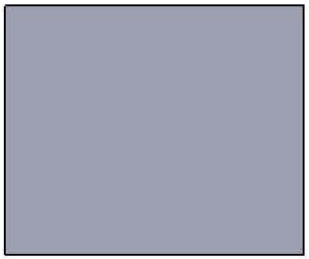

		DIMENSIONS ARE IN INCHES TOLERANCES: FRACTIONAL ± ANGULAR: MACH ± BEND ± TWO PLACE DECIMAL ± THREE PLACE DECIMAL ±		NAME	DATE
			DRAWN	Sen Liu	10/25/2010
			CHECKED		
			ENG APPR.		
			MFG APPR.		
		MATERIAL MACOR	Q.A.		
NEXT ASSY	USED ON	FINISH --	COMMENTS:		
Microreactor		DO NOT SCALE DRAWING			

PROPRIETARY AND CONFIDENTIAL

THE INFORMATION CONTAINED IN THIS DRAWING IS THE SOLE PROPERTY OF <INSERT COMPANY NAME HERE>. ANY REPRODUCTION IN PART OR AS A WHOLE WITHOUT THE WRITTEN PERMISSION OF <INSERT COMPANY NAME HERE> IS PROHIBITED.

Univ. of Pitt.

The Right Elbow

SIZE	DWG. NO.	REV.
A		
SCALE:1:1	WEIGHT:	SHEET 1 OF 4

The Right Elbow
(Multiple Views with hidden lines)

Compared with the design for previous version, the current design adds one more channel which allows both channels to connect to the main microreactor part, thus enchance the robustness of the whole system.

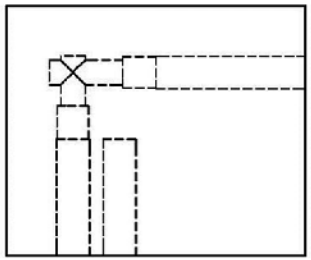

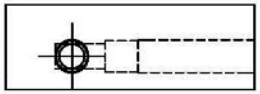

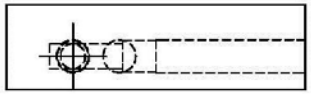

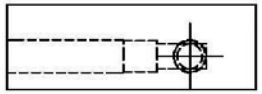

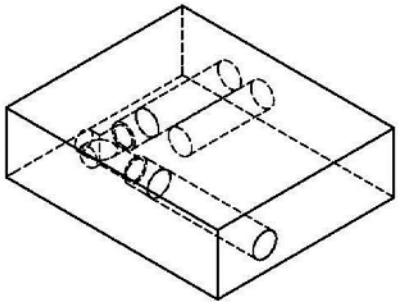

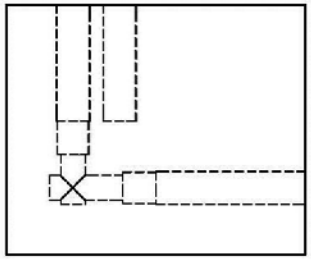

		DIMENSIONS ARE IN INCHES TOLERANCES: FRACTIONAL ± ANGULAR: MACH ± BEND ± TWO PLACE DECIMAL ± THREE PLACE DECIMAL ±		NAME	DATE
			DRAWN	Sen Liu	10/25/2010
			CHECKED		
			ENG APPR.		
			MFG APPR.		
			Q.A.		
		MATERIAL MACOR	COMMENTS:		
NEXT ASSY	USED ON	FINISH --			
Microreactor		DO NOT SCALE DRAWING			

PROPRIETARY AND CONFIDENTIAL

THE INFORMATION CONTAINED IN THIS DRAWING IS THE SOLE PROPERTY OF <INSERT COMPANY NAME HERE>. ANY REPRODUCTION IN PART OR AS A WHOLE WITHOUT THE WRITTEN PERMISSION OF <INSERT COMPANY NAME HERE> IS PROHIBITED.

Univ. of Pitt.

The Right Elbow

SIZE	DWG. NO.	REV.
A		
SCALE:1:1	WEIGHT:	SHEET 2 OF 4

The Right Elbow
(Standard 3 view)

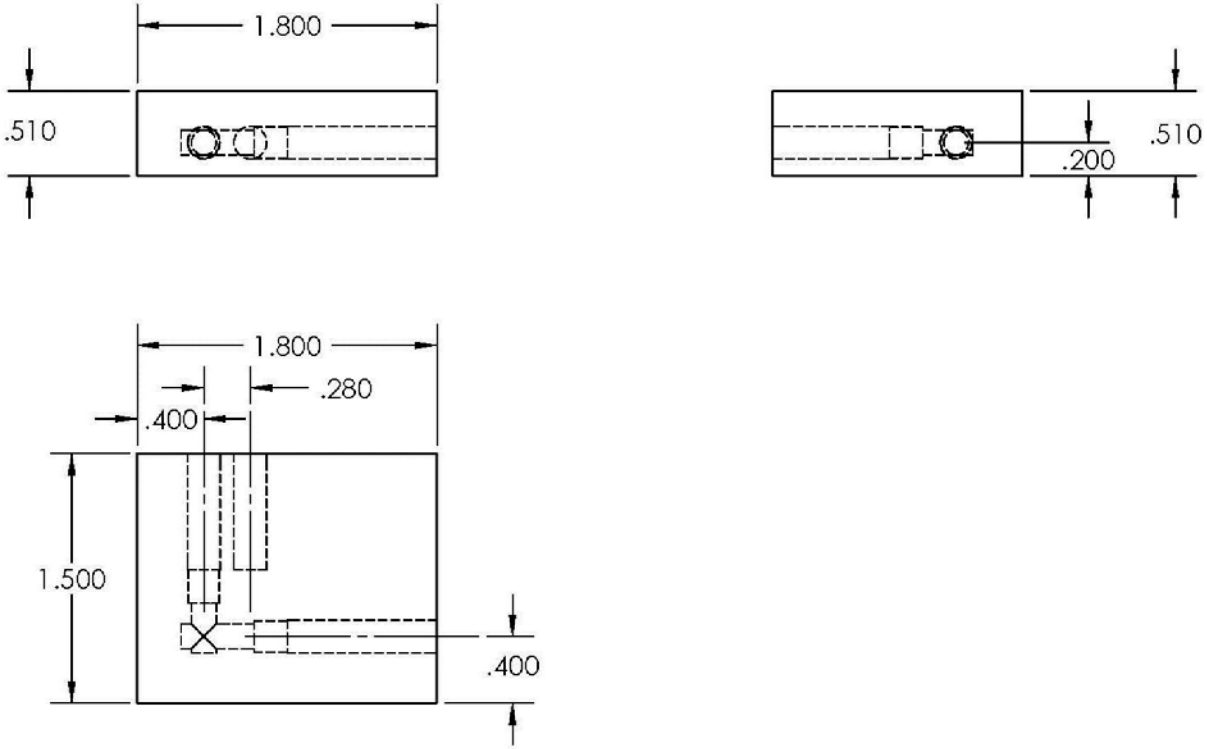

		DIMENSIONS ARE IN INCHES TOLERANCES: FRACTIONAL ± ANGULAR: MACH ± BEND ± TWO PLACE DECIMAL ± THREE PLACE DECIMAL ±		NAME	DATE
			DRAWN	Sen Liu	10/25/2010
			CHECKED		
			ENG APPR.		
			MFG APPR.		
		MATERIAL MACOR	Q.A.		
		FINISH —	COMMENTS:		
NEXT ASSY	USED ON	DO NOT SCALE DRAWING			
	Microreactor				

PROPRIETARY AND CONFIDENTIAL

THE INFORMATION CONTAINED IN THIS DRAWING IS THE SOLE PROPERTY OF <INSERT COMPANY NAME HERE>. ANY REPRODUCTION IN PART OR AS A WHOLE WITHOUT THE WRITTEN PERMISSION OF <INSERT COMPANY NAME HERE> IS PROHIBITED.

Univ. of Pitt.

The Right Elbow

SIZE	DWG. NO.	REV.
A		
SCALE:1:1	WEIGHT:	SHEET 3 OF 4

The Right Elbow
(Dimensions for the connecting system)

The connecting system in all, has two connecting interfaces with ceramic tubes, which have the same three-stage concentric configurations. The diameters are 0.196, 0.188 and 0.150, respectively, although the depth for each diameter is different. The dimensions for depth are annotated clearly in the design files.

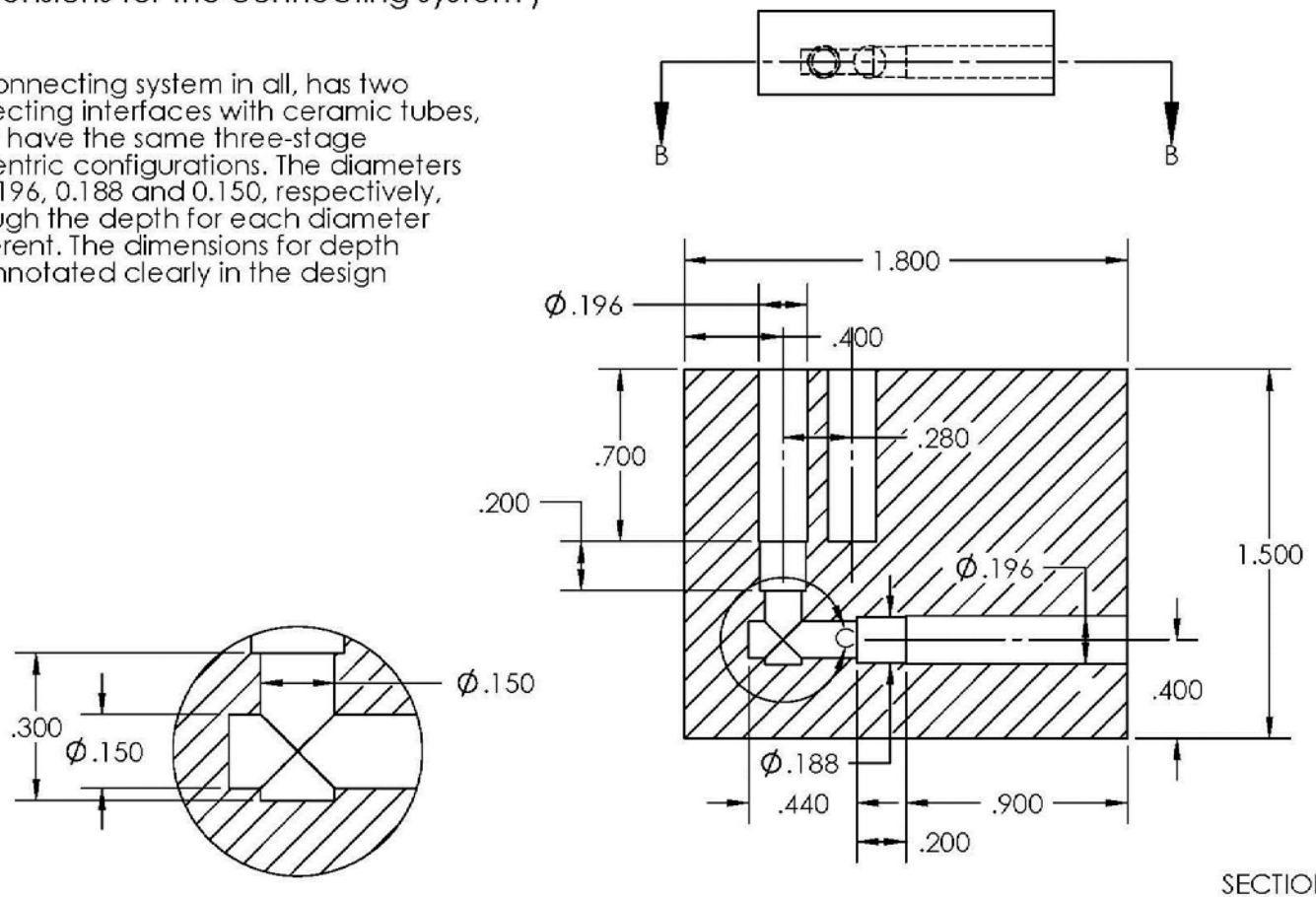

SECTION B-B
SCALE 1.5 : 1

DETAIL C
SCALE 3 : 1

		DIMENSIONS ARE IN INCHES TOLERANCES: FRACTIONAL ± ANGULAR: MACH ± BEND ± TWO PLACE DECIMAL ± THREE PLACE DECIMAL ±		NAME	DATE
			DRAWN	Sen Liu	10/25/2010
			CHECKED		
			ENG APPR.		
			MFG APPR.		
		MATERIAL MACOR	Q.A.		
			COMMENTS:		
NEXT ASSY	USED ON	FINISH —			
Microreactor		DO NOT SCALE DRAWING			

Univ. of Pitt.

The Right Elbow

SIZE	DWG. NO.	REV.
A		
SCALE:1:1	WEIGHT:	SHEET 4 OF 4

D.3 DRAWINGS OF THE INERT GAS PROTECTION SYSTEM

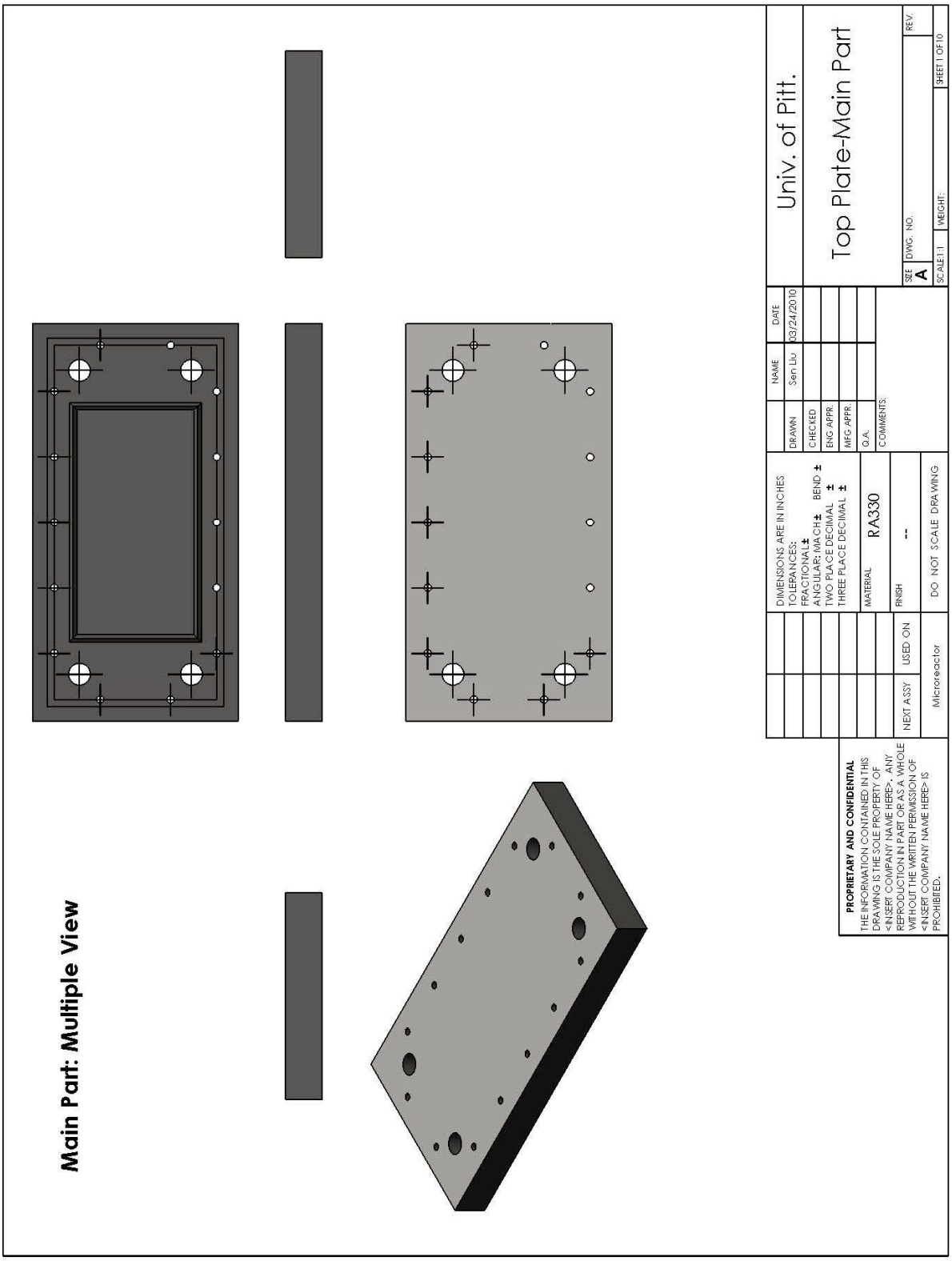

Main Part - Top View

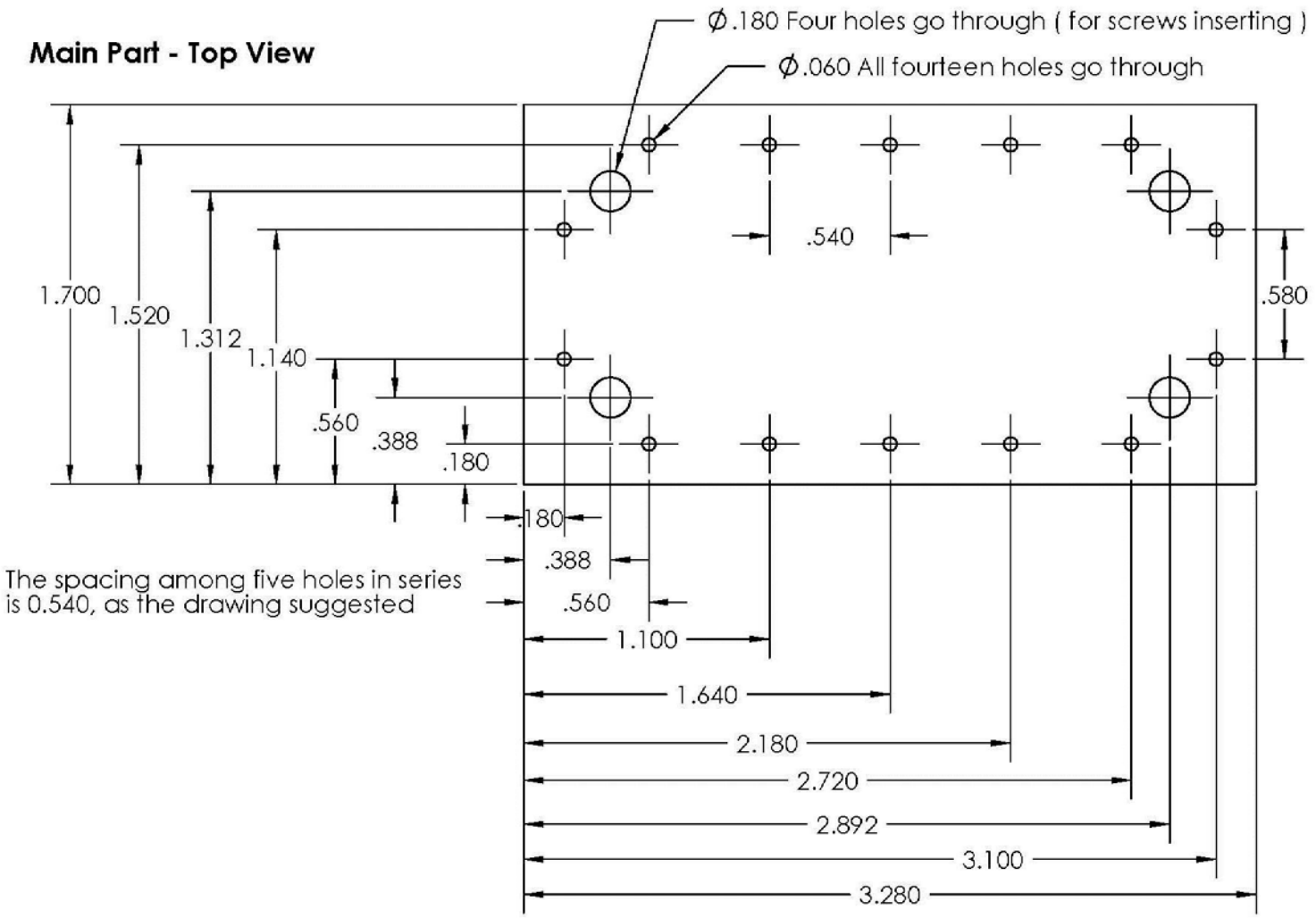

The spacing among five holes in series is 0.540, as the drawing suggested

		DIMENSIONS ARE IN INCHES TOLERANCES: FRACTIONAL ± ANGULAR: MACH ± BEND ± TWO PLACE DECIMAL ± THREE PLACE DECIMAL ±		NAME	DATE
			DRAWN	Sen Liu	03/24/2010
			CHECKED		
			ENG APPR.		
			MFG APPR.		
		MATERIAL RA330	Q.A.		
NEXT ASSY	USED ON	FINISH --	COMMENTS:		
	Microreactor	DO NOT SCALE DRAWING			

Univ. of Pitt.

Top Plate-Main Part

SIZE	DWG. NO.	REV.
A		
SCALE:1:1	WEIGHT:	SHEET 2 OF 10

Main Part - Bottom View

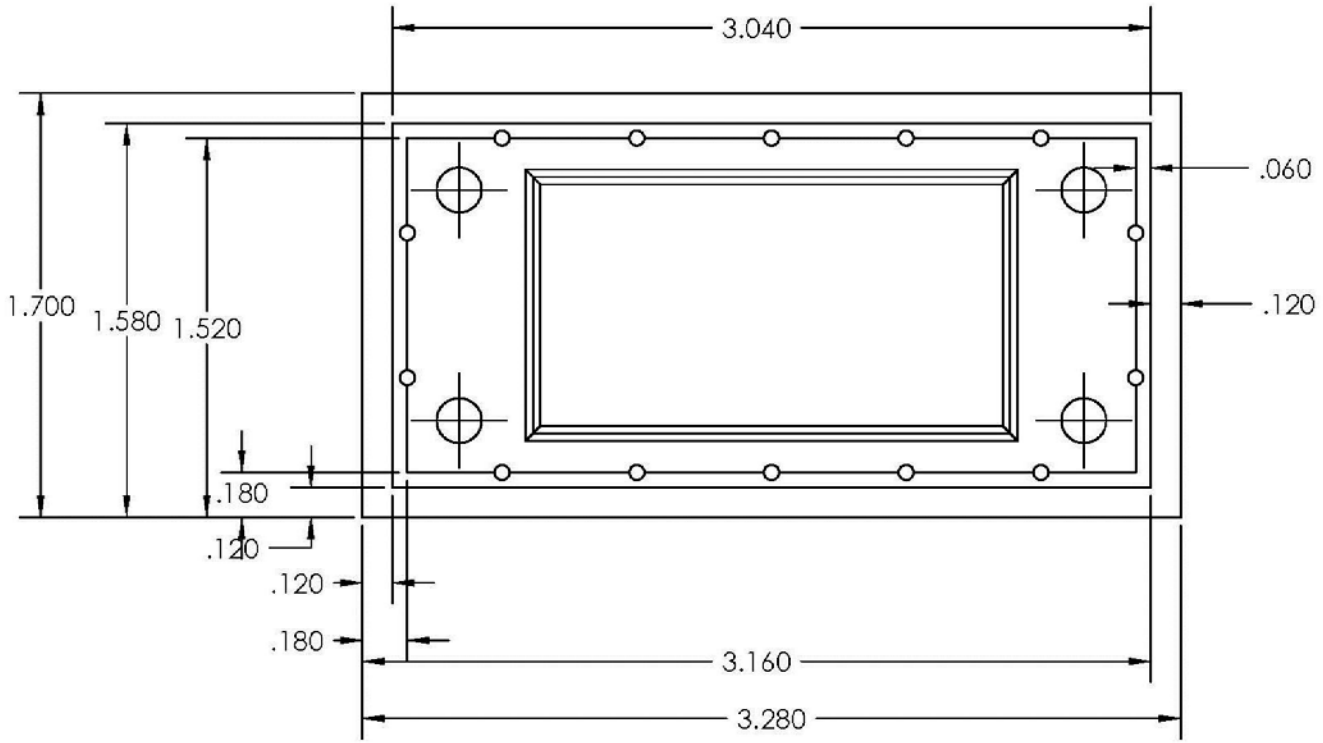

		DIMENSIONS ARE IN INCHES TOLERANCES: FRACTIONAL ± ANGULAR: MACH ± BEND ± TWO PLACE DECIMAL ± THREE PLACE DECIMAL ±		NAME	DATE
			DRAWN	Sen Liu	03/24/2010
			CHECKED		
			ENG APPR.		
			MFG APPR.		
			Q.A.		
		MATERIAL RA330	COMMENTS:		
NEXT ASSY	USED ON	FINISH —			
Microreactor		DO NOT SCALE DRAWING			

PROPRIETARY AND CONFIDENTIAL

THE INFORMATION CONTAINED IN THIS DRAWING IS THE SOLE PROPERTY OF <INSERT COMPANY NAME HERE>. ANY REPRODUCTION IN PART OR AS A WHOLE WITHOUT THE WRITTEN PERMISSION OF <INSERT COMPANY NAME HERE> IS PROHIBITED.

Univ. of Pitt.

Top Plate-Main Part

SIZE	DWG. NO.	REV.
A		
SCALE:1:1	WEIGHT:	SHEET 3 OF 10

Main Part - Crop View

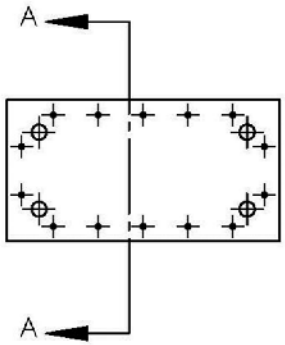

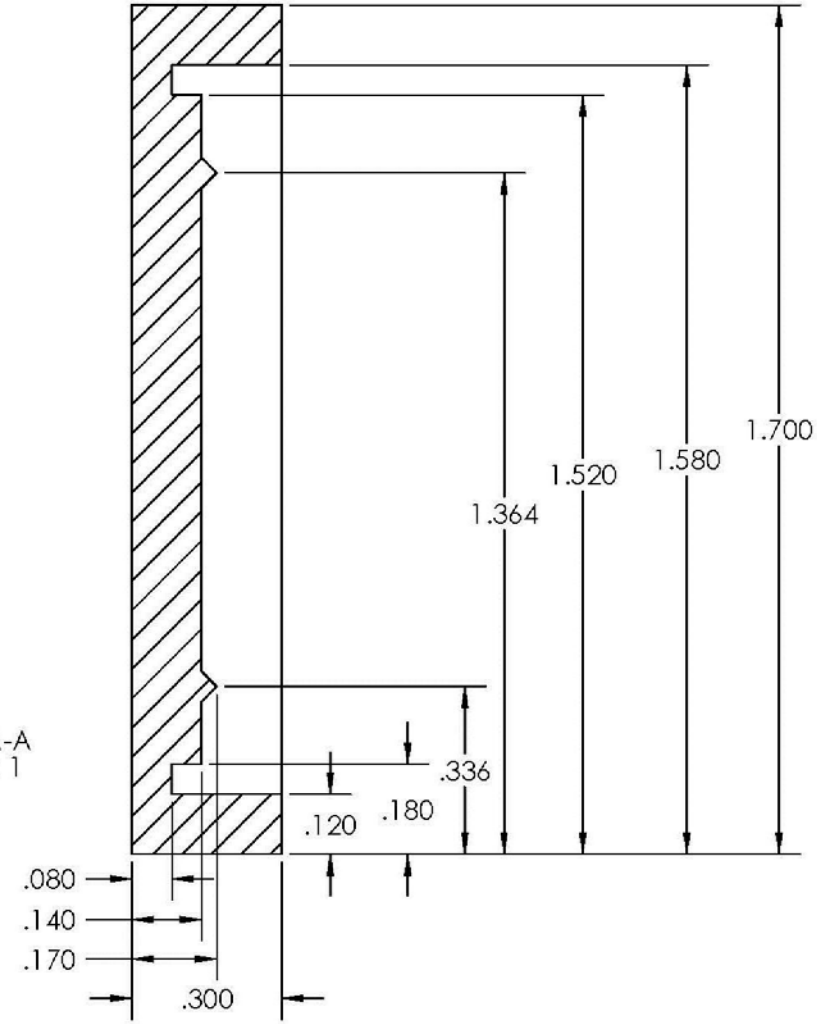

SECTION A-A
SCALE 3 : 1

		DIMENSIONS ARE IN INCHES TOLERANCES: FRACTIONAL ± ANGULAR: MACH ± BEND ± TWO PLACE DECIMAL ± THREE PLACE DECIMAL ±		NAME	DATE
			DRAWN	Sen Liu	03/24/2010
			CHECKED		
			ENG APPR.		
			MFG APPR.		
		MATERIAL RA330	Q.A.		
			COMMENTS:		
NEXT ASSY	USED ON	FINISH --			
Microreactor		DO NOT SCALE DRAWING			

Univ. of Pitt.

Top Plate-Main Part

SIZE	DWG. NO.	REV.
A		
SCALE:1:1	WEIGHT:	SHEET 4 OF 10

Accessory Part - Multiple View

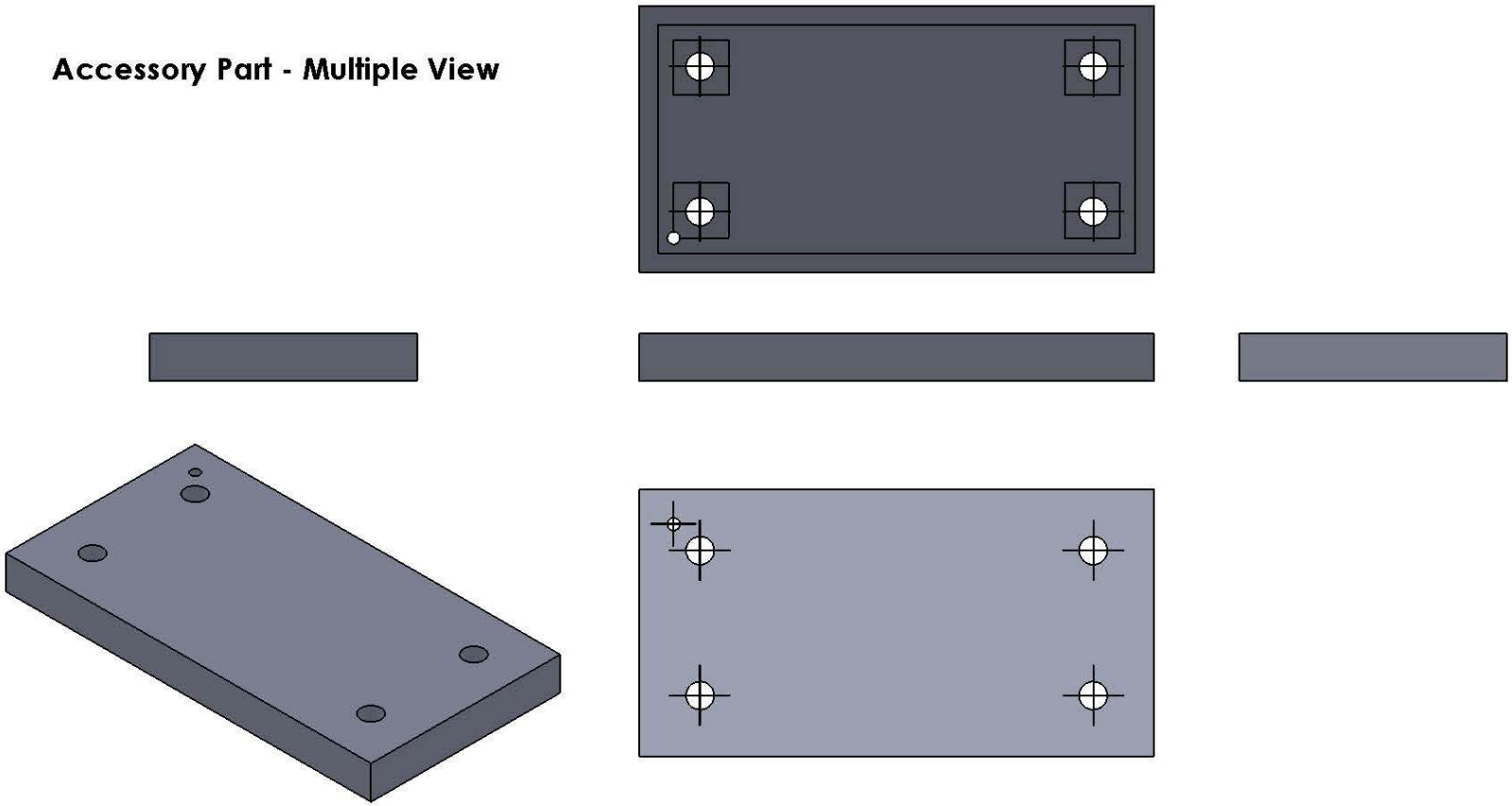

		DIMENSIONS ARE IN INCHES TOLERANCES: FRACTIONAL ± ANGULAR: MACH ± BEND ± TWO PLACE DECIMAL ± THREE PLACE DECIMAL ±		NAME	DATE
			DRAWN	Sen Liu	03/24/2010
			CHECKED		
			ENG APPR.		
			MFG APPR.		
		MATERIAL RA330	Q.A.		
			COMMENTS:		
NEXT ASSY	USED ON	FINISH --			
Microreactor		DO NOT SCALE DRAWING			

Univ. of Pitt.

Top Plate-Accessory

SIZE	DWG. NO.	REV.
A		
SCALE:1:1	WEIGHT:	SHEET 5 OF 10

Accessory Part - Top View

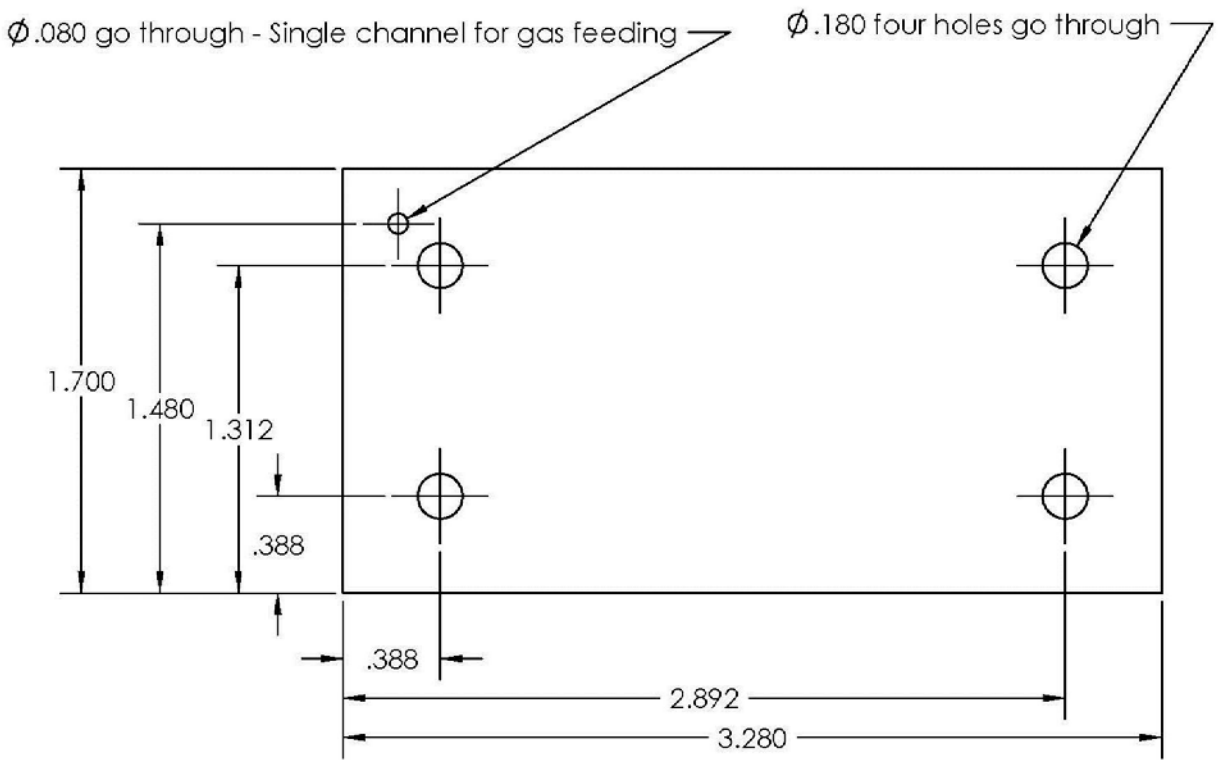

		DIMENSIONS ARE IN INCHES TOLERANCES: FRACTIONAL ± ANGULAR: MACH ± BEND ± TWO PLACE DECIMAL ± THREE PLACE DECIMAL ±		NAME	DATE
			DRAWN	Sen Liu	03/24/2010
			CHECKED		
			ENG APPR.		
			MFG APPR.		
		MATERIAL RA330	Q.A.		
		FINISH —	COMMENTS:		
NEXT ASSY	USED ON				
	Microreactor	DO NOT SCALE DRAWING			

Univ. of Pitt.

Top Plate-Accessory

SIZE	DWG. NO.	REV.
A		
SCALE:1:1	WEIGHT:	SHEET 6 OF 10

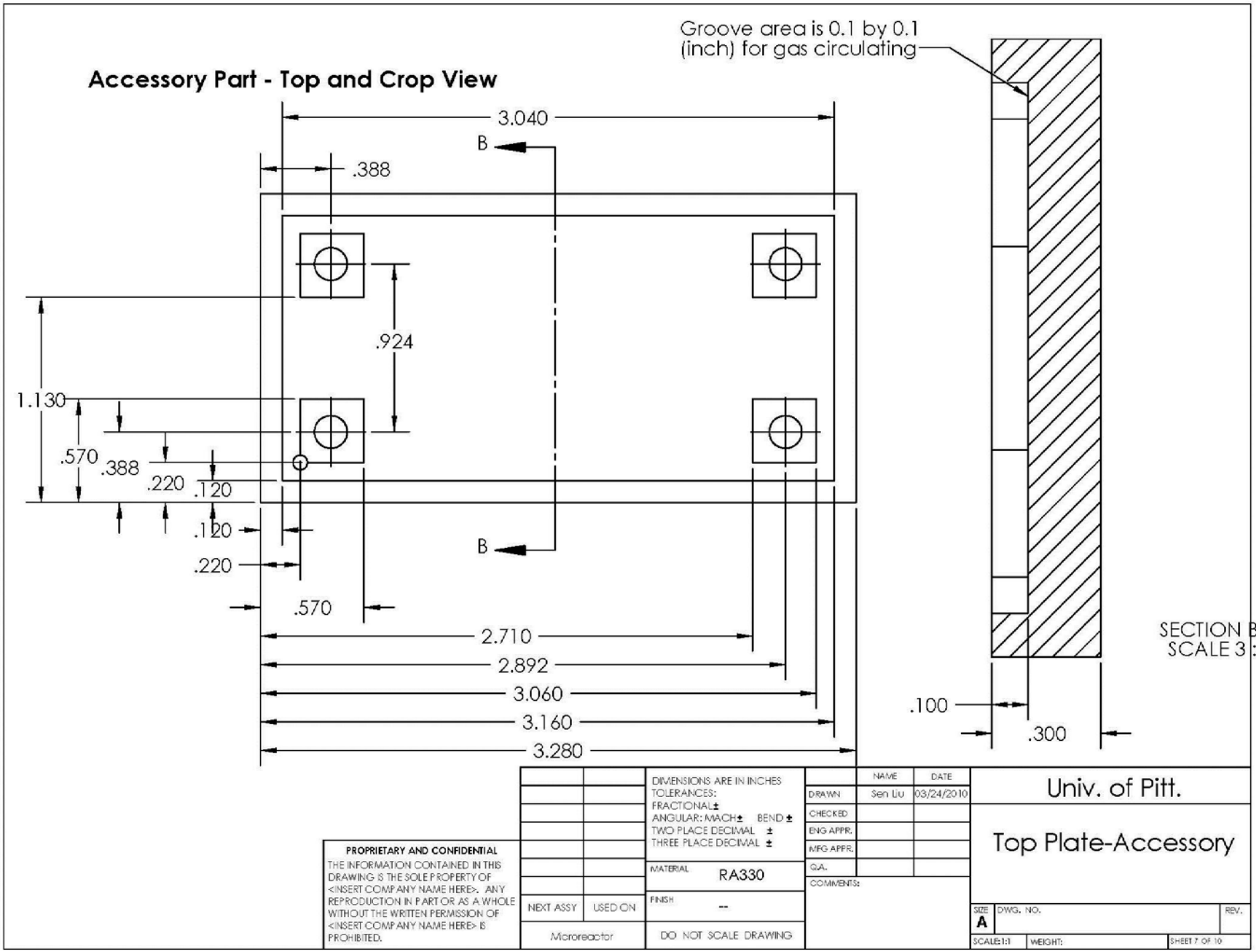
Accessory Part - Top and Crop View
Groove area is 0.1 by 0.1 (inch) for gas circulating
3.040
.388
B
.924
1.130
.570
.388
.220
.120
.120
.220
.570
2.710
2.892
3.060
3.160
3.280
SECTION B
SCALE 3 :
.100
.300
PROPRIETARY AND CONFIDENTIAL
THE INFORMATION CONTAINED IN THIS DRAWING IS THE SOLE PROPERTY OF <INSERT COMPANY NAME HERE>. ANY REPRODUCTION IN PART OR AS A WHOLE WITHOUT THE WRITTEN PERMISSION OF <INSERT COMPANY NAME HERE> IS PROHIBITED.
NEXT ASSY
USED ON
Microreactor
DIMENSIONS ARE IN INCHES
TOLERANCES:
FRACTIONAL ±
ANGULAR: MACH ± BEND ±
TWO PLACE DECIMAL ±
THREE PLACE DECIMAL ±
MATERIAL RA330
FINISH --
DO NOT SCALE DRAWING
NAME
DATE
DRAWN Sen Liu 03/24/2010
CHECKED
ENG APPR.
MFG APPR.
Q.A.
COMMENTS:
Univ. of Pitt.
Top Plate-Accessory
SIZE A
DWG. NO.
REV.
SCALE:1:1
WEIGHT:
SHEET 7 OF 10

Top Plate Assembly - Multiple View

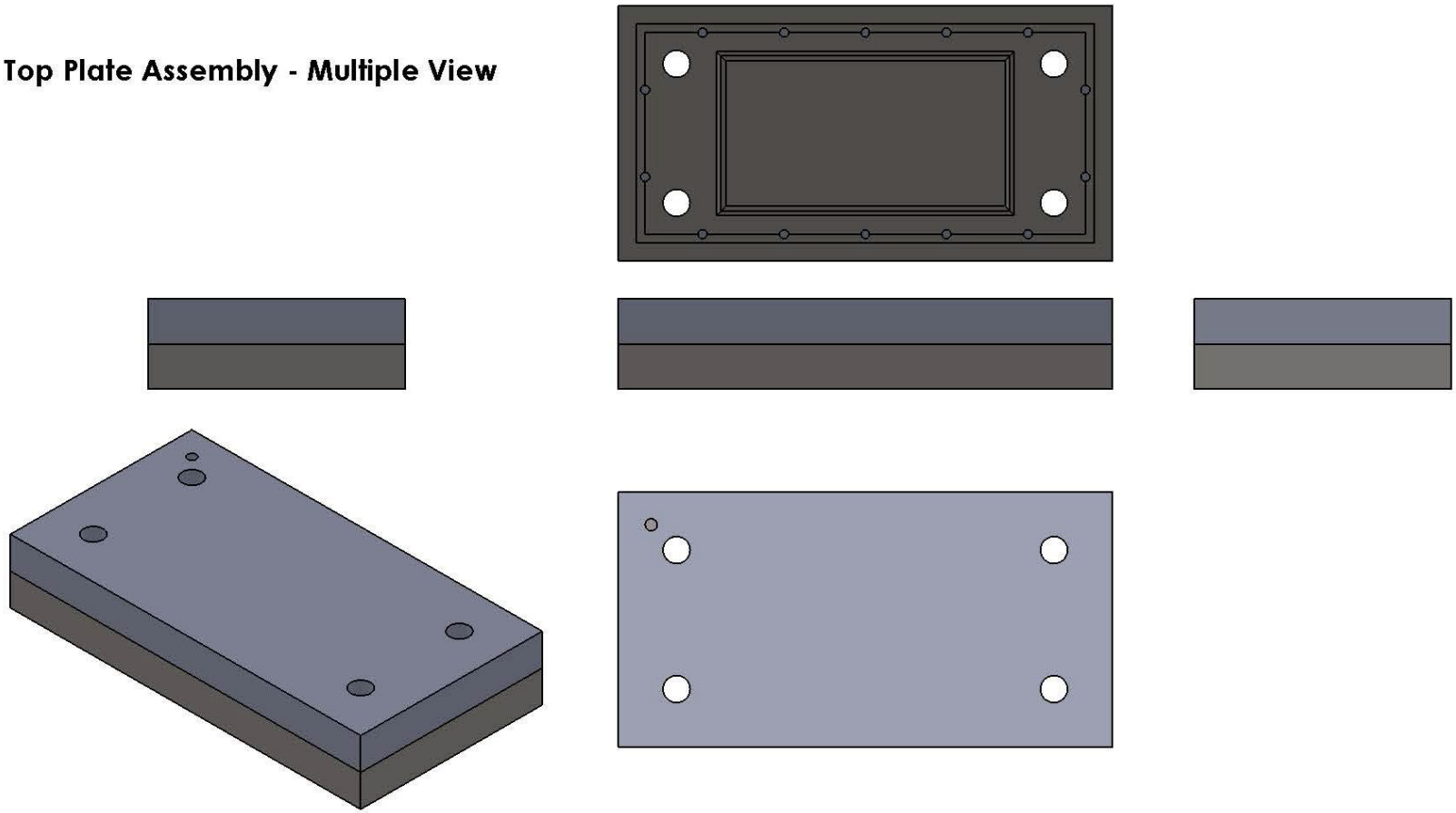

		DIMENSIONS ARE IN INCHES TOLERANCES: FRACTIONAL ± ANGULAR: MACH ± BEND ± TWO PLACE DECIMAL ± THREE PLACE DECIMAL ±		NAME	DATE
			DRAWN	Sen Liu	03/24/2010
			CHECKED		
			ENG APPR.		
			MFG APPR.		
		MATERIAL RA330	Q.A.		
			COMMENTS:		
NEXT ASSY	USED ON	FINISH --			
Microreactor		DO NOT SCALE DRAWING			

Univ. of Pitt.

Top Plate

SIZE	DWG. NO.	REV.
A		
SCALE:1:1	WEIGHT:	SHEET 8 OF 10

Top Plate Assembly - Crop View

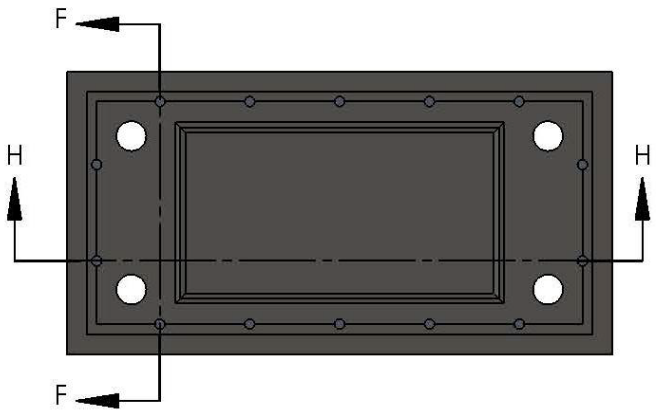

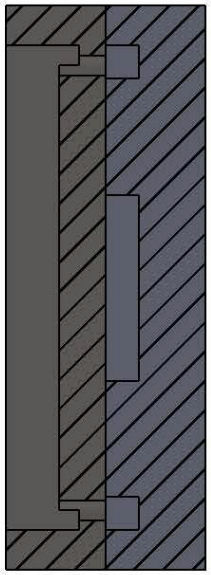

SECTION F-F
SCALE 2 : 1

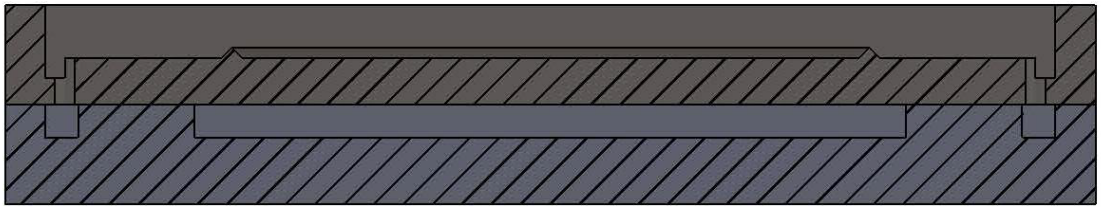

SECTION H-H
SCALE 2 : 1

		DIMENSIONS ARE IN INCHES TOLERANCES: FRACTIONAL ± ANGULAR: MACH ± BEND ± TWO PLACE DECIMAL ± THREE PLACE DECIMAL ±		NAME	DATE
			DRAWN	Sen Liu	03/24/2010
			CHECKED		
			ENG APPR.		
			MFG APPR.		
			Q.A.		
			COMMENTS:		
NEXT ASSY	USED ON	MATERIAL RA330			
		FINISH --			
Microreactor		DO NOT SCALE DRAWING			

Univ. of Pitt.

Top Plate

SIZE	DWG. NO.	REV.
A		
SCALE:1:1	WEIGHT:	SHEET 9 OF 10

BIBLIOGRAPHY

[1] S. Chattopadhyay, G. Veser, Heterogeneous-homogeneous interactions in catalytic microchannel reactors, Aiche J, 52 (2006) 2217-2229.

[2] D.G. Vlachos, The Interplay of Transport, Kinetics, and Thermal Interactions in the Stability of Premixed Hydrogen-Air Flames near Surfaces, Combust Flame, 103 (1995) 59-75.

[3] A. Balakrishna, L.D. Schmidt, R. Aris, Pt-Catalyzed Combustion of Ch4-C3h8 Mixtures, Chem Eng Sci, 49 (1994) 11-18.

[4] R.P. O'Connor, L.D. Schmidt, Catalytic partial oxidation of cyclohexane in a single-gauze reactor, J Catal, 191 (2000) 245-256.

[5] A. Donazzi, M. Maestri, B.C. Michael, A. Beretta, P. Forzatti, G. Groppi, E. Tronconi, L.D. Schmidt, D.G. Vlachos, Microkinetic modeling of spatially resolved autothermal CH4 catalytic partial oxidation experiments over Rh-coated foams, J Catal, 275 (2010) 270-279.

[6] Y.K. Park, P.A. Bui, D.G. Vlachos, Operation regimes in catalytic combustion: H-2/Air mixtures near Pt, Aiche J, 44 (1998) 2035-2043.

[7] D.G. Norton, D.G. Vlachos, A CFD study of propane/air microflame stability, Combust Flame, 138 (2004) 97-107.

[8] M. Wartmann, High-Temperature Methane Oxidation in Catalytic Micro-Channels, in, 2005.

[9] K.F. Jensen, T. Inoue, M.A. Schmidt, Microfabricated multiphase reactors for the direct synthesis of hydrogen peroxide from hydrogen and oxygen, Ind Eng Chem Res, 46 (2007) 1153-1160.

[10] K.F. Jensen, R.L. Hartman, Microchemical systems for continuous-flow synthesis, Lab Chip, 9 (2009) 2495-2507.

[11] J.M. Park, D.S. Kim, T.G. Kang, T.H. Kwon, Improved serpentine laminating micromixer with enhanced local advection, Microfluid Nanofluid, 4 (2008) 513-523.

[12] J. Choe, I.H. Song, J.H. Kim, S.G. Lee, S.M. Lee, K.H. Song, Gas/liquid dispersion in a sequential split micromixer, J Ind Eng Chem, 14 (2008) 161-165.

[13] A. Zampieri, P. Colombo, G.T.P. Mabande, T. Selvam, W. Schwieger, F. Scheffler, Zeolite coatings on microcellular ceramic foams: A novel route to microreactor and microseparator devices, Adv Mater, 16 (2004) 819-+.

[14] C.P. Lee, M.F. Lai, Microseparator for magnetic particle separations, J Appl Phys, 107 (2010).

[15] K.F. Jensen, H.R. Sahoo, J.G. Kralj, Multistep continuous-flow microchemical synthesis involving multiple reactions and separations, Angew Chem Int Edit, 46 (2007) 5704-5708.

[16] G. Veser, Experimental and theoretical investigation of H-2 oxidation in a high-temperature catalytic microreactor, Chem Eng Sci, 56 (2001) 1265-1273.

[17] Y.S. Seo, S.J. Cho, S.K. Kang, H.D. Shin, Experimental and numerical studies on combustion characteristics of a catalytically stabilized combustor, Catal Today, 59 (2000) 75-86.

[18] J. Mantzaras, C. Appel, Effects of finite rate heterogeneous kinetics on homogeneous ignition in catalytically stabilized channel flow combustion, Combust Flame, 130 (2002) 336-351.

[19] H. Zhu, R.J. Kee, J.R. Engel, D.T. Wickham, Catalytic partial oxidation of methane using RhSr- and Ni-substituted hexaaluminates, P Combust Inst, 31 (2007) 1965-1972.

[20] A. Bitsch-Larsen, R. Horn, L.D. Schmidt, Catalytic partial oxidation of methane on rhodium and platinum: Spatial profiles at elevated pressure, Appl Catal a-Gen, 348 (2008) 165-172.

[21] A. Beretta, A. Donazzi, D. Livio, M. Maestri, G. Groppi, E. Tronconi, P. Forzatti, Synergy of Homogeneous and Heterogeneous Chemistry Probed by In Situ Spatially Resolved Measurements of Temperature and Composition, Angew Chem Int Edit, 50 (2011) 3943-3946.

[22] D.A. Henning, L.D. Schmidt, Oxidative dehydrogenation of ethane at short contact times: species and temperature profiles within and after the catalyst, Chem Eng Sci, 57 (2002) 2615-2625.

[23] R.S. Vincent, R.P. Lindstedt, N.A. Malik, I.A.B. Reid, B.E. Messenger, The chemistry of ethane dehydrogenation over a supported platinum catalyst, J Catal, 260 (2008) 37-64.

[24] S.F. Hakonsen, J.C. Walmsley, A. Holmen, Ethene production by oxidative dehydrogenation of ethane at short contact times over Pt-Sn coated monoliths, Appl Catal a-Gen, 378 (2010) 1-10.

[25] L. Mleczko, M. Baerns, Catalytic Oxidative Coupling of Methane - Reaction-Engineering Aspects and Process Schemes, Fuel Process Technol, 42 (1995) 217-248.

[26] J.H. Lunsford, The Catalytic Oxidative Coupling of Methane, Angewandte Chemie-International Edition in English, 34 (1995) 970-980.

[27] J.W. Thybaut, J.J. Sun, L. Olivier, A.C. Van Veen, C. Mirodatos, G.B. Marin, Catalyst design based on microkinetic models: Oxidative coupling of methane, Catal Today, 159 (2011) 29-36.

[28] J.L. Colby, P.J. Dauenhauer, L.D. Schmidt, Millisecond autothermal steam reforming of cellulose for synthetic biofuels by reactive flash volatilization, Green Chem, 10 (2008) 773-783.

[29] J.C. Serrano-Ruiz, J.A. Dumesic, Catalytic routes for the conversion of biomass into liquid hydrocarbon transportation fuels, Energ Environ Sci, 4 (2011) 83-99.

[30] R. Quiceno, J. Perez-Ramirez, J. Warnatz, O. Deutschmann, Modeling the high-temperature catalytic partial oxidation of methane over platinum gauze: Detailed gas-phase and surface chemistries coupled with 3D flow field simulations, Appl Catal a-Gen, 303 (2006) 166-176.

[31] M.C. Huff, I.P. Androulakis, J.H. Sinfelt, S.C. Reyes, The contribution of gas-phase reactions in the Pt-catalyzed conversion of ethane-oxygen mixtures, J Catal, 191 (2000) 46-54.

[32] Z. Stansch, L. Mleczko, M. Baerns, Comprehensive kinetics of oxidative coupling of methane over the La2O3/CaO catalyst, Ind Eng Chem Res, 36 (1997) 2568-2579.

[33] F. Birkhold, U. Meingast, P. Wassermann, O. Deutschmann, Modeling and simulation of the injection of urea-water-solution for automotive SCR DeNO(x)-systems, Appl Catal B-Environ, 70 (2007) 119-127.

[34] O. Deutschmann, J. Koop, Detailed surface reaction mechanism for Pt-catalyzed abatement of automotive exhaust gases, Appl Catal B-Environ, 91 (2009) 47-58.

[35] O. Deutschmann, N. Mladenov, J. Koop, S. Tischer, Modeling of transport and chemistry in channel flows of automotive catalytic converters, Chem Eng Sci, 65 (2010) 812-826.

[36] C.T. Goralski, R.P. O'Connor, L.D. Schmidt, Modeling homogeneous and heterogeneous chemistry in the production of syngas from methane, Chem Eng Sci, 55 (2000) 1357-1370.

[37] O. Deutschmann, V.M. Janardhanan, Numerical study of mass and heat transport in solid-oxide fuel cells running on humidified methane, Chem Eng Sci, 62 (2007) 5473-5486.

[38] O. Deutschmann, T. Kaltschmitt, L. Maier, M. Hartmann, C. Hauck, Influence of gas-phase reactions on catalytic reforming of isooctane, P Combust Inst, 33 (2011) 3177-3183.

[39] O. Deutschmann, M. Hartmann, L. Maier, Hydrogen production by catalytic partial oxidation of iso-octane at varying flow rate and fuel/oxygen ratio: From detailed kinetics to reactor behavior, Appl Catal a-Gen, 391 (2011) 144-152.

[40] H.D. Minh, H.G. Bock, S. Tischer, O. Deutschmann, Optimization of two-dimensional flows with homogeneous and heterogeneously catalyzed gas-phase reactions, Aiche J, 54 (2008) 2432-2440.

[41] COMSOL Multiphysics User's Guide, in, COMSOL Multiphysics, 2010.

[42] COMSOL Multiphysics - Reference Guide in, COMSOL Multiphysics, 2010.

[43] N. Snow, ExxonMobil sees growing role of natural gas by 2030, Oil Gas J, 109 (2011) 34-35.

[44] O.V. Krylov, A.A. Firsova, A.A. Bobyshev, V.A. Radtsig, D.P. Shashkin, L.Y. Margolis, Mechanochemical Activation of Methane Oxidation Catalysts, Catal Today, 13 (1992) 381-390.

[45] G.E. Keller, M.M. Bhasin, Synthesis of Ethylene Via Oxidative Coupling of Methane .1. Determination of Active Catalysts, J Catal, 73 (1982) 9-19.

[46] M. Baerns, H. Hofmann, Characterization of Activity, Selectivity and Deactivation of Solid Catalysts, Proceedings of the 8th Icc Post Congress Symposium, Bochum, July 10-11, 1984 - Preface, Appl Catal, 15 (1985) R11-R12.

[47] T. Ito, J.X. Wang, C.H. Lin, J.H. Lunsford, Oxidative Dimerization of Methane over a Lithium-Promoted Magnesium-Oxide Catalyst, J Am Chem Soc, 107 (1985) 5062-5068.

[48] A.S. Bodke, D.A. Olschki, L.D. Schmidt, E. Ranzi, High selectivities to ethylene by partial oxidation of ethane, Science, 285 (1999) 712-715.

[49] C. Qi, J.H.B.J. Hoebink, G.B. Marin, Kinetics of the Oxidative Coupling of Methane at Atmospheric-Pressure in the Absence of Catalyst, Ind Eng Chem Res, 30 (1991) 2088-2097.

[50] J. Sun, J.W. Thybaut, G.B. Marin, Microkinetics of methane oxidative coupling, Catal Today, 137 (2008) 90-102.

[51] Q. Chen, P.M. Couwenberg, G.B. Marin, Effect of Pressure on the Oxidative Coupling of Methane in the Absence of Catalyst, Aiche J, 40 (1994) 521-535.

[52] M. Fleys, Y. Simon, P.M. Marquaire, Detailed kinetic study of the partial oxidation of methane over La2O3 catalyst. Part 2: Mechanism, Ind Eng Chem Res, 46 (2007) 1069-1078.

[53] W.H. Green, Y.S. Su, J.Y. Ying, Upper bound on the yield for oxidative coupling of methane, J Catal, 218 (2003) 321-333.

[54] M. Fleys, W.J. Shan, Y. Simon, P.M. Marquaire, Detailed kinetic study of the partial oxidation of methane over La2O3 catalyst. Part 1: Experimental results, Ind Eng Chem Res, 46 (2007) 1063-1068.

[55] C.H. Lin, K.D. Campbell, J.X. Wang, J.H. Lunsford, Oxidative Dimerization of Methane over Lanthanum Oxide, J Phys Chem-Us, 90 (1986) 534-537.

[56] H. Yamashita, Y. Machida, A. Tomita, Oxidative Coupling of Methane with Peroxide Ions over Barium Lanthanum Oxygen Mixed-Oxide, Appl Catal, 79 (1991) 203-214.

[57] H. Borchert, M. Baerns, The effect of oxygen-anion conductivity of metal-oxide doped lanthanum oxide catalysts on hydrocarbon selectivity in the oxidative coupling of methane, J Catal, 168 (1997) 315-320.

[58] M. Neurock, M.S. Palmer, M.M. Olken, Periodic density functional theory study of methane activation over La2O3: Activity of O2-, O-, O-2(2-), oxygen point defect, and Sr2+-doped surface sites, J Am Chem Soc, 124 (2002) 8452-8461.

[59] N.D. Chuvylkin, G.M. Zhidomirov, V.B. Kazansky, S-3(-) Radicals Stabilized on Mgo Surface, J Magn Reson, 26 (1977) 433-435.

[60] D.D. Nogare, N.J. Degenstein, R. Horn, P. Canu, L.D. Schmidt, Modeling spatially resolved data of methane catalytic partial oxidation on Rh foam catalyst at different inlet compositions and flowrates, J Catal, 277 (2011) 134-148.

[61] B.C. Michael, D.N. Nare, L.D. Schmidt, Catalytic partial oxidation of ethane to ethylene and syngas over Rh and Pt coated monoliths: Spatial profiles of temperature and composition, Chem Eng Sci, 65 (2010) 3893-3902.

[62] J.M. Deboy, R.F. Hicks, The Oxidative Coupling of Methane over Alkali, Alkaline-Earth, and Rare-Earth Oxides, Ind Eng Chem Res, 27 (1988) 1577-1582.

[63] M.R. Quddus, Y. Zhang, A.K. Ray, Multiobjective Optimization of a Porous Ceramic Membrane Reactor for Oxidative Coupling of Methane, Ind Eng Chem Res, 49 (2010) 6469-6481.

[64] N.S. Kaisare, G.D. Stefanidis, D.G. Vlachos, Millisecond Production of Hydrogen from Alternative, High Hydrogen Density Fuels in a Cocurrent Multifunctional Microreactor, Ind Eng Chem Res, 48 (2009) 1749-1760.

[65] M.S. Mettler, G.D. Stefanidis, D.G. Vlachos, Enhancing stability in parallel plate microreactor stacks for syngas production, Chem Eng Sci, 66 (2011) 1051-1059.

[66] O. Deutschmann, W. Boll, S. Tischer, Loading and Aging Effects in Exhaust Gas After-Treatment Catalysts with Pt As Active Component, Ind Eng Chem Res, 49 (2010) 10303-10310.

[67] D.M.G. Gregory P. Smith, Michael Frenklach, Nigel W. Moriarty, Boris Eiteneer, Mikhail Goldenberg, C. Thomas Bowman, Ronald K. Hanson, Soonho Song, William C. Gardiner, Jr., Vitali V. Lissianski, and Zhiwei Qin GRI-MECH, in.

[68] M. O Conaire, H.J. Curran, J.M. Simmie, W.J. Pitz, C.K. Westbrook, A comprehensive modeling study of hydrogen oxidation, Int J Chem Kinet, 36 (2004) 603-622.

[69] D.L. Baulch, C.J. Cobos, R.A. Cox, C. Esser, P. Frank, T. Just, J.A. Kerr, M.J. Pilling, J. Troe, R.W. Walker, J. Warnatz, Evaluated Kinetic Data for Combustion Modeling, J Phys Chem Ref Data, 21 (1992) 411-734.

[70] F. Behrendt, O. Deutschmann, R. Schmidt, J. Warnatz, Ignition and extinction of hydrogen-air and methane-air mixtures over platinum and palladium, Heterogeneous Hydrocarbon Oxidation, 638 (1996) 48-57.

[71] D. Chatterjee, O. Deutschmann, J. Warnatz, Detailed surface reaction mechanism in a three-way catalyst, Faraday Discuss, 119 (2001) 371-384.

[72] D.K. Zerkle, M.D. Allendorf, M. Wolf, O. Deutschmann, Understanding homogeneous and heterogeneous contributions to the platinum-catalyzed partial oxidation of ethane in a short-contact-time reactor, J Catal, 196 (2000) 18-39.

[73] O. Deutschmann, M. Hartmann, L. Maier, H.D. Minh, Catalytic partial oxidation of iso-octane over rhodium catalysts: An experimental, modeling, and simulation study, Combust Flame, 157 (2010) 1771-1782.

[74] P.M. Couwenberg, Q. Chen, G.B. Marin, Kinetics of a gas-phase chain reaction catalyzed by a solid: The oxidative coupling of methane over Li/MgO-based catalysts, Ind Eng Chem Res, 35 (1996) 3999-4011.

[75] P.M. Couwenberg, Q. Chen, G.B. Marin, Irreducible mass-transport limitations during a heterogeneously catalyzed gas-phase chain reaction: Oxidative coupling of methane, Ind Eng Chem Res, 35 (1996) 415-421.

[76] Weak Form Modeling, in: COMSOL Multiphysics - User's Guide, COMSOL Multiphysics, 2010, pp. 533.

[77] Chemical Reaction Engineering Module - User's Guide, in, COMSOL Mulphysics, 2010.

[78] The Chemical Species Transport Interfaces, in: Chemical REACTION Engineering Module - User's Guide, COMSOL Multiphysics, 2010.

[79] O. Schenk, A. Wachter, M. Hagemann, Matching-based preprocessing algorithms to the solution of saddle-point problems in large-scale nonconvex interior-point optimization, Comput Optim Appl, 36 (2007) 321-341.

[80] O. Schenk, M. Bollhofer, R.A. Romer, On large-scale diagonalization techniques for the Anderson model of localization, Siam J Sci Comput, 28 (2006) 963-983.

[81] R.H. Nibbelke, J. Scheerova, M.H.J.M. Decroon, G.B. Marin, The Oxidative Coupling of Methane over Mgo-Based Catalysts - a Steady-State Isotope Transient Kinetic-Analysis, J Catal, 156 (1995) 106-119.

[82] M.E. Dry, Practical and theoretical aspects of the catalytic Fischer-Tropsch process, Appl Catal a-Gen, 138 (1996) 319-344.

[83] T. Ren, Olefins from conventional and heavy feedstocks: Energy use in steam cracking and alternative processes, Energy, 2006 (2006) 425-451.

[84] M. Huff, L.D. Schmidt, Ethylene Formation by Oxidative Dehydrogenation of Ethane over Monoliths at Very Short-Contact Times, J Phys Chem-Us, 97 (1993) 11815-11822.

[85] R. Horn, N.J. Degenstein, K.A. Williams, L.D. Schmidt, Spatial and temporal profiles in millisecond partial oxidation processes, Catal Lett, 110 (2006) 169-178.

[86] N.E. Fernandes, Y.K. Park, D.G. Vlachos, The autothermal behavior of platinum catalyzed hydrogen oxidation: Experiments and modeling, Combust Flame, 118 (1999) 164-178.

[87] D.G. Norton, D.G. Vlachos, Hydrogen assisted self-ignition of propane/air mixtures in catalytic microburners, P Combust Inst, 30 (2005) 2473-2480.

[88] A.S. Bodke, D. Henning, L.D. Schmidt, S.S. Bharadwaj, J.J. Maj, J. Siddall, Oxidative dehydrogenation of ethane at millisecond contact times: Effect of H-2 addition, J Catal, 191 (2000) 62-74.

[89] B. Yang, T. Yuschak, T. Mazanec, A.L. Tonkovich, S. Perry, Multi-scale modeling of microstructured reactors for the oxidative dehydrogenation of ethane to ethylene, Chem Eng J, 135 (2008) S147-S152.

[90] F. Donsi, T. Caputo, G. Russo, A. Di Benedetto, R. Pirone, Modeling ethane oxy-dehydrogenation over monolithic combustion catalysts, Aiche J, 50 (2004) 2233-2245.

[91] O. Deutschmann, B.T. Schadel, M. Duisberg, Steam reforming of methane, ethane, propane, butane, and natural gas over a rhodium-based catalyst, Catal Today, 142 (2009) 42-51.

[92] M. Hartmann, T. Kaltschmitt, O. Deutschmann, Catalytic partial oxidation of higher hydrocarbon fuel components on Rh/Al(2)O(3) coated honeycomb monoliths, Catal Today, 147 (2009) S204-S209.

[93] R. Horn, O. Korup, M. Geske, U. Zavyalova, I. Oprea, R. Schlogl, Reactor for in situ measurements of spatially resolved kinetic data in heterogeneous catalysis, Rev Sci Instrum, 81 (2010) -.